Deposition of ITO and AZO thin films by laser ablation at 355 nm in a background atmosphere

Thestrup Nielsen, Birgitte

Publication date:
2000

Document Version
Publisher's PDF, also known as Version of record

Risø-R-1140(EN)

Deposition of ITO and AZO thin films by laser ablation at 355 nm in a background atmosphere

Birgitte Thestrup

Risø National Laboratory, Roskilde
February 2000

Abstract The main topic in this thesis is deposition of ITO and AZO thin films by pulsed laser ablation at 355 nm in a background atmosphere.

Indium tin oxide (ITO) and aluminium doped zinc oxide (AZO) films belong to the transparent, semiconducting films, which have many applications in opto-electronic devices.

Pulsed laser deposition (PLD) is a relatively new film deposition technique, which is applicable, especially, for deposition of multi-component oxide materials. However, despite of its success, the deposition process is not understood in detail.

Here, a design of a pulsed laser deposition setup with the opportunity of varying key deposition parameters is presented. A comprehensive experimental study, on how the material properties of laser deposited ITO films at 355 nm are influenced by specific experimental parameters in the PLD process, is given. Especially, this study clarifies the connection between the electrical and optical properties of the ITO films and the background atmosphere. Furthermore, a comparison between the material properties of AZO and ITO films grown at similar deposition conditions is presented. Finally, holographic recording in laser deposited AZO and ITO thin films is demonstrated.

Cover picture: Side view of laser plasma seen through vacuum window during film deposition. The plasma is the elongated bright area in the blue light seen in the lower right corner of the photo. The author to this thesis is standing to the left of the chamber.

This thesis is submitted in partial fulfilment of the requirements for the degree of Doctor of Philosophy at the University of Copenhagen, Denmark.

ISBN 87-550-2609-5
ISSN 0106-2840

Information Service Department, Risø, 2000

Contents

Preface and acknowledgements

The present thesis has been carried out at the Optics and Fluid Dynamics Department (OFD), Risø National Laboratory, Denmark from August 1994 to December 1999. Within this period I was on maternal leave twice for 10 plus 12 months. The first 13 months of my Ph.d. study I worked full time, while the rest of the period I worked ¾ of full time. Due to these circumstances, my Ph.d. study was equivalently extended.

The work leading to this thesis was supervised by Dr. Jørgen Schou, Senior Scientist in OFD, Risø National Laboratory, and Professor Nils O. Andersen, Director of the Niels Bohr Institute for Astronomy, Physics and Geophysics, University of Copenhagen.

The project was financed by the Danish Natural Science Research Council.

I want to thank Jørgen Schou for his continuous encouragement during this work and for many fruitful discussions. Furthermore, thanks to Nils O. Andersen for useful conversations. Thanks to my fellow colleagues, who are or were part of our group: Winnie Svendsen, Ole Ellegaard, Tue N. Hansen, Bo Toftmann and Evy Holmelund.

I am very grateful to Arne Nordskov, who built the experimental setup and subsequently improved it. Thanks to Jess Thorsen for technical assistance.

In addition, I want to thank Carsten Dam-Hansen for his help with recording gratings, Niels B. Larsen for his atomic force microscope measurements, Lene Hubert for the X-ray photospectroscopy measurements, and Martin M. Nielsen for the X-ray measurements.

Thanks to Lone Astradson, Heidi Carlsen, and the rest of the staff in the department who have always been helpful, Bitten Skaarup for checking my English, Erik Eilertsen for computer assistance, Lars Lindvold and Per Michael Johansen for professional inspiration.

Special thanks to my husband Steen Arnfred Nielsen for his help and continuous support during this work.

Finally, I would like to express my gratitude to my family and friends for their support and their forgiveness of my lack of time during the last period of writing this thesis.

- going toward a new millennium -

Birgitte Thestrup Nielsen

Risø National Laboratory, Denmark
December 1999

Dansk resumé

Film af indiumtinoxid (ITO) og aluminium-dopet zinkoxid (AZO) tilhører gruppen af transparente, halvledende film. Disse film har mange anvendelser indenfor opto-elektronik.

Hovedemnet i denne afhandling er deponering af ITO og AZO tyndfilm ved brug af laserablation. Ablationen foregår i en specific baggrundsatmosfære ved en laserbølgelængde på 355 nm.

Pulset laserdeponering (PLD) er en relativ ny filmdeponeringsteknik, der specielt er anvendelig til deponering af oxidmaterialer bestående af mange materialekomponenter. På trods af teknikkens succes, er deponeringsprocessen ikke forstået i detaljer.

Denne afhandling præsenterer et design af en opstilling til pulset laserdeponering, hvor essentielle deponeringsparametre kan varieres. Desuden beskrives et omfattende eksperimentelt studie, der viser, hvorledes materialeegenskaberne af laserdeponerede ITO film ved 355 nm påvirkes af specifikke eksperimentelle parametre i PLD processen. I dette studie synliggøres specielt sammenhængen mellem baggrundsatmosfæren og ITO filmenes elektriske og optiske egenskaber. Endvidere sammenlignes egenskaberne af AZO og ITO film groet under samme deponeringsbetingelser. Endelig demonstreres det, hvorledes holografiske gitre kan skrives i laserdeponerede AZO og ITO film.

1 Introduction

1.1 Background

Transparent, semiconducting oxide films have a wide range of applications in both research and industry. They are used as coatings in a variety of devices including solar cells, gas sensors and recently, organic light-emitting devices [1,2]. Indium tin oxide (ITO) is one of the most important metallic oxides for device coatings due to its excellent material properties. Films of ITO have high transmission of visible light (typically above 80%), high electrical conductivity (resistivities in the range 10^{-3} – 10^{-4} Ωcm), and hardness and stability that are superior to those of thin metallic films [1].

However, aluminium-doped zinc oxide (AZO) has recently received attention as a promising alternative to ITO [3]. AZO films have optical and electrical properties similar to ITO films, and zinc is, in addition, a cheap, abundant and non-toxic material.

ITO films have been grown on glass by various deposition techniques such as sputtering, evaporation, chemical vapour deposition, and the sol-gel technique [1,4]. AZO films have also been grown by various techniques [3,5,6], even though much less is known about the deposition process of AZO. Typically, these techniques require a heated substrate or post-annealing of the films in order to fabricate high-quality films. Recently, ITO and AZO films have been produced by pulsed laser deposition (PLD) as well [7,8].

The use of more sophisticated materials and substrates in opto-electronic devices such as, e.g., heat-sensitive polymers and organic materials [2,9] has challenged the production techniques. PLD is a relatively new film deposition technique based on laser ablation [10]. PLD has proven to be a successful technique for depositing films of complex oxide materials, primarily because the stoichiometry from the target is retained in the deposited films. Furthermore, PLD offers the opportunity of depositing films at low substrate temperatures, even room temperature. In addition, the film deposition can be performed in a reactive oxygen atmosphere without the need for further processing.

The oxygen background atmosphere serves two purposes during PLD of metal oxide films. It may slow down and scatter the ablated target particles following a laser pulse, and it may control the oxidation state of the film surface during growth. However, the importance and interplay of each of these two mechanisms have not been clarified in detail.

1.2 Scope and limitations of thesis

The main purpose of this thesis is to present a comprehensive experimental study on how the material properties of laser deposited ITO and AZO thin films are affected by specific experimental parameters in the PLD process. The experimental parameters of interest in this work are the pressure and type of the background gas atmosphere, the substrate temperature, and the laser fluence. The study provides new knowledge about the importance of these parameters in laser deposition of ITO and AZO thin films on glass at a wavelength of 355 nm.

Moreover, a new pulsed laser deposition setup was designed for this work with the opportunity of varying key deposition parameters.

The work was carried out under the following experimental restrictions:

- Glass substrates were used for all deposition experiments.
- The substrate temperature was limited to relatively low temperatures, i.e. from room temperature to 300°C.
- The laser fluence was limited to two regimes. "Low" fluence (0.5 – 0.8 J/cm^2) just above the plasma creation threshold, and "high" fluence (around 2.0 J/cm^2).

1.3 Outline of thesis

The thesis is divided into six chapters, each covering a specific subject. The general structure of the thesis is the following. Chapter 2 introduces pulsed laser deposition. Chapter 3 concerns the experimental setup. In chapters 4, 5 and 6 the main experimental results are presented. The results are divided into three topics – "Deposition rates for ITO and related time-of-flight measurements", "Deposition of ITO films in various background atmospheres", and "Deposition of AZO and ITO films at high laser fluence". Chapter 7 deals with holographic recording in AZO and ITO films. Each chapter contains a summary and a list of references.

The content of the individual chapters is as follows.

- Chapter 2 gives an introduction to pulsed laser deposition of multi-component oxides. The deposition process is described in three steps covering the laser-target interaction, the expansion of the plasma plume, and the film deposition. The first step also includes some practical considerations for laser ablation. The last step is treated more generally, including characteristics for PLD growth.

- Chapter 3 presents the experimental setup designed for this work, together with a description of the film characterisation methods. In general, the deposited films were characterised by their thickness, their electrical sheet resistance, and their transparency for visible light. Furthermore, selected films were characterised by their surface structure, their chemical composition, and their crystallinity. Finally, the chapter describes an experimental setup for time-of-flight measurements.

- Chapter 4 is divided into three sections. The first section contains experimental results that demonstrate how the ITO deposition rate is influenced by specific experimental parameters in the ablation process. The experimental parameters examined are the laser fluence, the pressure and type of the background atmosphere and the substrate temperature. The deposition rate is an essential process parameter in thin film growth. Section two contains a discussion of the accuracy of the experimental method. The third section is devoted to related time-of-flight measurements of silver ions ablated in a neon atmosphere. These measurements give some understanding of the particle dynamics during ablation in a background atmosphere.

- Chapter 5 presents the major part of the experimental results obtained in this work concerning the deposition of ITO films in various background atmos-

pheres – see Thestrup *et al.* [11]. In this chapter it is demonstrated how ITO film properties, surface structure, and composition are strongly related to deposition parameters in the PLD process. The electrical and optical properties of the ITO films are examined in detail as a function of the process parameters. The parameters altered in the PLD process were the background atmosphere, the background gas pressure, and the substrate temperature. Oxygen, neon, argon, and xenon were chosen as background atmospheres. Oxygen because it is the standard reactive atmosphere used in PLD. Neon, argon, and xenon because they are inert gases and their masses resemble the mass of atomic oxygen, molecular oxygen, and indium and tin, respectively. The chapter includes a discussion of general material properties of ITO.

- Chapter 6 is devoted to the deposition of AZO and ITO films at high laser fluence – see Thestrup *et al.* [12,13]. The chapter presents results that compare the electrical and optical properties as well as surface structure and crystallinity of AZO and ITO films deposited in an oxygen atmosphere. The role of the deposition parameters used in the PLD process of these films is examined. The chapter includes a discussion of how the laser fluence affects the material properties.

- Chapter 7 demonstrates how optically induced gratings can be written in laser deposited AZO and ITO films – see Thestrup *et al.* [14,15]. In this chapter the characteristics of grating formation in the two different materials are compared. The chapter includes an introduction to holographic gratings as well as a description of the experimental setup used for the experiments.

1.4 References

1 H.L. Hartnagel, A.L. Dawar, A.K. Jain, C. Jagadish: *Semiconducting Transparent Thin Films* (Institute of Physics Publishing, Bristol 1995)

2 Z. Shen, P.E. Burrows, V. Bulovic, S.R. Forrest, M.E. Thompson: Science **276**, 2009 (1997)

3 J. Hu, R.G. Gordon: J. Appl. Phys. **71**, 880 (1992)

4 R.B.H. Tahar, T. Ban, Y. Ohya, Y. Takahashi: J. Appl. Phys. **83**, 2631 (1998)

5 K.C. Park, D.Y. Ma, K.H. Kim: Thin Solid Films **305**, 201 (1997)

6 M. Ohyama, H. Kozuka, T. Yoko: J. Am. Ceram. Soc. **81**, 1622 (1998)

7 J.P. Zheng, H.S. Kwok, Appl. Phys. Lett. **63**, 1 (1993)

8 A. Suzuki, T. Matsushita, N. Wada, Y. Sakamoto, M. Okuda: Jpn. J. Appl. Phys. **35**, L56 (1996)

9 B.-S. Chiou, S.-T. Hsieh, W.-F. Wu: J. Am. Ceram. Soc. **77**, 1740 (1994)

10 *Pulsed Laser Deposition of Thin Films*, ed. by D.B. Chrisey, G.K. Hubler (Wiley, New York 1994)

11 B. Thestrup, J. Schou, A. Nordskov, N.B. Larsen: Appl. Surf. Sci. **142**, 248 (1999) *reprint included in thesis*

12 B. Thestrup, J. Schou: Appl. Phys. A **69**, s807 (1999) *reprint included in thesis*

13 B. Thestrup, J. Schou, *AZO – a new optical material*: DOPS-NYT 4 (1999) (in Danish)

14 B. Thestrup, C. Dam-Hansen, J. Schou, P.M. Johansen: accepted for publication in J. Optics A, January 2000, *reprint included in thesis*

15 B. Thestrup, C. Dam-Hansen, J. Schou, P.M. Johansen, *Holographic Gratings Induced in Laser Deposited AZO and ITO films*, post-deadline paper in 7th topical meeting in Photorefractive Materials, Effects and Devices, June 27-30, Elsinore, Denmark (1999) pp. 31-34

2 Pulsed laser deposition of multi-component oxides

Already in the 1960s, just a few years after the first commercial Ruby laser became available, the first laser deposition experiments were performed [1]. However, it was not until almost 20 years later that scientists really became interested in pulsed laser deposition (PLD). In the late 1980s, reliable short pulsed ultraviolet (UV) lasers became commercially available and PLD proved to be efficient in growing high-quality high-temperature superconductor (HTS) films [2]. Since then the PLD technique has experienced explosive growth and researchers have studied the deposition of HTS films and other multicomponent oxide films.

The advantages of PLD are the simplicity and versatility of the experiment. With the use of a high-power pulsed UV-laser and a vacuum chamber, a variety of stoichiometric oxide films can be grown in a reactive oxygen background gas without the need for further processing.

This chapter is an introduction to the following chapters and is mainly based on Chrisey and Hubler's book on "Pulsed Laser Deposition of Thin Films" [3] and Smiths book on "Thin-Film Deposition, Principles and Practice" [4].

2.1 The pulsed laser deposition process

2.1.1 Keywords

Some keywords for the PLD technique are: *UV-laser wavelengths*, which ensure high light absorption in a relatively thin layer of the target surface. *High laser fluxes*, which give rise to high instantaneous deposition fluxes. *High kinetic energies* of the ejected particles, which give the possibility of operating in high background gas pressures of oxygen or other gases. In addition, ultra-high-vacuum conditions are not necessary.

Compared with other vacuum deposition techniques such as, e.g., sputtering and chemical vapour deposition, the PLD technique is operationally simpler, faster and more versatile. Some disadvantages of the PLD technique are that problems with particulates can occur, that large area covering is difficult and that the upper deposition rate limit is unknown.

2.1.2 The deposition process

The PLD process shown schematically in Figure 2-1 can be divided into (at least) three steps:

1. Laser - target interaction
2. Plume expansion
3. Film deposition

Here "plume" means the ensemble of particles ejected from the target following a laser pulse.

Each process step is very material dependent as well as dependent on experimental parameters such as laser wavelength, laser fluence and pulse width, background gas type and pressure, substrate type and temperature, and deposition geometry. Some typical parameters for pulsed laser deposition are listed in Table 2-1 below.

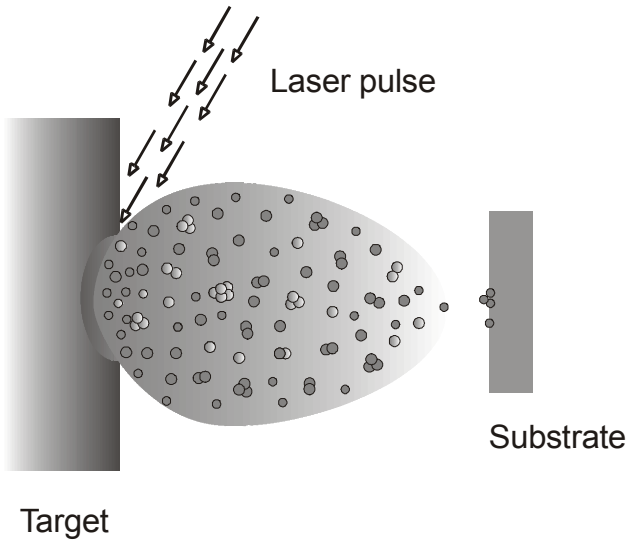

Figure 2-1 Schematic presentation of the pulsed laser deposition process. High-power laser pulses irradiate a target, material is ejected and deposited on a substrate placed nearby.

Table 2-1 Typical PLD parameters.

Parameter	***Typical values***
Materials examples (multicomponent oxides)	YBCO, BiSrCaCuO, $BaTiO_3$, ZnO, …
Laser wavelength	between 200 – 400 nm (i.e. 193, 248, 266, 308, 355 nm, etc.)
Laser pulse width	6 – 50 ns
Laser repetition rate	1 – 10 Hz
Laser fluence	0.5 – 5 J/cm^2
Vacuum pressure	~ 10^{-6} torr
Background gas	O_2, O_3, N_2O, NO_2, …
Background gas pressure	1 – 300 mtorr
Substrate examples	MgO, $SrTiO_3$, Si, Al_2O_3, glass, SiO_2, …
Substrate temperatures	25° - 750°C

The time scales involved in the three process steps are very different. Typically, the laser-target interactions occur within nanoseconds, whereas the plume expansion in a background gas takes place within microseconds. Depending on the experimental conditions, the film growth process following a laser pulse can in principle continue to develop until the next laser pulse occurs milliseconds later.

In the following sections each process step will be described separately.

2.2 Laser – target interaction

When a pulsed high-power laser interacts with a target material, the process is often referred to as ”laser ablation”. Here ”ablation” covers a variety of processes that occur during the interaction such as absorption, surface melting and vaporisation, ejection of particles, and plasma formation and expansion. If the laser power density is high enough (~ 10^9 W/cm^2), this interaction may resemble an explosion (see, e.g., [5]).

This section starts with a brief description of the laser ablation process followed by a discussion of some practical considerations regarding the laser – material interaction.

2.2.1 The ablation process

The ablation process is complex and very material dependent as well as highly dependent on laser parameters such as wavelength, pulse length and power density. A general description is complex and it is more convenient to describe a typical ablation scenario as a function of laser pulse time. A schematic presentation of the ablation process for a 30 ns long high-power laser pulse is shown in Figure 2-2.

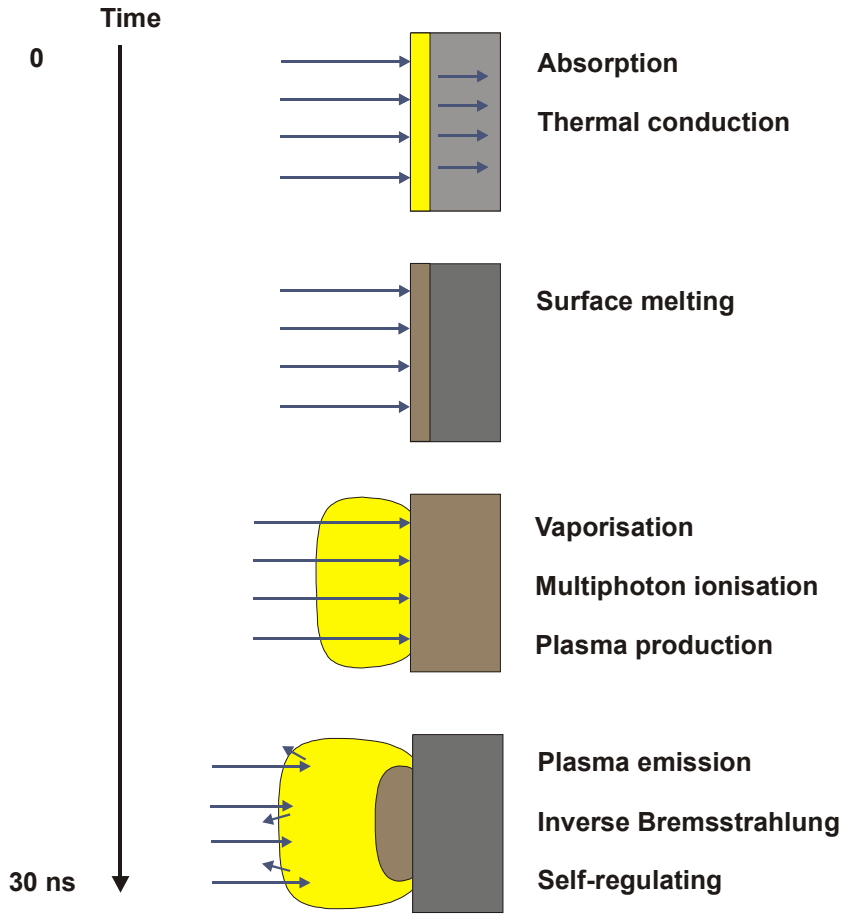

Figure 2-2 Schematic presentation of the laser target interactions during a high-power laser pulse. Adapted from reference [6].

The laser - target interaction can be divided into several stages.

- As the laser pulse hits the target, photons are immediately absorbed in a surface layer by electronic processes. The absorption depth depends on the optical penetration depth of the material, which can be in the order of a few nanometers at the vaporisation temperature [7]. The absorbed energy is transported into the material either by electrons (in metals) or by phonons (in non-metals). The energy relaxation time in metals is very fast, ~ 10^{-14} s, whereas it is much slower, ≥ 10^{-12} s, in non-metals [7,8]. However, compared with the laser pulse duration, the absorbed energy is rapidly converted into heat.
- Thereby the surface is heated beyond the melting temperature of the target material (which is, e.g., ~ 1400°C for YBCO [6]) and the surface melts.
- The melted surface starts to vaporise. The high temperatures generated at the target surface (up to several thousand degrees celcius) cause emission of many species from the target – ions, electrons, neutral atoms and molecules [6]. Further irradiation by the laser light ionises the evaporated material by single-photon and nonresonant multiphoton processes and an expanding plasma (i.e. an electrified gas of electrons, ions and neutrals that maintains quasi charge neutrality) is formed above the target surface.
- Once formed, the plasma absorbs the laser radiation by inelastic free electron scattering also called inverse-Bremsstrahlung, which results in further heating of the plasma. The absorption of the radiation by the plasma is a function of the plasma density, the plasma temperature and the laser frequency [6]. For sufficiently long laser pulses (and/or high laser power densities), the electron density above the target surface can become so dense that the plasma becomes opaque and no laser-target interaction is possible. However, as the plasma expands, it becomes less dense and the laser may again interact with the target surface and in this way a self-regulating process is established. The hot plasma also emits light, partly by Bremsstrahlung at the early stage of plume expansion [9], but also by emission from atoms, ions and molecules, which is seen as a luminous region just above the target surface [9].

As indicated above, a variety of different interactions are involved in a laser ablation process. Not only the interaction between the laser and the target has to be considered, but also laser-vapour, vapour-target, laser-plasma and plasma-target interactions play a role. Several theoretical models and model calculations that try to describe this ablation process exist – see, e.g., Phipps and Dreyfus [10], Kelly and Miotello [11], Bäuerle [12] and references within. However, the existing models usually deal with parts of the interaction only and/or with specific materials.

2.2.2 Practical considerations

Laser power density

A characteristic feature of laser ablation is the existence of a laser ablation threshold, i.e. for all materials there exists a threshold laser power density below which ablation, i.e. measurable material removal, is not possible. This threshold power density may be lower for non-metals than for metals, which is due to the poor energy transport in non-metals giving rise to higher surface temperatures during the ablation process. Typical threshold laser power densities are in the order of 10^7-10^8 W/cm^2 [6,13]. Above the ablation threshold, the ablation rate increases nonlinearly with increasing laser power density.

For optimum laser deposition, the laser power density should neither be too low nor too high. If the power density is too close to the ablation threshold, the material removal is low and non-stoichiometric transfer of target material is possible for multicomponent targets [14]. If the power density is too high, however, a large amount of the laser energy is ”wasted” in plume heating and ionisation instead of being used for heating the target surface. See the final ablation stage above.

Laser wavelength

The laser wavelengths used for laser deposition are typically between 200 and 400 nm. This is mainly because most materials used for deposition exhibit strong absorption in this spectral region. Absorption coefficients tend to increase with decreasing wavelength in this region and the optical penetration depths of the target materials are correspondingly reduced.

Wavelengths in the visible or infrared part of the photonic spectrum are problematic as they greatly enhance the inverse-Bremsstrahlung [15,16]. Below 200 nm, strong absorption of molecular oxygen can make the beam control setting in this spectral region difficult if film deposition is performed in an oxygen background gas. Furthermore, the optics is more difficult at shorter UV-wavelengths [16] as special and expensive components are needed at these wavelengths.

Target surface modifications

The laser ablation process alters the target surface topology and can change the chemical composition of the target surface as well. After several laser pulses, an initially flat target surface will typically convert to a rough surface morphology exhibiting small structures like cones, ripples or ridges [17]. In order to obtain steady state laser ablation, preconditioning (preablation) of the target is necessary [17].

In a laser deposition experiment, the laser light is usually incident at 30°-45° to the target surface. Thereby, the laser-plasma interaction is reduced and any laser-substrate interaction avoided. A drawback of this geometry is that the laser may etch a trench into the target so that the plume tilts back towards the laser beam [18].

2.3 Plume expansion

Provided that the laser power density on the target is above the threshold for plasma creation, an expanding plasma is formed above the target surface during ablation. This plasma formation threshold is typically higher than the power density threshold for laser ablation [14].

In PLD the plasma plume typically expands in a background atmosphere. However, in order to describe plume expansion in an atmosphere, some knowledge of plume expansion in vacuum is necessary. This section treats, firstly, plume expansion in vacuum and, secondly, plume expansion in a background atmosphere.

2.3.1 In vacuum

During irradiation of a target, in vacuum, with a high-power laser pulse of around 30 ns duration, a bubble of hot plasma is formed ≤ approximately 50 μm from the target surface [9]. As soon as the plasma is created, the plasma particles interact and tend to “lose memory” of the primary ablation mechanisms [11]. Thus, the plasma expansion can be described by certain characteristics, i.e.

secondary ablation mechanisms (see, e.g., [9,14]) which to some extent are independent of the primary mechanisms. The expansion characteristics are described below.

Knudsen layer formation

Initially, the density of ablated particles may be high, i.e. in the range of 10^{18} – 10^{20} cm^{-3} [14]) and, in addition, the ablated particles close to the target surface have an anisotropic velocity distribution (all velocity vectors point away from the target surface). However, this anisotropic velocity distribution is transformed into an isotropic one by collisions among the ablated particles. This happens within a few mean-free paths from the surface, a region known as the Knudsen layer [8]. It is mainly within this Knudsen layer that laser energy is absorbed in the plasma [14].

High temperatures

Estimated initial plasma temperatures for PLD materials are in the range from 5000 K to 15000 K [9].

Forward-directed plume

After the laser pulse has terminated, inter-particle collisions can lead to a highly anisotropic expansion of the plasma plume [14], which will typically be peaked in the forward direction, i.e. normal to the target surface. In a model by Singh and Narayan (see, e.g., [19]), where they model the plasma as a fluid - using the equations of gas dynamics followed by an adiabatic expansion - they show that the acceleration of the plasma varies inversely with its dimensions. Consequently, the highest velocities are obtained in the direction perpendicular to the target surface, where the initial plasma dimension is only tens of micrometers. Similar results emerge from the treatment by Anisimov *et al.* [20,21]

High expansion velocities

At PLD conditions in vacuum, typical velocities of the particles in the leading edge of the plume are in the range of $1\text{-}2\cdot10^4$ m/s. For an ablated atom or ion with a mass of 100 amu, this corresponds to a kinetic energy of ~ 50-200 eV [14]. In general, ion velocities are higher than those of neutral species [6].

Complex plume

The plume composition is complex, especially for multicomponent targets, and may change during expansion. In the first few millimeters of the plume expansion, emission from atoms and ions, multiple charged ions and possible molecules can typically be observed together with Bremsstrahlung emission in the plasma. After the first millimeters of expansion, Bremsstrahlung emission and emission from multiple charged ions are no longer observed. In absorption spectroscopy ground-state atoms and ions have been observed in the plume after the initial expansion [9].

Typically, non-emitting particles (i.e. ground-state atoms and ions) have broader velocity distributions than emitting particles at PLD conditions. The existence of fast neutrals in the plume can be explained by recombination of fast ions with electrons and/or resonant charge exchange between fast ions and neutrals. Electrons are more mobile than ions and neutrals, but are restricted from escaping the dense plasma by the strong space-charge field they build up by collectively moving away from the ions [9].

2.3.2 In a background atmosphere

In the presence of a background atmosphere the plume particles will, in addition to colliding with themselves, collide with the gas particles, which can lead to scattering, attenuation and thermalisation of the plume. Thereby, important film growth parameters such as the spatial distribution, the deposition rate, and the kinetic energy distribution of the depositing species are altered. In addition, the plume particles can react chemically with the gas particles. As in the case of plume expansion in vacuum, plume expansion in a background atmosphere can be described by certain characteristics (see, e.g., [9,22]). However, depending on the background gas pressure and/or the difference in mass between the ablated species and the background gas particles, these characteristics will vary in strength or will not occur at all. The characteristics for plume expansion in a background atmosphere are the following.

Increased fluorescense
Due to collisions on the expansion front of the plume and subsequent inter-plume collisions, an increase in fluorescence from all species compared with the expansion in vacuum can usually be observed [9].

Sharpening of the plume boundary
As the plume propagates into the background atmosphere it seems to push the background gas ahead and a sharp plume boundary may be created at the plume front. This plume sharpening indicates the formation of a shock front.

A slowing of the plume
After a few microseconds of expansion and at sufficiently high background gas pressure, the plume slows down relative to the propagation in vacuum and eventually coalesces with slower moving material [9].

Plume splitting
At intermediate background gas pressures (in the millitorr range) the plume tends to split up into a fast (collisionless) and a slow (scattered) component [6,14].

Changes in angular distribution
Collision-induced broadening of the plume may appear when the mean free path of ablated species, Λ, is less than the target-substrate distance, h. For target-substrate distances in the centimeter range, experiments (see, e.g., [23] for references) indicate that changes in angular distribution become significant when h/Λ is around 10.

Plume thermalisation
With typical PLD target-substrate distances around a few centimeters and at sufficiently high background gas pressures, i.e. ≥ approximately 100 mtorr, the plume particles can thermalise completely [14].

Chemical reactions
Reactive scattering can, e.g., result in the formation of molecules or clusters in the plume [9].

2.4 Film deposition

The film growth process, i.e. deposition of ejected target material onto a growing film, can be described by the following sequence: Firstly, the arriving particles must adsorb on the surface[1], after which they may diffuse some distance before they react with each other and the surface and start to nucleate. The way the particles nucleate may determine the structure or morphology of the growing film. Under certain circumstances (e.g. high substrate temperature) diffusional interactions within the film and with the substrate, beneath the growing film surface, may subsequently modify film composition and film properties.

In PLD, film growth is highly influenced by the process parameters. In the following, some typical film growth modes will briefly be described and subsequently some PLD growth characteristics will be discussed. Finally, different film structures will be mentioned. The following subsections are mainly based on the references [4,24,25].

2.4.1 Typical growth modes

In general, three conventional modes of nucleation and growth are considered:

1. Three-dimensional island growth called Volmer-Weber growth.
2. Two-dimensional full-monolayer growth called Frank - van der Merwe growth.
3. Two-dimensional growth of full monolayers followed by nucleation and growth of three-dimensional islands called Stranski-Krastinov growth.

The selection of one of these growth modes by a substrate-film system depends on the thermodynamics that relates the surface energies (film and substrate) to the film-substrate interface energy.

Volmer-Weber nucleation and growth

Figure 2-3 illustrates the different processes involved in the nucleation of clusters on a surface by vapour deposition of atoms.

The balance between growth and dissolution processes for a given cluster will be governed by the total free energy of a cluster, ΔG, relative to an assemble of individual atoms. In general, for three-dimensional cluster growth, ΔG will have a maximum, ΔG^*, at a critical cluster size, which means that cluster sizes above this critical size are stable.

To a first approximation *the nucleation rate* is given as the product between [the arrival rate of atoms at critical-size nucleus] and [the concentration of critical nuclei]. The former is proportional to the concentration of mobile atoms on the surface and to the surface diffusion coefficient. The latter is a strongly decreasing function of ΔG^*. As a rule, an increased cluster nucleation rate is desired in Volmer-Weber growth. In practice, this can be achieved by increasing the deposition rate (or decreasing the substrate temperature[2]) which gives a decrease in ΔG^*. Another possibility is to decrease the net surface/interface free energy (and thereby decrease ΔG^*), e.g. by creating interactions with a background gas.

1 Generally, adsorption is either by physisorption (van der Waals forces) or by chemisorption (chemical bonds with surface atoms).

2 Normally, a decrease in substrate temperature also reduces the surface diffusion coefficient.

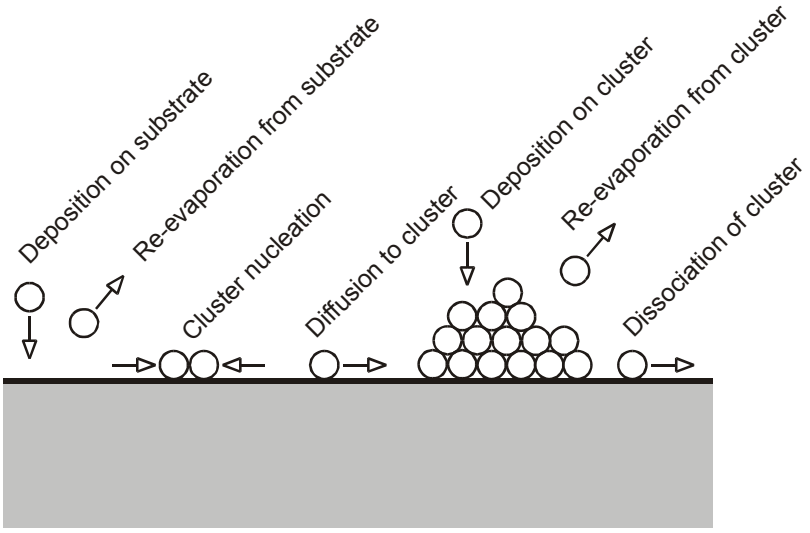

Figure 2-3 Schematic diagram of atomic processes in the nucleation of three-dimensional clusters of deposited film atoms on a substrate surface. Adopted from [24].

Frank - van der Merwe nucleation and growth
Full monolayer growth involves nucleation and growth of islands that are only one monolayer thick and grow to essential complete coalescence before significant clusters are developed on the next film layer. In this case there is no free energy barrier for nucleation (i.e. no ΔG^*). If the surface material is different from the film material, full monolayer nucleation will be promoted by strong film-substrate bonding, low film surface energy and high substrate surface energy.

Stranski-Krastinov nucleation and growth
Full monolayer growth may change to three-dimensional island growth after 1-5 monolayers due to a change in the energy situation with successive monolayers. This could e.g. be an increase in stress with increasing layer thickness due to mismatched lattice spacings.

2.4.2 Characteristics of PLD growth

Qualitatively, a possible event scheme for nucleation during a PLD cycle is as follows (assuming a high instantaneous vapour flux, see [24]):

- A vapour pulse causes the nucleation of a high density of small subcritical clusters (i.e. the clusters are much smaller that those that would be stable for a much lower instantaneous deposition rate). The subcritical clusters are expected to be unstable once the vapour pulse has decayed after approximately 1 ms.
- The subcritical clusters will tend to dissociate into mobile species.
- The mobile species will nucleate new clusters on a different scale during the time of no vapour arrival - typically 100 ms.
- The next pulse will initiate the same sequence with some of the mobile atoms being added to the clusters formed following the first pulse.

If the atomic process time constants, T_{ap}'s, (i.e. the time constants for all the relevant diffusion, accumulation and dissociation phenomena) are much smaller

than the period of the PLD cycle, T_{cycle}, the pulsed vapour arrival should not affect the final film result significantly. However, if $T_{cycle} \approx T_{ap}$, then the film formation pattern may be altered.

If the PLD is performed in a background gas e.g. oxygen, the background gas may promote stoichiometric film formation as oxide deposition. Furthermore, as mentioned above, the presence of a background gas may change film and substrate surface energies, possibly even the film growth mode. However, it is difficult to predict specific effects since they will depend on sticking coefficients, reaction rates and other factors.

According to Metev [25], the two main thermodynamic parameters that determine film growth in PLD are the substrate temperature, T_s, and the supersaturation, m, where the latter is proportional to T_s and $\ln(R_a/R_e)$. Here R_a is the actual deposition rate and R_e is the equilibrium deposition rate at temperature T_s. An increase in substrate temperature will, e.g., increase the rate of surface diffusion of the adsorbed particles. For typical PLD conditions, the actual deposition rate can be varied in a controlled manner by the experimental conditions over a wide range from $R_a \sim 10^{14}$ to 10^{22} $cm^{-2}s^{-1}$.

Other important process parameters that may influence the film growth are the flux, the energy, the ionisation degree and the type of condensing particles. Surely, the physochemical properties of the substrate are essential for film growth as well. E.g. YBCO films are typically grown on non-interacting, nearly lattice-matched crystalline substrates (such as <100> MgO, $SrTiO_3$ and $LaAlO_3$ [24]).

2.4.3 Structure development

The development of the deposited film structure changes with the amount of thermal motion that takes place during film growth and also with the amount of additional energy that is delivered to the growing surface as indicated above. According to Smith [4] important parameters are the ratio of the substrate temperature, T_s, to the melting point of the film, T_m (in Kelvin), and the distance between adsorption sites, a, compared with the diffusion length, Λ_D, of the adsorbed particles. Four main structural forms (zones) have been identified in vapor-phase processes (see also, e.g., [26]).

Zone 1

When T_s/T_m is so low that surface diffusion is negligible ($\Lambda_D < a$), the film may consist of columns typically tens of nanometers in diameter separated by voids a few nanometers across. The columns have poor crystallinity or are amorphous. In thicker films this structure may be superimposed with an array of cones with wider voids between them, which terminate in domes at the surface.

Zone T

This form is usually associated with energy-enhanced processes such as, e.g., PLD. When $\Lambda_D < a$, the film may contain defected columns similar to those of *zone 1*, but the voids and domes are absent.

Zone 2

When $T_s/T_m > 0.3$ approximately so that surface diffusion becomes significant, the film may consist of columns that have tight grain boundaries between them. The crystalline columns have less defects than in *zone 1* and *zone T* and are often facetted at the surface. The *zone 2* structure can also occur in amorphous films, where the plane boundaries are planes of reduced bonding rather than planes of crystallographic discontinuity.

Zone 3
When $T_s/T_m > 0.5$ approximately so that considerable bulk annealing of the film is taking place during deposition, the film may, under certain circumstances, consist of more isotropic or equiaxed crystallite shapes. For $T_s/T_m > 0.5$, *zone 2* and *zone 3* structures are often associated with smooth film surfaces. However, the grain boundaries can develop grooves.

In general, the "optimum" substrate temperature for high-quality thin-film growth is when $0.3 < T_s/T_m < 0.5$ approximately, where there is sufficient surface diffusion to allow surface atoms to minimise their surface energy (reach thermodynamically stable sites) [26].

2.4.4 Particulate formation

One major problem in PLD is the presence of particulates on the film surface. Particulates can, e.g., originate from liquid droplets that are expelled from the target during irradiation, from ejected protruding surface features that are mechanically removed from the target by laser-induced thermal and mechanical shock, or from cluster condensation from vapour species due to supersaturation [27]. The first particulate type is typically observed at laser power densities above 10^7 W/cm^2, and the last type is most likely observed in the presence of a background gas during film deposition [27]. Typical particulate sizes are in the micron and submicron ranges, however, for particulates formed from the vapour state the size tends to be in the nanometer range. In general, the density and the size of particulates on the deposited film surface tend to increase with increasing laser fluence and with increasing laser wavelength [27]. However, other process parameters such as laser spot size and ambient gas pressure are important as well.

2.5 Summary

PLD is a relative simple experimental deposition technique. However, the deposition process is, in fact, rather complex and in order to deposit films of optimum quality, the process parameters must be controlled in an adequate manner. The process parameters such as, e.g., the deposition rate, the kinetic energy of ablated particles and the mobility of adsorbed particles may be controlled by the experimental parameters such as, e.g., the laser fluence, the background gas pressure and the substrate temperature. The optimum process parameters, however, vary from one material to another.

PLD is an alternative film deposition technique, which is interesting primarily for deposition of multicomponent oxide materials. Indeed, within this field the technique is competitive to other vacuum deposition techniques.

2.6 References

1 H.M. Smith, A.F. Turner: Appl. Opt. **4**, 147 (1965)

2 D. Dijkkamp, T. Venkatesan, X.D. Wu, S.A. Shaheen, N. Jisrawi, Y.H. Min-Lee, W.L. McLean, M. Croft: Appl. Phys. Lett. **51**, 619 (1987)

3 *Pulsed Laser Deposition of Thin Films*, ed. by D.B. Chrisey, G.K. Hubler (Wiley, New York 1994)

4 D.L. Smith: Thin-Film Deposition: Principles and Practice (McGraw-Hill, New York 1995)

5 R.E. Russo: Appl. Spectrosc. **49**, 14A (1995)

6 J. Cheung, J. Horwitz: MRS Bulletin **17**, 30 (1992)

7 C. Körner, H.W. Bergmann in *Laser Processing: Surface Treatment and Film Deposition*, ed. by J. Mazumder, O. Conde, R. Villar, W. Steen (Kluwer Academic Publishers, the Netherlands 1996) pp. 797-808

8 M. von Allmen, A. Blatter: *Laser-Beam Interactions with Materials* (Springer-Verlag, Berlin 1995) pp. 41-43, pp.128-129

9 D.B. Geohegan in [3] pp. 115-165

10 C.R. Phipps, R.W. Dreyfus in *Laser Ionization Mass Analysis*, ed. by A. Vertes, R. Gijbels, F. Adams (Wiley, New York 1993) pp. 369-431

11 R. Kelly, A. Miotello in [3] pp. 55-87

12 D. Bäuerle: *Laser Processing and Chemistry*, (Springer-Verlag, Berlin 1996) pp. 209-228

13 J.C.S. Kools in [3] pp. 455-471

14 D.H. Lowndes in *Laser Ablation and Desorption*, ed. by J.C. Miller, R.F. Haglund (Academic Press, San Diego 1998) pp. 475-571

15 R.W. Dreyfus: Appl. Surf. Sci. **86**, 29 (1995)

16 S.M. Green, A. Piqué, K.S. Harshavardhan, J.S. Bernstein in [3] pp. 23-54

17 S.R. Foltyn in [3] pp. 89-113

18 J.A. Greer, M.D. Tabat, C. Lu: Nucl. Inst. and Meth. in Phys. Res. B **121**, 357 (1997)

19 R. K. Singh, J. Narayan: Phys. Rev. B **41**, 8843 (1990)

20 S.I. Anisimov, D. Bäuerle, B.S. Luk'yanchuk: Phys. Rev. B **48**, 12076 (1993)

21 S.I. Anisimov, B.S. Luk'yanchuk, A. Luches: Appl. Surf. Sci. **96-98**, 24 (1996)

22 D.H. Lowndes, D.B. Geohegan, A.A. Puretzky, D.P. Norton, C.M. Rouleau: Science **273**, 898 (1996)

23 K.L. Saenger in [3] pp. 199-227

24 J.S. Horwitz, J.A. Sprague in [3] pp. 229-254

25 S. Metev in [3] pp. 255-264

26 G.K. Hubler in [3] pp. 327-355

27 L.-C. Chen in [3] pp. 167-1971

3 Experimental setup and methods

This chapter describes the film deposition setup designed for the work presented in this thesis and the different methods used for film characterisation. In addition, the time-of-flight setup used for the experiments described in subsection 4.3 is presented.

3.1 Design of the deposition setup

A schematic view of the film deposition setup is shown in Figure 3-1. Photos of the deposition setup can be found in the "photogallery" placed at the end of this thesis. The setup was designed to be as flexible as possible and, therefore, most of the key deposition parameters could be varied. However, these parameters are far from independent and a comprehensive examination of all parameter variations is beyond the scope of this work. As mentioned in chapter 1, I have in this thesis focused on the influence of the background gas, the substrate temperature and, to some extent, of the laser fluence on the film properties. Table 3-1 summarises the film deposition parameters used throughout this work.

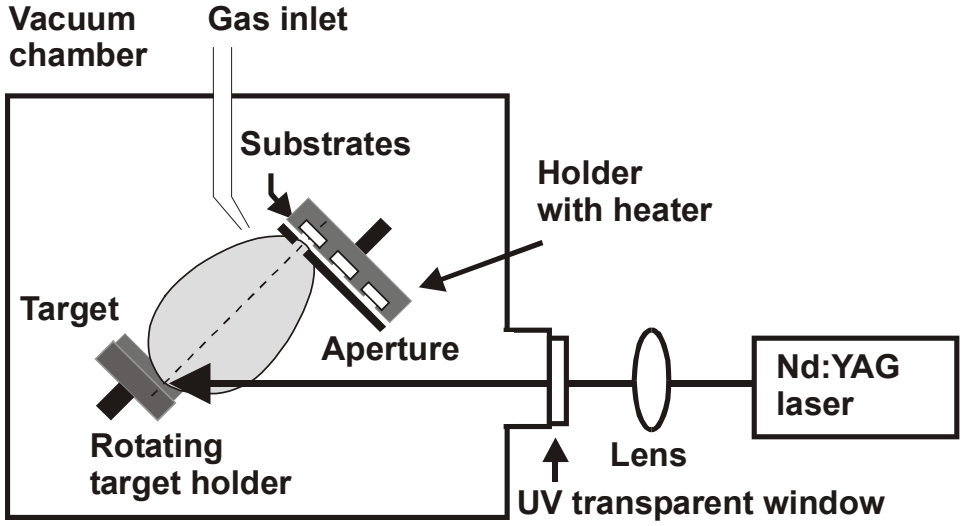

Figure 3-1 Schematic side view of the deposition setup.

The film deposition took place in a vacuum chamber held at a base pressure of around 10^{-6} torr, which is sufficient to ensure pure films at the deposition rates used in this work [1]. Basically, a ceramic target placed in a rotating target holder was irradiated with ultraviolet (UV) laser pulses from a tripled Nd:YAG laser. Thereby, ablated target material was deposited on glass substrates placed 60 mm from the target surface.

The targets were commercial ceramic sputtering targets. The indium tin oxide (ITO) targets consisted of In_2O_3 mixed with 10 wt% SnO_2 and the aluminium zinc oxide targets consisted of ZnO mixed with 2 wt% Al_2O_3. Target purity was 99.99% and 99.999%, respectively. In order to remove target surface impurities and stabilise the deposition rate, these targets were pre-irradiated in vacuum before each film deposition series. A typical pre-irradiation rate was 100 laser shots per target spot. New targets were irradiated with at least 300 – 1200 laser

shots per target spot depending on the laser fluence used. A step-motor was programmed to rotate the target during deposition. Photo 4 in the "photogallery" shows a microscope picture of an irradiated ITO target.

The glass substrates were mounted on an aluminium holder, i.e. a disc containing five substrates in total. An aperture in front of this holder ensured that only one substrate at a time was exposed to the ablation flux. The substrates were then exchanged simply by rotating the holder with another programmed step-motor. The substrate holder could be heated from 25°C up to 300°C using a canthal wire wrapped around the holder, and a feedback system ensured a constant temperature within 2%. The temperature was measured continuously during film deposition by a thermocouple. As a rule, we always cleaned the glass substrates with methanol before use.

Table 3-1 Film deposition parameters.

Parameters	***Type and/or size***		
Materials	**Target**	90wt% In_2O_3/10wt% SnO_2	**ITO**
		2wt% Al_2O_3/98wt% ZnO	**AZO**
	Substrate	**Glass**	
Background gasses		**O_2, Ne, Ar, Xe**	
Laser parameters	Wavelength	355	nm
	Repetition rate	10	Hz
	Pulse length	6	ns
	Fluence	**0.5 – 2.0**	**J/cm^2**
	Beam spot area	0.072	cm^2
Pressure parameters	Base pressure	$2 \cdot 10^{-6}$	torr
	Background gas pressure	**10^{-5} - 5· 10^{-2}**	**torr**
Target parameters	Diameter	30	mm
	Thickness	3	mm
	Rotation frequency	~ 1/60	Hz
Substrate parameters	Diameter	10	mm
	Thickness	0.17	mm
	Temperature	**25 – 300**	**°C**
Aperture dimensions	Length × width	10 × 5.5	mm^2

The laser light was directed into the vacuum chamber with a UV mirror of 88% reflectance (at 355 nm), which was also used for laser alignment. To ensure a constant irradiation fluence during film deposition, the laser pulse energy was measured before and after each film deposition with a laser power meter. Furthermore, in order to achieve the required pulse energy, the laser beam was usually attenuated by a series of glass plates (microscope slides) positioned in the beam line (see, e.g., Figure 3-5). After the mirror the laser beam was focused to a spot size of 0.072 cm^2 through a coated lens, which had a focal length of 1000 mm and was placed 600 mm from the target surface. The spot size was determined by measuring the beam spot area on the target from a single laser pulse as a function of laser energy – see appendix A. At a certain fluence threshold, this area reached a constant value which was defined as the spot size. The beam from the Nd:YAG laser was expected to have a quasi-Gaussian intensity profile. However, a few hotspots (areas of high intensity) in the intensity profile were observed.

Film deposition was typically performed in an ambient background gas, e.g. oxygen, with a pressure of up to 50 mtorr. This background gas was let into the vacuum chamber near the substrate surface through a needle valve. We used two different pressure sensors to measure the gas pressure, either a cold cathode

gauge control (range 10^{-8} to 10^{-3} mbar) or a Pirani gauge (electronically heated wire, range 10^{-3} to 10^{3} mbar). Several vacuum pumps were used in the setup; a diffusion pump, pre-pumped with a rotary pump, pumped the main chamber and another rotary pump pumped the background gas reservoir. In order to eliminate hydrocarbons in the system, the diffusion pump- and the reservoir pump systems were equipped with liquid-nitrogen traps. In general, if the glass substrates were heated during deposition, they were subsequently cooled down to room temperature at a background gas pressure of around 25 mtorr. A list of the experimental equipment is given in appendix A.

3.2 Film characterisation

In order to study the influence of the deposition parameters on the properties of the deposited films, the films were characterised in several ways. Below, the different characterisation methods are presented.

3.2.1 Film thickness and deposition rate

In this work we have used three independent methods to determine film thickness and, thus, deposition rates:

- A method involving quartz crystal microbalance (QCM) measurements.
- A method involving transmission spectra of deposited films.
- A direct thickness measurement, using an atomic force microscope (AFM).

QCM measurements

Figure 3-2 shows a schematic view of a QCM. The QCM basically consisted of a piezoelectric quartz crystal. Silver electrodes were attached on each side and were connected to an oscillating electric circuit placed outside the chamber. The quartz crystal was a commercial AT-cut crystal that was made to vibrate at the resonance frequency of its fundamental thickness-shear mode of vibration by an external field - see the figure. This resonance frequency, f_q, was around 5 MHz and was temperature independent at room temperature [2]. When material is deposited on the QCM, a decrease in frequency occurs due to the piezoelectric effect. By inserting the QCM at the substrate position it was possible to measure the film deposition rate by measuring the decrease in resonance frequency, Δf, as a function of time. A PC was used for data acquisition. An example of a QCM frequency plot is shown in appendix A, including a more detailed description of the measuring procedure.

For small mass load, i.e. $\Delta f/f_q << 1$, the following expression gives the mean mass deposition rate per unit area, D_M, in the time interval Δt as a function of the total frequency change Δf in that time interval

$$D_M = (\Delta f * C_f)/ \Delta t. \qquad (3\text{-}1)$$

Here $C_f = 1.279 \cdot 10^{16}$ amu/(Hz cm^2) is a calibration constant of the QCM. We used the mean linear deposition rate, D, instead which is determined as

$$D = D_M / (\rho_f \cdot N_A), \qquad (3\text{-}2)$$

where N_A is Avogadro's number and ρ_f is the film density, for which we chose the value given by the target manufacturer. This choice of density value is discussed further in the following chapter in connection with other problems with using QCM measured deposition rates for determining film thickness. From the linear deposition rate, the film thickness, d, of a given film is found as

$$d = D \cdot \Delta T, \qquad (3\text{-}3)$$

where ΔT is the total film deposition time.

It should be noted that the QCM method is very sensitive to laser alignment, especially at low background gas pressure. However, the method is effective for determining deposition rates, as well as film thickness for hard films thinner than around 200 nm or opaque films, where the two other measuring methods are useless. For a detailed description of the mass sensitivity of a QCM, see references [3,4].

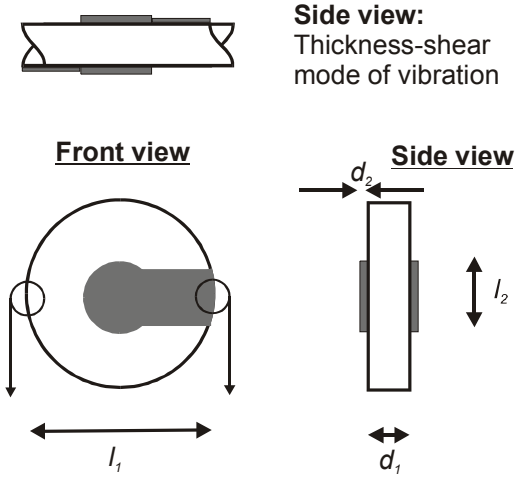

Figure 3-2 Schematic view of a quartz crystal microbalance (l_1 = 14 mm, d_1 = 0.3 mm, l_2 = 6 mm, d_2 = 4000 Å).

Film thickness from transmission spectra

Whenever it was possible, the thicknesses of the deposited films were determined from their transmission spectra (see also "*Film transmission*" below) following a method by Manifacier *et al.* [5]. For a sufficiently thick film (d > ~180 nm) ripples will occur in the transmission spectrum due to etalon interference effects produced at the air/film and film/substrate interfaces. This is demonstrated in Figure 3-3 that shows an example of a transmission spectrum for an ITO film deposited on glass. The thickness of the film can then be determined from two maxima or minima in the transmission spectrum using the following equation:

$$d = (M \cdot \lambda_1 \cdot \lambda_2) / 2[n(\lambda_1) \cdot \lambda_2 - n(\lambda_2) \cdot \lambda_1]. \qquad (3\text{-}4)$$

Here M is the number of oscillations between the two extremes and λ_1, $n(\lambda_1)$, λ_2, $n(\lambda_2)$ are the corresponding wavelengths and indices of refraction. According to the authors, the precision of the method can be estimated to

$$\Delta d/d \approx \Delta\lambda(\lambda_1+\lambda_2)/\lambda_1\lambda_2 + \Delta n/n \qquad (3\text{-}5)$$

in the case of weak dispersion of n. Equations (3-4) and (3-5) are valid in the case of weak absorption in the film. More specifically, if n_0, n_1, and $\eta=n-ik$ are the refractive indices of air, substrate and film, respectively, and we assume weak dispersion of n and k, then it is required that $k^2 << (n-n_0)^2$ and $k^2 << (n-n_1)^2$.

In principle, it should be possible to calculate the complex refractive index η of a film, at a given wavelength, from its transmission spectrum as well. In practice, however, experimental uncertainties in the spectrometric data can cause uncertainties in n and k, which make the evaluated values useless [6]. In our case, it was not possible to calculate reliable values of n and k from the ripple

amplitudes in the transmission spectra. Instead, we used a refractive index measured for ZnO at 600 nm by Craciun *et al.* [7] for AZO films, and a wavelength dependent refractive index for ITO measured by Coutal *et al.* [8] for ITO films.

As a rule, the film thickness was obtained from a spectrum as the average value of at least two independent calculations from different maxima and minima. It should be noted that determining film thicknesses from transmission spectra requires transparent films and films with thicknesses above approximately 180 nm in order to see any interference effects in the spectra.

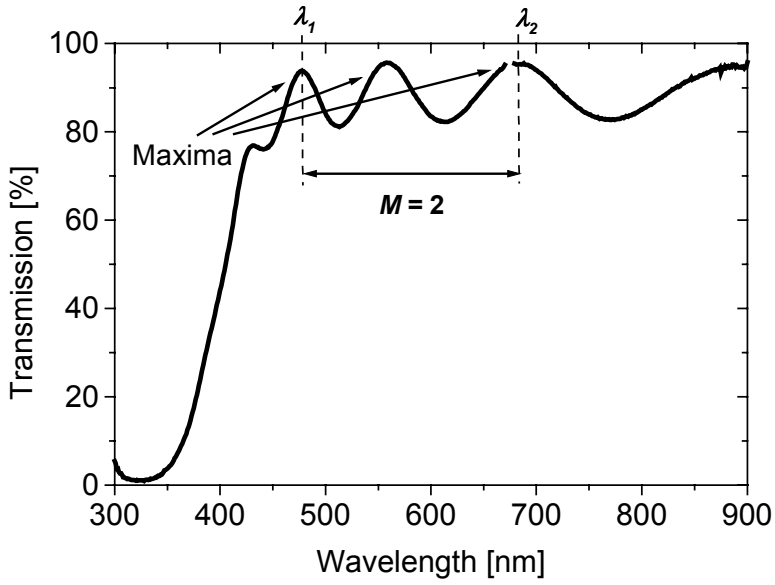

Figure 3-3 Transmission spectrum for an ITO film. The film thickness is d = 670 nm ± 8 % as calculated from the maxima (and minima) in the spectrum. The film was deposited at 25 ℃ in oxygen at 30 mtorr.

AFM measurements

An AFM, operating in tapping mode, was used as a profilometer to determine several film thicknesses. Prior to the measurement, the film was scratched across its centre. It was then possible to measure the film thickness directly by sampling across this scratch with the AFM. In contrast to the other two methods, this method gives a "point" measurement of the film thickness at the centre of the film and not an average measurement. The method is precise within few nanometers, but cannot be used for hard films where it is difficult to obtain a well-defined scratch.

3.2.2 Film sheet resistance

The electrical sheet resistance of the deposited films was determined with a linear four-point probe (Figure 3-4a). The probe consisted of four silver point contacts, which were pressed toward a film using adequate pressure. The two contacts in the centre were connected to a voltmeter with high input impedance (10^7 Ω) and the outermost contacts were connected to a current generator (giving 1 mA) in series with an ammeter.

By measuring the voltage drop with a different pair of point contacts than the pair used for current flow, the voltage drop associated with current flow through the contacts does not influence the measurement [9]. With the film dimensions

(width relative to length) chosen in our setup, the difference between the measured resistance and the actual resistance, due to sample geometry, is below 5% according to Stephens *et al.* [10]. For good accuracy, the diameter of the point contact tip, l_c, should be much smaller than the tip spacing, l_s [9]. $l_c/l_s \approx 0.1$ in our case.

According to, e.g., Hartnagel *et al.* [11], the electrical resistance, *R,* of a rectangularly shaped sample is given by

$$R = \rho \cdot (l/bd), \qquad (3\text{-}6)$$

where ρ is the electrical resistivity of the sample and l, b and d are the length, the width and the thickness of the sample, respectively – see Figure 3-4b. If $l = b$, equation (3-6) becomes

$$R = \rho/d = R_s\,, \qquad (3\text{-}7)$$

where the sheet resistance, R is the resistance of a square of the film between opposite edges and is independent of the size of this square. For equal point contact spacing and for an infinitely thin film resting on an insulating substrate, R_s is given as

$$\rho/d = R_s = (\pi/\ln 2) \cdot (V/I) \cong 4.53 \cdot (V/I), \qquad (3\text{-}8)$$

where I is the measured current passing through the film and V is the measured voltage drop.

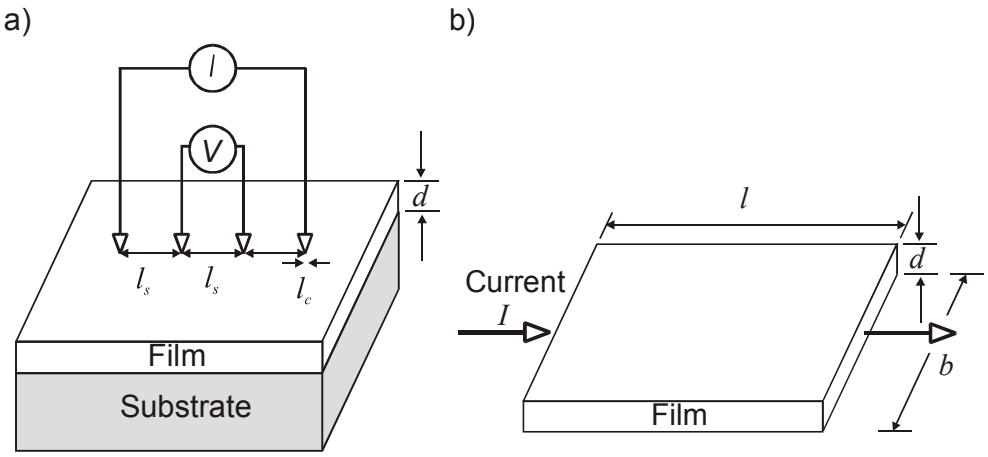

Figure 3-4 a) Four-point probe arrangement for measuring sheet resistance of a thin film. b) Geometry defining the sheet resistance of a film of thickness d, length l and width b.

As a rule, the sheet resistance for each deposited film was obtained as the average value of three independent measurements.

3.2.3 Film transmission

The transmission of visible light through each deposited film was measured with a UV/visible spectrophotometer (range 190 to 900 nm). An example of a transmission spectrum is shown in Figure 3-3. The film spectra were automatically corrected for substrate effects by inserting a reference substrate in the spectrophotometer during a measurement.

Besides measuring the light transmission through each film, the films were also analysed simply by ”visual inspection” to see their colour and gloss. Some of the films were studied in a light microscope as well. In the “photogallery”, at

the end of this thesis, some examples of microscope pictures of deposited films are shown.

3.2.4 Film structure and composition

The film surface morphology was studied with an atomic force microscope. The AFM was operating in tapping mode, which basically means that a small probe tip is vibrating above the film surface at a certain resonance frequency. By measuring the vertical movement of the tip keeping a constant tip force (which is a strong function of the tip-surface distance) while scanning the film surface, a surface picture can be formed. Examples of AFM pictures of film surfaces are shown in the "photogallery".

The film and target surface composition was examined with X-ray photoelectron spectroscopy (XPS). In XPS an incident X-ray beam can eject inner shell electrons, called photoelectrons, out of near-surface atoms in the film. By measuring the energy spectrum of these escaping photoelectrons, the chemical elements in the film can be identified (see, e.g., [12]). The peak positions in an XPS-spectrum are determined by the energy levels of the electron shells in the probed atoms in the sample. By measuring relative calibrated peak areas, relative concentrations of specific elements in a sample can be determined.

The crystallinity of the deposited films was examined by X-ray diffraction (XRD). From the X-ray diffraction measurements one can obtain knowledge about sizes of scattering vectors for a given film (see, e.g., [13]). On the basis of some facts about the macroscopic crystal symmetry, one can usually identify some of the reciprocal Bravais lattice planes. In our case, the X-ray data were used to examine whether the films were amorphous or polycrystalline.

Besides the analysing methods mentioned above, the films were scratch-tested as well – i.e. we examined film sticking to the substrate simply by scratching the films with a scalpel.

3.3 Time-of-flight setup

This section describes the setup used for time-of-flight (TOF) measurements of silver ions ablated in a neon background atmosphere. The TOF measurements give some understanding of the particle dynamics during ablation in a background atmosphere. The setup has been described previously by T.N. Hansen *et al.* [14] and is shown schematically in Figure 3-5. Basically, a 6 ns pulse from the frequency-tripled Nd:YAG laser of wavelength 355 nm irradiated a silver target at normal incidence. The target was placed in a vacuum chamber with a base pressure of around $1.2 \cdot 10^{-7}$ torr, containing a background gas of neon at low pressure (< 0.1 torr). Following the laser pulse, a TOF spectrum of ablated silver ions, ejected in the horizontal plane, was collected at an angle of 7.5° to the target normal with a moveable Langmuir plasma probe.

The laser light was focussed to a spot size of 0.040 cm^2 through a lens with a focal length of 1000 mm placed 735 mm from the target surface [15]. As for the film deposition setup, the laser light was directed into the vacuum chamber with an UV mirror and attenuated with glass plates placed in the beam line. The laser fluence was around 2.4 J/cm^2.

The vacuum chamber was equipped with a cryostat, whose outermost reservoir was filled with liquid nitrogen, and pumped with a turbo-molecular pump equipped with a liquid-nitrogen trap. The neon gas was introduced into the chamber through a needle valve in the same way as for the film deposition setup. The neon background pressure was varied between 15 and 60 mtorr.

The Langmuir plasma probe consisted of a tin-soldered copper wire with a projected area of 0.013 cm^2 at the end of an insulated cable. The active probe was biased with a fixed voltage of –30 V, which was supplied from a capacitor of 1 μF. This bias voltage is sufficient to reject all the plasma electrons and give the saturated ion signal. The collected ion current was determined from the voltage signal across a 25 Ω resistor. This voltage signal from the ion probe was collected with a digital oscilloscope that was triggered from the laser (when emitting a laser pulse). The probe-target distance could be varied from 40 to 80 mm from outside the chamber.

Before the measurements were performed, the silver target (purity 99.9%) was pre-irradiated with 30 laser pulses in order to remove a possible oxide layer from the surface and to ensure a constant ablation rate [16].

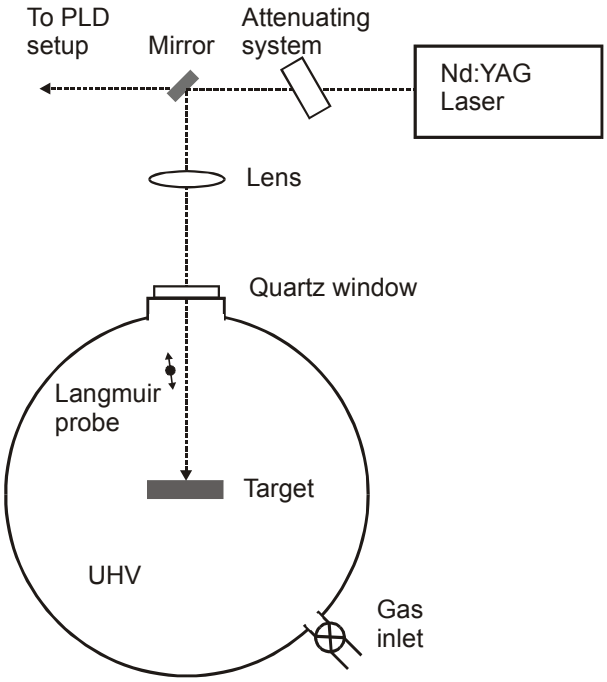

Figure 3-5 Schematic top view of the time-of-flight setup.

3.4 Summary

In this chapter the film deposition setup and the experimental parameters used for film deposition have been described. The main experimental parameters of interest in this work, i.e. for deposition of indium tin oxide and aluminium doped zinc oxide films on glass, are the type of background gas used, the background gas pressure, the substrate temperature and the laser fluence.

In addition, various film characterisation methods have been mentioned in this chapter. These characterisation methods have been used to determine essential film and deposition properties such as the film thickness and deposition rate, the electrical sheet resistance and the film transmission, as well as the film structure and composition.

3.5 References

1 G.K. Hubler in: *Pulsed Laser Deposition of Thin Films*, ed. by D.B. Chrisey, G.K. Hubler (Wiley, New York 1994) pp. 327-355

2 *Applications of Piezoelectric Quartz Crystal Microbalances*, ed. by C. Lu, A.W. Czanderna (Elsevier, Amsterdam 1984)

3 H.K. Pulker, J.P. Decosterd, in [2] pp. 63-123

4 B. Thestrup, *Sputtering of solid D_2 with keV electrons: Dependence on yield from film thickness*, Master Thesis in Danish (University of Copenhagen, 1994)

5 J.C. Manifacier, J. Gasiot, J.P. Fillard: J. Phys. E: Scientific Instr. **9**, 1002 (1976)

6 I. Hamberg, C.G. Granqvist: J. Appl. Phys. **60**, R123 (1986)

7 V. Craciun, S. Amirhaghi, D. Craciun, J. Elders, J.G.E. Gardeniers, I.W. Boyd: Appl. Surf. Sci. **86**, 99 (1995)

8 C. Coutal, A. Azéma, J.-C. Roustan: Thin Solid Films **288**, 248 (1996)

9 D.L. Smith: Thin-Film Deposition: Principles and Practice (McGraw-Hill, New York 1995)

10 A.E. Stephens, H.J. Mackey, J.R. Sybert: J. Appl. Phys. **42**, 2592 (1971)

11 H.L. Hartnagel, A.L. Dawar, A.K. Jain, C. Jagadish: *Semiconducting Transparent Thin Films* (Institute of Physics Publishing, Bristol 1995)

12 L.C. Feldman, J.W. Mayer: *Fundamentals of Surface and Thin Film Analysis* (Elsevier Scientific Publishing, New York 1986)

13 N.W. Ashcroft, N.D. Mermin: *Solid State Physics* (W.B. Saunders Company, Philadelphia 1976)

14 T.N. Hansen, J. Schou, J.G. Lunney: Appl. Surf. Sci. **138-139**, 184 (1999)

15 T.N. Hansen, *UV laser ablation of metals in vacuum* (Master Thesis in Danish, University of Copenhagen, 1997) p. A.1-4

16 T.N. Hansen, J. Schou, J.G. Lunney: Europhys. Lett. **40**, 441 (1997)

4 Deposition rates for ITO and related time-of-flight measurements

As mentioned in chapter 2, the expansion of the laser-generated plume in pulsed laser deposition (PLD) and the related film deposition rate depend strongly on the experimental parameters during film growth. The main experimental parameters of interest in this thesis are the laser fluence, the type and pressure of the background atmosphere and the substrate temperature.

The first section of the present chapter deals with experiments where the influence of these parameters on the mean deposition rate of ITO is examined. In the second section the accuracy of the experimental method used in these experiments is discussed, including a discussion of film density. Finally, the third section is devoted to related time-of-flight measurements of silver ions ablated in neon, which give some understanding of the particle dynamics during ablation in a background atmosphere.

4.1 Deposition rates for ITO

4.1.1 General remarks

An important process parameter in thin film deposition is the mean deposition rate, D, as it determines how fast a film grows. Furthermore, PLD is characterised by its high instantaneous deposition rate, D_I, which determines the degree of supersaturation and, thus, the nucleation during film growth as described in section 2.3. Table 4-1 compares the estimated typical deposition rates for ITO used in our experiments with deposition rates from other standard vacuum techniques.

As an example a mean deposition rate of approximately 1.3 Å/s corresponds in our case to depositing one monolayer per second or 0.1 monolayer per laser pulse (assuming one monolayer corresponds to 10^{15} particles/cm^2 and using a mean particle mass for ITO of 55 amu). In addition, for an instantaneous deposition rate, D_I, of around 10^4 Å/s and a background vacuum pressure of $2\cdot10^{-6}$ torr, which are typical of this work, the corresponding pressure/deposition rate ratio is $2\cdot10^{-10}$ torr/Å/s. According to Hubler [1] a pressure/deposition rate ratio of $< 10^{-7}$ torr/Å/s must be achieved to obtain pure films. Consequently, impurities in the deposited films should not be a problem.

Table 4-1 ITO deposition rates, D, for selected vacuum deposition techniques.

Deposition technique	*D [Å/s]*	*Reference*
PLD - this work	**1 – 15** ($D_I \approx 10^3$ - $2\cdot10^4$)	[2,3]
Sputtering	2 – 20	[4,5]
Vacuum evaporation	1 – 5	[6]
Chemical vapour deposition	0.2 – 0.3	[5]

4.1.2 Laser fluence effects

Figure 4-1 shows an example of how the mean (thickness) deposition rate, *D*, of ITO changes as a function of the laser pulse energy for laser deposition in two different background gases, oxygen and argon. *D* was measured using a quartz crystal microbalance (QCM, see subsection 3.2.1), and the background gas pressures were maintained at a constant value during the measurements. The laser pulse energy range was within 15 to 66 mJ/pulse corresponding to a fluence range of 0.21 to 0.92 J/cm^2.

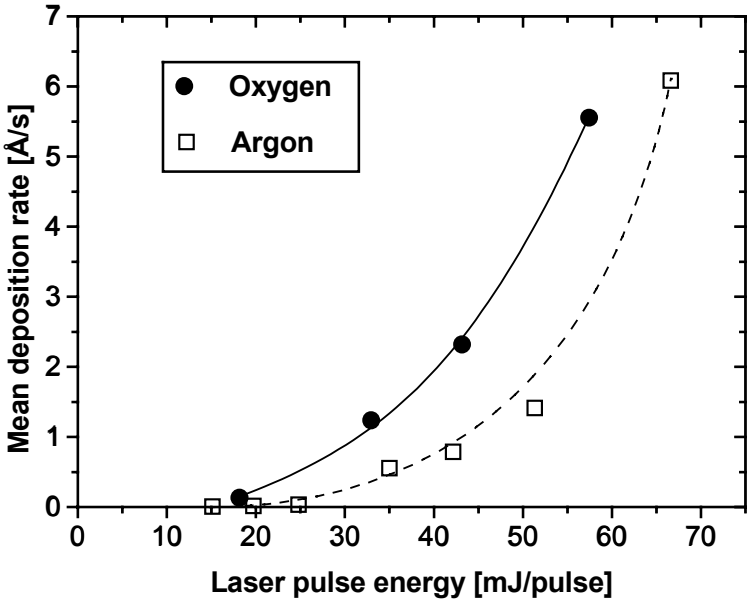

Figure 4-1 Mean deposition rate versus laser pulse energy for ITO deposited at room temperature in 26 mtorr of oxygen or 27 mtorr of argon. Lines are for guidance only.

Obviously, the change in deposition rate with increasing laser pulse energy is highly non-linear for both background gases. Such behaviour is not surprising as the measurements are performed above the ablation threshold at relatively low laser power densities (0.35-1.5·10^8 W/cm^2), where the ablation rate increases non-linearly with increasing laser power density as mentioned in section 2.1. Similar non-linear behaviour versus laser fluence has been observed in, e.g., the ablation yield of ^{58}Ni in an experiment by Preuss *et al.* [7], where thin Ni films were ablated with a KrF laser (248 nm, 0.5 ps).

The ablation threshold power density is not a specific subject of this thesis. However, the lowest deposition rate measured in our experiments was *D* = 0.007 Å/s, which was obtained at ablation in argon with a laser pulse energy as low as 15 mJ/pulse. This energy corresponds to a laser fluence of 0.21 J/cm^2 and a power density of 0.35·10^8 W/cm^2. In comparison, Lunney *et al.* [8] measured the etching threshold to be 0.5 J/cm^2 for a 150 nm thick ITO film on glass ablated with an excimer laser (248 nm, 23 ns). This corresponds to an ablation threshold power density of 0.22·10^8 W/cm^2, which is close to the lowest power density used in our experiment. Szörényi *et al.* [9] measured the laser ablation threshold for a 500 nm thick ITO film on glass ablated with a KrF laser (248 nm, 23 ns). They found the threshold to be at a laser power density around

$0.18 \cdot 10^8$ W/cm^2. Coutal *et al.* [10] reported an ablation fluence threshold of 0.3 J/cm^2 by irradiation of an In_2O_3:SnO_2 target (of the same kind that was used in this work) with an ArF laser (193 nm). However, they did not indicate the laser pulse length.

Another striking feature in Figure 4-1 is the significantly lower deposition rate in argon than in oxygen at similar pulse energies. In a similar experiment Afonso *et al.* [11] compared the number of atoms deposited on a substrate (with a setup geometry similar to the one used in this work) during ablation of a $Bi_2Sr_2Ca_1Cu_2O_8$ target in 0.1 mbar (75 mtorr) of oxygen or argon at a specific laser fluence. They observed equivalently that the number of deposited atoms is significantly lower in argon than in oxygen. The lower deposition rate in argon can partly be explained by an increased scattering of the ablated species in argon relative to oxygen. An increased scattering is expected in argon as the mass of an argon atom exceeds the mass of an oxygen molecule. Furthermore, in collisions involving molecules the amount of possible inelastic scattering processes is enhanced. Particle scattering is further discussed in section 4.3.

In the case of a reactive background gas such as oxygen, the chemical effects induced by the ambient gas may be important for the deposition rate as well. Especially at the substrate surface may the oxygen background gas assist in incorporating oxygen into the growing film. In contrast, gas-phase dissociation of molecular oxygen into atomic oxygen is not expected to be of significant importance for the deposition. The bond dissociation energy of molecular oxygen is high (5.11 eV [12]) and the average electron energy in the plasma for typical laser fluences has been estimated to be in the range of 2-4 eV (see [12] for reference) which is not sufficient to dissociate O_2. Still, some O_2 dissociation may take place as a small amount of high-energetic electrons exist in the plasma.

4.1.3 Background gas effects

Figure 4-2 shows examples of mean deposition rates of ITO measured in the four different background gases, oxygen, neon, argon and xenon, as a function of background gas pressure.

Originally, the experimental data were obtained at laser pulse energies between 27-36 mJ/pulse. However, in order to compare the different deposition rates, they have been calibrated to a pulse energy, E, of 35 mJ/pulse using experimental D versus E curves as the ones in Figure 4-1[3]. In the case of xenon an upper deposition rate limit for pressures above 20 mtorr is indicated instead. This limit is based on deposition rate measurements at a laser pulse energy of 49 mJ/pulse. The scattering of the data points at low pressures (below 10 mtorr) is a laser alignment effect. Laser alignment effects are discussed in subsection 4.2.3.

As expected, the deposition rate tends to decrease with increasing background gas pressure for a given background gas. Zheng and Kwok [13] observed similar behaviour by deposition of ITO in oxygen at room temperature, where they had determined the deposition rate from film thickness measurements. As discussed in section 2.2, an increase in background gas pressure will broaden the angular distribution of the ablated plume due to collisions between the ablated species and the background gas particles. This again leads to a decrease in the deposition rate measured by the QCM due to the finite width of the deposition area. The change in angular distribution of the plume with background gas pressure is briefly discussed in section 4.2.

3 In the calibration, a linear dependence between D and E within the energy range 25 to 40 mJ/pulse was assumed.

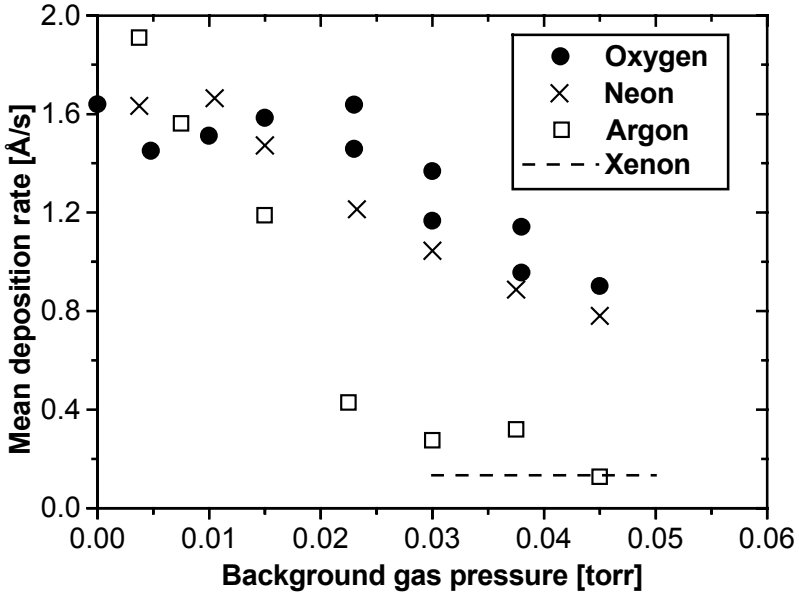

Figure 4-2 Mean deposition rate of ITO versus background gas pressure for deposition in various gases at 25°C. The data have been calibrated to a laser pulse energy of 35 mJ/pulse – except for xenon data (see text).

Collision-induced broadening is expected to become significant when h/Λ is around 10, where h is the target-substrate distance and Λ is the mean free path of ablated species (see section 2.2). In our case h = 60 mm which means that on average Λ should be around or less than 6 mm for this to be fulfilled. The mean free path of a fast ion, Λ_{ion}, penetrating through a gas is given by [14]

$$\Lambda_{ion} = (\pi a_e^2 n)^{-1}, \qquad (4\text{-}1)$$

where a_e is the effective collision diameter of a gas particle and n is the molecular concentration of gas particles. For an ideal gas $n = p/(k_B T)$, where p, k_B and T are the gas pressure, Boltzmann's constant and the absolute temperature, respectively.

Using equation (4-1) above and collision diameters from Table 4-2 in section 4.3, this means that, as a rough estimate, collision-induced broadening should become significant (in our case) when the gas pressure is around 26 mtorr in neon, 13 mtorr in argon and 7.2 mtorr in xenon. This is under the assumption that an ablated ion has the same diameter as the scattering gas particle under consideration which is not completely true. Scattering of ions is further discussed in section 4.3. However, it is indeed reasonable to explain the decrease in deposition rate with increasing pressure (Figure 4-2) simply by plume broadening, at least for the inert gases.

Focusing on the inert gases, another striking feature in Figure 4-2 is that the deposition rate for a given background gas pressure (above 0.010 torr) tends to depend on the mass of the background gas particles. Again, this is probably a plume broadening effect. Intuitively, one expects a high-mass scattering gas as, e.g., xenon to have a larger effect on the plume particle trajectories than a low-mass scattering gas as, e.g., neon, which again may affect the deposition rate.

4.1.4 Substrate temperature effects

Concerning the relation between the ITO deposition rate, D, and the substrate temperature, T_s, a preliminary deposition experiment in 23 mtorr of oxygen at a laser fluence of 1.8 J/cm^2 was performed [15]. Two ITO films were deposited during five minutes of ablation on substrates held at T_s = 200°C and T_s = 25°C, respectively. Then the thickness of the films was measured (using their transmission spectra – see equation (3-3)) and compared. Apparently, there was no significant deviation in thickness between the two films which suggests that the ITO deposition rate, D, (in oxygen) is independent of substrate temperature at ablation with a laser fluence of 1.8 J/cm^2.

4.2 Accuracy of the experimental method

In the previous section results from deposition of ITO on a QCM were presented. However, the accuracy or reliability of the experimental method was not discussed. In order to use the deposition rate results in a calculation of the thickness of ITO films deposited on glass, it is necessary to consider four basic questions:

- Is the ITO sticking coefficient on the silver electrode (of the QCM) equal to the ITO sticking coefficient on the glass substrates?
- Is the ITO film density constant and independent of deposition parameters such as, e.g., the background gas, the gas pressure, the substrate temperature and the laser fluence?
- Is the ITO deposition rate stable during film deposition?
- May possible laser misalignment and possible plume bending caused by the target trench affect the ITO deposition?

4.2.1 Sticking coefficient and film density

Regarding the first point it seems reasonable to assume that the sticking of ITO on silver is approximately the same as the sticking of ITO on glass (at room temperature). In both cases ITO is deposited on an amorphous substrate of a different material type. However, no measurements of the sticking coefficients have been performed in this work.

Concerning the second question a comparison between ITO deposition rates measured with the QCM and deposition rates calculated from atomic force microscope (AFM) film thickness measurements has been performed. The results for deposition of ITO in the four different background gases are shown in Figure 4-3. The laser fluence was 0.5 J/cm^2 and the data points are average values for the pressure range of 5 to 30 mtorr, except for xenon where the QCM value is taken from above and the AFM value is for ITO deposition at 3.8 mtorr. The reason for using average values is to reduce the influence from laser alignment effects.

In general, there is very good agreement between the deposition rates measured with the QCM and with the AFM. The agreement is within the relative uncertainties which are at most ± 9% (for the average values). This suggests that at deposition of ITO at 25°C at a pressure around 5 to 30 mtorr, and at this specific fluence, the film density is constant within a few percent independently of the type of background gas used. The deviation in film density from the value given

by the target manufacturer is expected to be 10% at most under these circumstances[4].

Concerning the relation between ITO film density and substrate temperature, at a laser fluence of around 0.5 J/cm^2, preliminary experiments indicated that the film density is higher for films deposited at T_s = 200°C than for films deposited at T_s = 25°C (in oxygen, neon and argon). The experimental procedure was the following: For each of the three background gases, two ITO films were deposited onto the silver electrodes of two different quarts crystals during four minutes of ablation at a background gas pressure of 23 mtorr. The crystals were mounted in a specially designed holder and the first film was deposited at T_s = 200°C and the second film at T_s = 25°C. The mass deposition rate, D_M, was then calculated from each film by comparing the resonance frequencies of the quartz crystal microbalances measured before and after film deposition (using equation (3-1)).

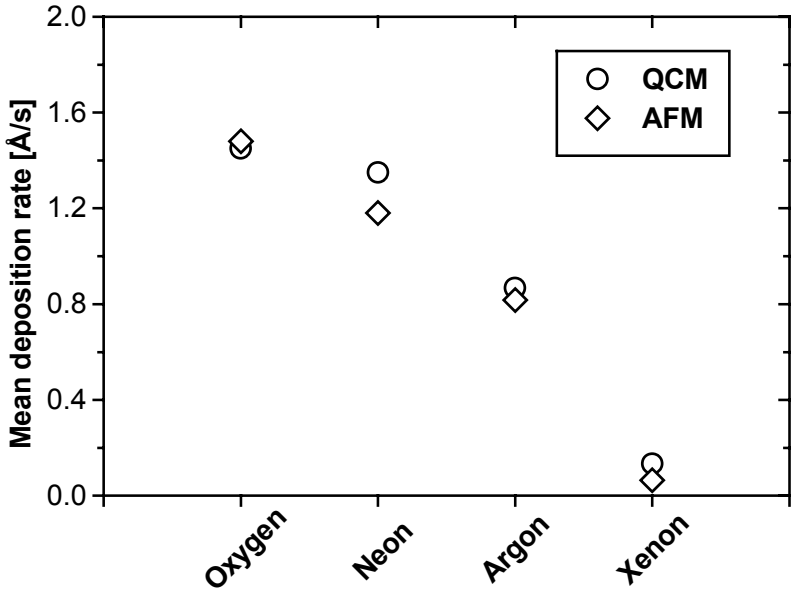

Figure 4-3 Mean deposition rates for ITO deposition at 25°C in different background gases. Fluence: 0.5 J/cm^2. The points are average values for the pressure range 5 to 30 mtorr, except for xenon (see text). Circles: QCM measurements. Diamonds: Deposition rates calculated from AFM film thickness measurements.

The measurements indicated a significant relative decrease in D_M with decreasing substrate temperature (from T_s = 200°C to T_s = 25°C), which was 27% in oxygen, 39% in neon, and 49% in argon. These values probably highly overestimate the actual change in D_M with decreasing substrate temperature, and it is indeed necessary to perform an additional, independent experiment to prove or disprove these results. Especially when the experimental difficulties are considered, i.e. the quartz crystals had been heated which could affect their performance, and the experiment involved two separate frequency measurements of the same crystal in an external setup, not a continuous measurement.

4 A deviation in the deposition rate of 9% between the QCM and the AFM measurements corresponds to a deviation in the film density (from the real value) of at most 10%.

Nevertheless, if we assume that the substrate temperature has an effect on the mass deposition rate, D_M, but not on the thickness deposition rate, D (as indicated in subsection 4.1.3 above), it means that the film density is substrate temperature dependent as well. As was also indicated above, the film density may therefore be higher at T_s = 200°C than at T_s = 25°C at the particular laser fluence used in this experiment.

No measurements have been performed in this work concerning the connection between ITO film density and background gas pressure or laser fluence.

4.2.2 Deposition rate stability

The third question concerns the stability of the deposition rate during film deposition. Figure 4-4 shows an example of a QCM experiment, where the deposition rate, as a function of time, was measured during approximately four minutes of ITO ablation in oxygen. The QCM frequency was measured with time steps of three seconds. The deposition rate, D, was then calculated at each time step from the mass deposition rate, D_M, using time intervals of Δt = 6 s (see equations (3-1) and (3-2) in chapter 3).

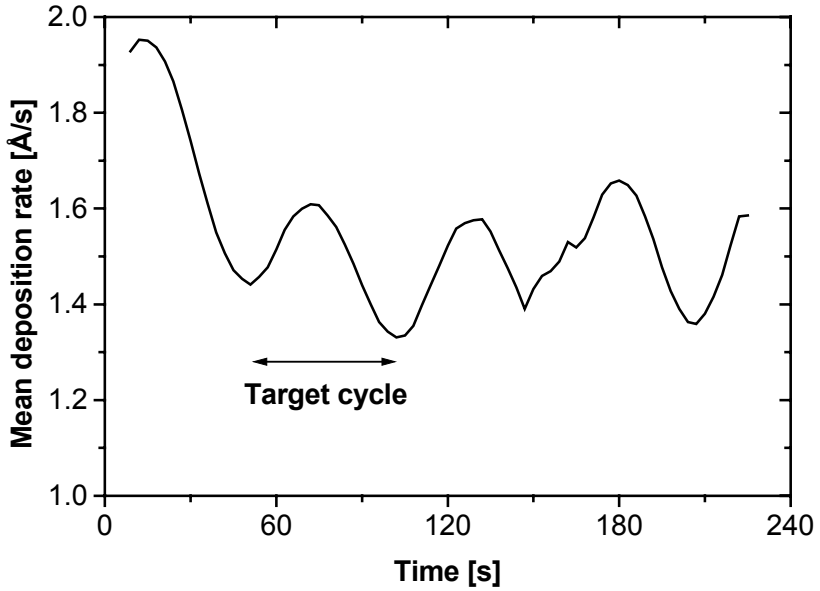

Figure 4-4 Mean deposition rate versus time during ablation of ITO in oxygen, measured by the QCM. Fluence: 0.43 J/cm^2. Oxygen pressure: 23 mtorr.

Obviously, Figure 4-4 demonstrates that the deposition rate changes not only monotonically with time but also, within a target cycle, with the target position. However, on average the deposition rate remains almost constant (D ~ 1.5 Å/s) after one target cycle. From previous ablation measurements on pure silver targets at normal laser incidence [16] it is known that around 20 laser shots on a target spot are necessary to achieve a constant deposition rate at the fluence used. In our case this corresponds to approximately one target cycle period of deposition[5], which explains the decrease in the average deposition rate from the

5 At a laser repetition rate of 10 Hz, a laser spot size of 0.072 cm^2 and a radius of 10 mm for the ablation circle on the target, the minimum number of laser shots on each target spot is 23 per full target rotation.

first target cycle period to the next in Figure 4-4. This effect has been taken into account in all deposition rate measurements used in this thesis.

The relative variation of the deposition rate within a target cycle is around 10% in Figure 4-4. The oscillations in the figure are probably caused by small oscillations in the target normal (during target rotation) relative to the QCM normal. Such oscillations may be due to a slight mismatch between the rotation axis of the step-motor and the target holder (i.e. the target holder is placed askew on the step-motor axis). Small oscillations in the target normal cause small oscillations in the plasma plume relative to the QCM normal, which again affect the deposition rate. However, as all film deposition experiments in this work are performed within several target cycles, it should not affect the film thickness calculations significantly.

4.2.3 Laser alignment and target trench effects

The fourth question mentioned at the beginning of section 4.2 concerns laser alignment and target trench effects. Possible laser misalignment and possible plume bending caused by the target trench (see, e.g., subsection 2.1.2) may influence the deposition rate, especially at low background gas pressure, where the plasma plume is narrow. Experiments from two different groups [17,19] confirm that at the background gas pressures used throughout this work the angular distribution of the plasma plume changes significantly with the background gas pressure.

The first experiment dealt with measurements of the angular distribution of plume particles, both ions and neutrals, at ablation of a pure silver target at normal laser incidence in an oxygen background gas by Hansen *et al.* [17]. The measurements were made under similar experimental conditions as the QCM measurements except that a slightly higher fluence of 2.5 J/cm^2 was used at normal laser incidence and the target-probe distance was 80 mm. However, according to previous ablation measurements of silver in vacuum [16,18], the angular distribution of the plume particles is almost constant for fluences between 0.8 to 2.5 J/cm^2, and no significant change in the angular distribution is observed when the laser incidence is changed from normal to oblique. The ion measurements in oxygen indicated that at an oxygen pressure of 15 mtorr, the major part[6] of ablated ions was within an angular spread of approximately 46° and within these 46° the ion distribution was highly non-linear, i.e. most of the ions travelled in the forward direction. At a slightly higher oxygen pressure of 38 mtorr the angular spread had increased to approximately 68°. For comparison, the spread was only 35° in vacuum. The measurements of the angular distribution of neutrals showed similar trends; however, the angular spread seems to be wider than that for the ions.

The second experiment by Ma *et al.* [19] treated angular distribution profiles of lead in PZT films deposited by laser ablation. They used an excimer laser (308 nm, 10 ns), a fluence of 4 J/cm^2, and a target-substrate distance of 50 mm. Their results indicated that at a gas pressure of 50 mtorr (oxygen or argon) and substrates at room temperature, the major part (1/e value) of the lead was deposited within an angular spread of around 40°, and within these 40° the lead abundance was highly non-linear (which was actually not the case for films deposited at 200 mtorr).

In our setup the angular spread of the deposition area is roughly 5° corresponding to a film width of 5.5 mm. Thus assuming a continuous deposition, a

6 The angular spread in which the particle signal decreases from its maximum value (normal to the target) to e^{-1} times this maximum value.

laser misalignment of 3 mm, which is not atypical, would cause the central part (5°) of the plasma plume to miss the substrate. At low background gas pressures where the particle flux is concentrated in the forward direction this may affect the deposition rate significantly. Correspondingly, possible plume tilting caused by target trench effects during ablation may cause deviations in the deposition rate. A plume tilting of 3° would also cause the central part of the plasma plume to miss the substrate. In addition, since the particle flux distribution is pressure dependent, this deposition rate deviation becomes pressure dependent as well, as discussed by Greer *et al.* [20].

4.2.4 Experimental uncertainties

The QCM provides an excellent method for film thickness determination for hard films that are either opaque or have thicknesses below around 180 nm (as mentioned in chapter 2). However, for films deposited at low background gas pressures, i.e. below approximately 15 mtorr, the estimated film thicknesses are only correct within 50% considering the uncertainties in the deposition discussed above. For pressures above 15 mtorr the film thicknesses, calculated from QCM deposition rate experiments, can be considered to be correct within 30%.

4.3 Time-of-flight measurement of silver ions ablated in a neon environment

Section 4.1 treated the deposition rate during film growth, which is connected to the final step (step 3) in the pulsed laser deposition process described in chapter 2. This section deals with the previous step in the process, i.e. the plume expansion (step 2) and, therefore, the dynamics of the plume particles following a laser pulse (see section 2.2). More specifically, in this section silver ion time-of-flight (TOF) measurements in a neon background gas from a single laser pulse are presented. The measurements are an extension of a general TOF study on silver ions ablated in gases at low pressure [21].

A silver ion has almost the same mass and covalent radius as an indium or a tin ion, see Table 4-2. Consequently, it is reasonable to assume that the dynamics of silver ions that penetrate through a neon gas is similar to the dynamics of indium and tin ions ablated in neon from an ITO target.

The experimental setup is described in section 3.3. Basically, TOF spectra of ablated silver ions were collected at an angle of 7.5° to the target normal in the horizontal plane with a moveable ion plasma probe. The laser fluence was around 2.4 J/cm^2. In Table 4-2 some constants relevant to this section are listed.

Table 4-2 Particle mass, collision diameter, and covalent radius.

Particle	***In***	***Sn***	***O***	***O_2***	***Ne***	***Ar***	***Xe***	***Ag***
Mass [amu]	114.82	118.69	15.999	31.991	20.183	39.948	131.30	107.87
Collision diameter$^{\Delta}$ [Å]	-	-	-	3.55	2.54	3.58	4.78	-
Covalent radius of ions* [Å]	1.44	1.41	0.73	-	-	-	-	1.53

$^{\Delta}$ *Reference [22]. The collision diameters have been calculated from the viscosity.*
* *Reference [23].*

4.3.1 Time-of-flight in neon

Figure 4-5 shows some examples of the ion TOF spectra for various neon pressures at a target-probe distance of 80 mm. The vacuum spectrum is given as well (high probe currents are not included).

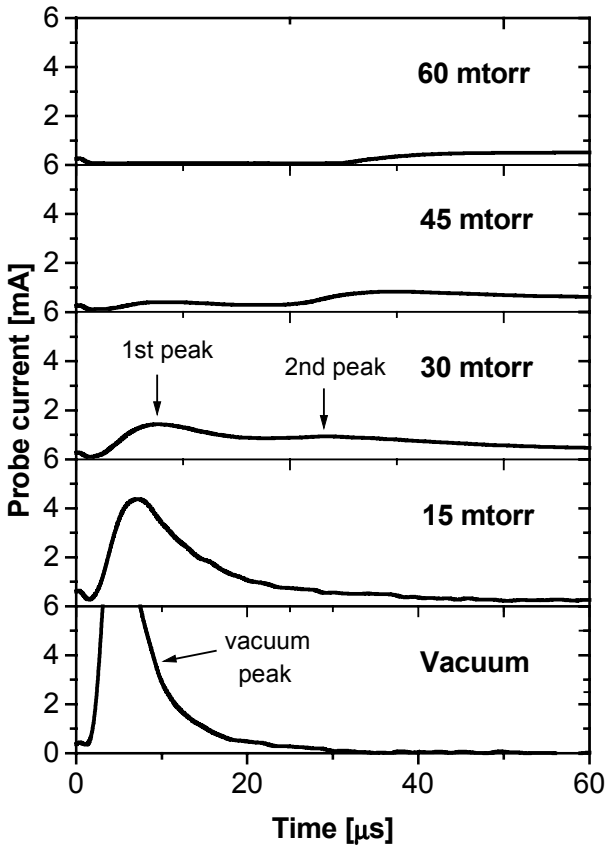

Figure 4-5 Time-of-flight spectra of silver ions ablated in a neon atmosphere at various pressures. Target-probe distance: 80 mm. Laser fluence: 2.4 J/cm^2.

The spectra demonstrate some typical characteristics of plume expansion during pulsed laser deposition – see section 2.2. In vacuum where the ions are not scattered by a background atmosphere, the majority of the ions arrive after 3 to 8 μs at the probe. This corresponds to ion velocities of $1 - 2.7 \cdot 10^4$ m/s, which are typical velocities for particles in the leading edge of the plume. As the neon pressure increases, the "vacuum" ion peak is broadened due to ion-background gas interactions and, furthermore, the peak is delayed relative to the vacuum signal. At a neon pressure of 30 mtorr, plume splitting is observed and the TOF spectrum now contains two peaks. The first peak results from fast silver ions that are not scattered at all or only scattered into small angles, and the second peak results from silver ions that have undergone significant slowing down as discussed in subsection 2.2.2. This second peak becomes completely dominant at a neon pressure of 60 mtorr.

The velocity behaviour of the first and second ion peaks is examined at a neon pressure of 45 mtorr in Figure 4-6 that gives the relation between the target-probe distance, R_{TP}, and the peak times, t_p.

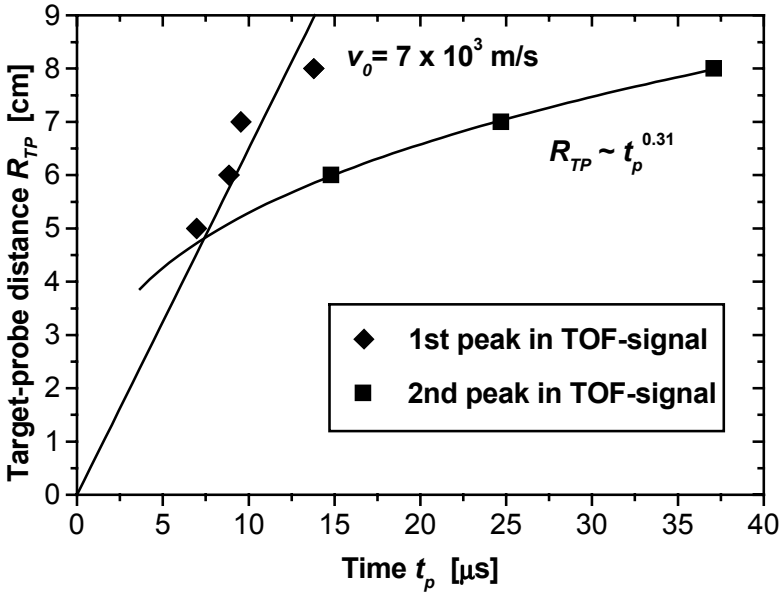

Figure 4-6 Target-probe distance, R_{TP}, versus peak time, t_p, for the two ion peaks in the TOF spectra for silver ions ablated in neon at 45 mtorr. Laser fluence: 2.4 J/cm^2. Fits to the 1st and 2nd ion peaks are indicated in the figure. v_0: Velocity of the 1st peak.

The first ion peak seems to expand almost at a constant velocity of $v_0 \approx 7 \cdot 10^3$ m/s as indicated by the linear curve fit in the figure. The second ion peak decelerates as the plume expands, and the expansion is found to be well described by $R_{TP} \propto t_p^{0.31}$ within the target-probe distance range examined. Similar experiments in 45 mtorr of oxygen and argon gave exponents of 0.32 and 0.36, respectively [21]. A blast wave model, developed to describe the propagation of a shock wave through a background gas (see e.g. [24]), predicts an exponent of 0.4. However, e.g. Geohegan [25] found exponents varying from 0.54 at 50 mtorr to 0.45 at 300 mtorr for ablation of YBCO in oxygen with a KrF laser operating at 2.5 J/cm^2. He did, however, have a target-probe distance of only 20 mm and therefore observed one ion peak only. In addition, he could not distinguish between the different ions. M. Ohkoshi *et al.* [26] found an exponent of 0.33 at 66 Pa (~ 500 mtorr) for ablation of iron in a nitrogen atmosphere with a KrF laser (248 nm, 27 ns) at a laser pulse energy of 0.25 J.

In appendix B all the neon measurements have been combined in one graph showing the dependence of the current in the transmitted peak (first ion peak) of the TOF spectrum on $N \times R_{TP}$, where N is the particle density of the neon background atmosphere and R_{TP} is the target-probe distance. From the slope of a fit to the data we found (by using a simple Beer's law scattering model) that the collection cross section for collisions of silver ions with the neon background gas is $\sigma_{Ne} = 4.0 \cdot 10^{-16}$ cm^2. This value is in good agreement with previous collection cross sections found for collisions of silver ions with oxygen and argon using the same setup ($\sigma_{O2} = 4.8 \cdot 10^{-16}$ cm^2 and $\sigma_{Ar} = 6.7 \cdot 10^{-16}$ cm^2) [21], and in agreement with results from other groups as well [25,28]. These experimentally determined collection cross sections confirm the assertion in section 4.1 that the lower deposition rate of ITO in argon than in oxygen can partly be explained by an increased scattering of the ablated species in argon relative to oxygen. Ap-

pendix B includes a more general discussion of the interpretation of these cross sections together with calculations of total cross sections for collision of silver ions with oxygen, neon, argon and xenon particles, and for collision of indium, tin and oxygen ions with neon atoms.

4.3.2 Time-of-flight in various gases

In order to compare ion dynamics in different background gases, Figure 4-7 presents TOF results for silver ions ablated in the three different background gases, oxygen, neon and argon, at 45 mtorr at a target-probe distance of 80 mm. The ion signals have been normalised to their maximum peak value. Note that there may be small differences in the definition of t=0 as the oxygen and argon data are not from this work.

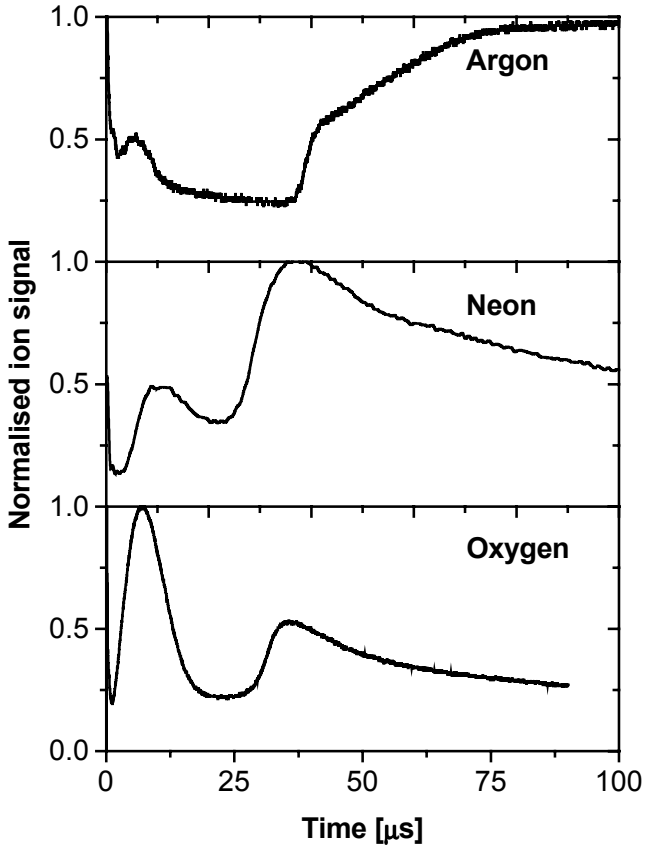

Figure 4-7 Time-of-flight spectra of silver ions ablated in oxygen, neon and argon at 45 mtorr. Target-probe distance: 80 mm. Laser fluence: 2.4 - 2.5 J/cm^2. Oxygen data are from reference [21] and argon data from reference [27].

Obviously, the three different background gases scatter the ablated silver ions differently, even though plume splitting is observed in all three gases. In oxygen, the first ion peak, representing fast ions, dominates completely, and the second ion peak is only weakly broadened. In neon, however, the first ion peak is suppressed and the second peak, which seems to be slightly more broadened than in oxygen, dominates. The same tendency is observed in argon, where significant broadening and delay of the second ion peak is noted.

The plume splitting behaviour observed in neon and argon resembles ion probe measurements presented by Wood *et al*. [28] in which silicium ions were ablated into helium. In their experiments the target-probe distance was 50 mm

and they used pressures in the range 100 – 250 mtorr. In addition, Wood *et al.* had modelled the ion flux curve shapes using a multiple-scattering/hydrodynamical model. Their experimental and model results indicated that a dominant second ion peak is expected (at pressures where plume splitting occurs) when "high-mass" ions (silicium ions) are scattered into a "low-mass" inert background gas (helium). In contrast, two clearly separated dominant peaks are expected when the ion mass (silicium ion mass) is lower than the mass of the inert scattering gas (argon). In experimental and model results for silicium ablated in argon, Wood *et al.* furthermore pointed out that the fast ion peak was not shifted away from the vacuum peak.

Apparently, the TOF curve for silver ions ablated in oxygen (Figure 4-7) represents a third possibility. Two separated ion peaks are observed; however, the first ion peak is shifted away from the vacuum peak [21]. This behaviour could be related to the fact that the amount of possibly inelastic scattering processes is much higher for ion – molecule collisions than for ion – atom collisions. As a molecule can be vibrationally and rotationally excited in an inelastic collision with and ion, the silver ions can lose energy to these excitation processes. This possibility does not exist if the background gas consists of atoms.

4.3.3 Ion energy distribution in vacuum

From the TOF spectrum measured in vacuum, see Figure 4-5, it is possible to obtain an energy distribution of the ablated silver ions, see Figure 4-8.

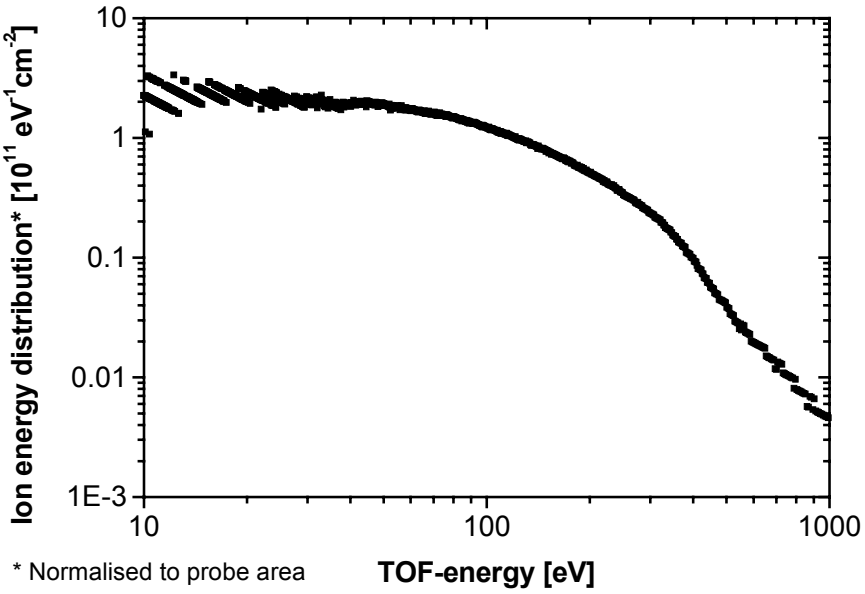

Figure 4-8 Energy distribution of silver ions ablated in vacuum. Target-probe distance: 80 mm. Laser fluence: 2.4 J/cm^2.

Assuming that the ions are singly ionised and not accelerated during their travel from target to probe, the number, N, of positively single ionised silver ions normalised to the probe area, S, and with an energy between E and $E+dE$ is given as [29]:

$$(1/S)\, N(E) = (e\, m\, R_{TP}\, S)^{-1} \cdot t^3 \cdot I\,. \qquad (4\text{-}2)$$

Here e is the elementary charge, m the ion mass and I the ion current at time t. It is noted that $R_{TP} >> r_0$, where r_0 is the radius of the laser beam spot on the target.

Figure 4-8 shows the vacuum energy distribution based on equation (4-2). The distribution is broad containing ions with energies from a few eV to several hundred eV, as expected from the discussion in section 2.2. When the ablation is performed in a background gas, this energy distribution will be altered considerably. However, as indicated above, some of the high-energy ions (fast ions) will probably reach the probe (or a substrate) without being scattered. High-energetic ions impinging on a substrate during film deposition are not necessarily beneficial to film growth as they may create defects in the film or even cause resputtering, although reemission effects may account for 3% loss of the total deposited material at most [11].

4.4 Summary

The experiments presented in this chapter clearly demonstrate that the ITO deposition rate during deposition strongly depends on the experimental parameters; the type of the background gas, the background gas pressure, and the laser fluence. The highest deposition rates were obtained in oxygen, even though the experimental collection cross section for collision of silver ions with the different gases was higher for oxygen than for neon. Two effects can explain this difference between oxygen and the inert gases:

1. Gas dynamic effects. Even before deposition, the ion plume dynamics is significantly different in oxygen than in the inert gases.
2. Chemical effects. Chemical reactions between the oxygen gas and the ablated species at or near the substrate surface may influence film deposition.

In interpretation of the deposition data it seems important to note that details in the experimental settings may affect the deposition rate significantly. Furthermore, it seems important to distinguish between the thickness and the mass deposition rate as the film density may vary with substrate temperature.

4.5 References

1 G.K. Hubler in *Pulsed Laser Deposition of Thin Films*, ed. by D.B. Chrisey, G.K. Hubler (Wiley, New York 1994) pp.327-355

2 B. Thestrup, J. Schou, A. Nordskov, N.B. Larsen: Appl. Surf. Sci. **142**, 248 (1999)

3 B. Thestrup, J. Schou: accepted for publication in Appl. Phys. A

4 M. Kamei, Y. Shigesato, S. Takaki: Thin Solid Films **259**, 38 (1995)

5 H.L. Hartnagel, A.L. Dawar, A.K. Jain, C. Jagadish: *Semiconducting Transparent Thin Films* (Institute of Physics Publishing, Bristol 1995)

6 R.B.H. Tahar, T. Ban, Y. Ohya, Y. Takahashi: J. Appl. Phys. **83**, 2631 (1998)

7 S. Preuss, E. Matthias, M. Stuke: Appl. Phys. A **59**, 79 (1994)

8 J.G. Lunney, R.R. O'Neill, K. Schulmeister: Appl. Phys. Lett. **59**, 647 (1991)

9 T. Szörényi, Z. Kántor, L.D. Laude: Appl. Surf. Sci. **86**, 219 (1995)

10 C. Coutal, A. Azéma, J.-C. Roustan: Thin Solid Films **288**, 248 (1996)

11 C.N. Afonso, J. Gonzalo: Nucl. Inst. and Meth. B **116**, 404 (1996)

12 A. Gupta: J. Appl. Phys. **73**, 7877 (1993)

13 J.P. Zheng, H.S. Kwok: Thin Solid Films **232**, 99 (1993)

14 D.L. Smith: *Thin-Film Deposition: Principles and Practice* (McGraw-Hill, New York 1995)

15 E. Holmelund, B. Thestrup, J. Schou, unpublished

16 T.N. Hansen: *UV laser ablation of metals in vacuum* (Master Thesis in Danish, University of Copenhagen 1997) p. 30, 54

17 T.N. Hansen, J. Schou, unpublished

18 B. Toftman, J. Schou, unpublished

19 C.S. Ma, S.K. Hau, K.H. Wong, P.W. Chan, C.L. Choy: Appl. Phys. Lett. **69**, 2030 (1996)

20 J.A. Greer, M.D. Tabat, C. Lu: Nucl. Inst. and Meth. B **121**, 357 (1997)

21 T.N. Hansen, J. Schou, J.G. Lunney: Appl. Surf. Sci. **138-139**, 184 (1999)

22 *Handbook of Chemistry and Physics*, 79th ed. (CRS, Boca Raton 1998)

23 *Web-Elements*: www.shef.ac.uk/chemistry/web-elements

24 D.B. Geohegan in *Pulsed Laser Deposition of Thin Films*, ed. by D.B. Chrisey, G.K. Hubler (Wiley, New York 1994) pp. 115-165

25 D.B. Geohegan in *Laser Ablation: Mechanisms and Applications*, ed. by J.C. Miller, R.F. Haglund (Springer-Verlag, Berlin Heidelberg 1991) pp. 28-37

26 M. Ohkoshi, T. Yoshitake, K. Tsushima: Appl. Phys. Lett. **64**, 3340 (1994)

27 T.N. Hansen, J. Schou, unpublished

28 R.F. Wood, K.R. Chen, J.N. Leboeuf, A.A. Puretzky, D.B. Geohegan: Phys. Rev. Lett. **79**, 1571 (1997)

29 T.N. Hansen: *UV laser ablation of metals in vacuum* (Master Thesis in Danish, University of Copenhagen 1997) Appendix A.2

5 Deposition of ITO films in various background atmospheres

Thin films of indium tin oxide (ITO) are used in a variety of optoelectronic devices due to their high transparency in the visible region of the photonic spectrum combined with a high conductivity. Moreover, as mentioned in chapter 2, pulsed laser deposition (PLD) is an unique deposition technique in the sense that stoichiometric, multicomponent oxide films can be deposited on substrates even at rather low substrate temperatures without the need of post-annealing. However, the quality of the deposited films and thus film properties are, in general, sensitive to the specific process parameters during film growth.

In this chapter it is demonstrated how ITO film properties, structure and composition are related to key parameters such as type of background atmosphere, background gas pressure, and substrate temperature during the PLD process. In the first section general material properties of ITO are discussed. The second and third section demonstrate how the electrical and optical properties of ITO films are strongly related to the key deposition parameters. These two sections contain the main results within this experimental study. In the fourth section ITO film composition and surface structure are analysed. Finally, a summary of the work presented in this chapter is given in section five. A description of the film deposition setup and a list of typical deposition parameters were given in chapter 3.

5.1 Indium tin oxide

This section presents general material properties of indium tin oxide such as crystal structure, band structure, conductivity, regime of transparency, and tin-doping.

5.1.1 Crystal structure

Tin doped indium oxide, i.e. ITO, films are typically polycrystalline and retain a crystal structure of bulk undoped indium oxide (In_2O_3) [1]. However, the lattice constants are usually higher than those in bulk In_2O_3. In_2O_3 single crystal has the cubic bixebyite structure (also called c-type rare earth structure) and belongs to the space group T_h^7, Ia3. Just recently, a lattice parameter of 10.22 – 10.31 Å was found for polycrystalline ITO films deposited on glass by PLD (at temperatures between 100°-300°C) [2]. This value is in agreement with earlier measurements on sputter deposited ITO [3,4,5].

The structure of ITO is highly complicated as the unit cell of In_2O_3 and, consequently, ITO contain 80 atoms. However, two crystallographically non-equivalent indium sites exist [6]. One is associated with an equal In-O separation and O atoms lying nearly at the corners of a cube with two body-diagonally opposite corners unoccupied. The other is associated with non-equal In-O separations and O atoms lying nearly at the corners of a cube with two face-diagonally opposite corners unoccupied.

5.1.2 Band structure

Figure 5-1 shows an assumed band structure of undoped In_2O_3 and heavily Sn doped In_2O_3 proposed by Hamberg *et al.* [6]. No specific band structure calculations of ITO (or In_2O_3) have been made due to the complicated structure.

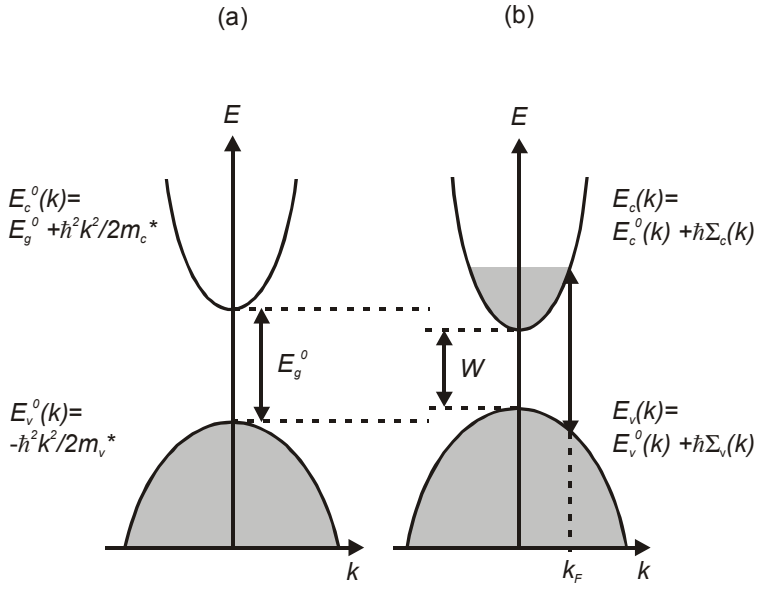

Figure 5-1 Assumed band structures of (a) undoped and (b) Sn-doped In_2O_3 [6]. Shaded areas denote occupied states. Shift of the bands is apparent. Band-gaps, Fermi wave number, k_F, and dispersion relations are also indicated.

The assumed band structure for In_2O_3 has parabolic bands characterised by effective mass m_c^* for the conduction band and m_v^* for the valence band. The direct semiconductor band-gap, E_g^0, is around 3.75 eV. The conduction band is probably mainly from In:5s electrons and the valence band is from O^{2-}:2p electrons. Usually In_2O_3 is somewhat reduced, and these oxygen vacancies, V_0, give rise to shallow donor states just below the conduction band.

ITO is an n-type semiconductor in which tin acts as a cationic dopant in the In_2O_3 lattice. Sn^{4+} ions are incorporated at In^{3+} sites and provide an extra electron for conduction, or tin ions are incorporated in interstitial positions. In undoped In_2O_3 electric conduction is due to the oxygen vacancies, V_0. Each vacancy maximally contributes two electrons for conduction (perfectly stoichiometric In_2O_3 is either an insulator or an ionic conductor [7]).

In the assumed band structure of ITO, a partial filling of the conduction band as well as shifts in the energy of the bands relative to their locations in In_2O_3 take place, as indicated in Figure 5-1. The effect of doping is a widening of the energy gap, E_g, relative to E_g^0. However, *electron – electron* and *electron – impurity* scattering (Sn atoms or oxygen vacancies being the impurities) tends to decrease the gap. This is illustrated by setting $W < E_g^0$ in the figure. Here W is the energy difference between the top of the valence band and the bottom of the conduction band in ITO. In Figure 5-1, $\hbar\Sigma_c$ and $\hbar\Sigma_v$ are self-energies due to *electron – electron* and *electron – impurity* scattering.

A schematic energy band model of Sn-doped In_2O_3 (ITO) is presented in Figure 5-2. The model has been taken from reference [8]. The tin doping results in the presence of a one-electron Sn:5s donor level just below E_c. In ITO films, V_0 and Sn:5s donor levels coexist and both contribute with conduction electrons as demonstrated in the figure. However, when the percentage of tin is high (~ 10 mol%), the contribution from oxygen vacancies is normally insignificant [1].

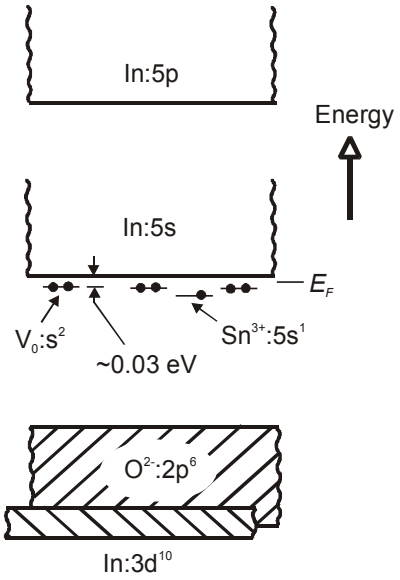

Figure 5-2 Schematic energy band model of lightly Sn-doped In_2O_3 [8]. Relevant electron levels and electron energy bands for indium, tin and oxygen are included. The Fermi energy, E_F, is indicated as well.

5.1.3 Conductivity

In general, electrical conductivity, σ, and, as a result, the resistivity, ρ, depend on the concentration, n_e, and the mobility, μ, of free carriers in a material [1,6,7]

$$\sigma = 1/\rho = n_e \mu e, \qquad (5\text{-}1)$$

where e is the electron charge. Thus, in order to obtain films with high conductivity or correspondingly low resistivity, high carrier concentrations and high mobility should be obtained at the same time.

The carrier concentration may be increased via doping as mentioned above. However, as the doping atoms occupy random sites in the host lattice, the doping process affects the carrier mobility while increasing n_e. Consequently, obtaining the lowest possible resistivity is a trade-off between carrier concentration and electron mobility. According to Tahar *et al.* [7], the theoretical maximum carrier density due to only Sn-doping is $3.0 \cdot 10^{20} \times C_{Sn}$ (at%), where C_{Sn} is the tin concentration.

In a polycrystalline semiconducting material as ITO the mobility of the charge carriers depends on the mechanisms by which the carriers are scattered by lattice imperfections [1]. Various scattering mechanisms may be involved in semiconducting materials. *Ionised impurity* scattering, *neutral impurity* scattering, and *grain-boundary* scattering are some of the scattering mechanisms that have been mentioned in connection with mobility measurements of ITO films [9,10].

Table 5-1 below gives some examples of optimum electrical material parameters obtained for ITO films deposited by other vacuum deposition methods. Silver is included as well in order to relate the parameters of the semiconductor to a well-known metal. Reviews on electrical properties of ITO films deposited by deposition techniques other than PLD are given by, e.g., Hartnagel *et al.* [1] and Tahar *et al.* [7].

Table 5-1 Electrical properties of ITO films deposited by other vacuum techniques. ρ: resistivity. n_e: carrier concentration. μ_H: Hall mobility. T_s: substrate temperature.

Deposition technique	ρ [10^{-4} Ωcm]	n_e [10^{20} cm^{-3}]	μ_H [cm^2/Vs]	T_s [°C]
Sputtering [11]	1.7–2.0	6.7-8.1	44-46	400
Evaporation [12]	1.5-10	2-6	45-70	150
CVD* [13]	1.6-1.8	9	43	350-450
Silver [14]	0.015	590	-	

* Chemical vapour deposition

5.1.4 Regime of transparency

ITO films are, in general, highly transparent for visible light and highly reflective for mid- and far-infrared radiation [1,6,10,15,16,17]. Figure 5-3 shows the typical spectral dependence of a transparent, semiconducting material [18].

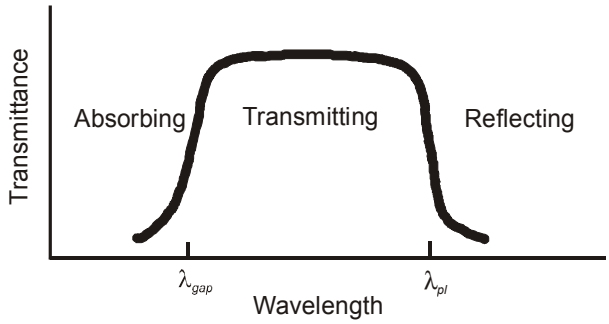

Figure 5-3 Spectral dependence of a transparent semiconducting material. λ_{gap} and λ_{pl} are the wavelengths at which the band-gap absorption and the free electron plasma absorption take place.

For UV wavelengths, absorption due to the fundamental band-gap dominates. For large wavelengths, high reflection due to free electrons is observed.

The wavelength, λ_{gap}, at which band-gap absorption takes place (see the figure), is determined by the band-gap shift in ITO relative to undoped In_2O_3, i.e. by $\Delta E_g = E_g - E_g^0$ (see also Figure 5-1). ΔE_g is given by [6]

$$\Delta E_g = \Delta E_g^{BM} + \hbar\Sigma_c(k_F) - \hbar\Sigma_v(k_F). \qquad (5\text{-}2)$$

Here ΔE_g^{BM} is a Burstein-Moss shift that is related to the carrier density, n_e, and the reduced effective mass, m_{vc}* ($(m_{vc}^*)^{-1} = (m_v^*)^{-1} + (m_c^*)^{-1}$) by

$$\Delta E_g^{BM} = (\hbar^2/2m_{vc}^*)(3\pi^2 n_e)^{2/3}. \quad (5\text{-}3)$$

The Burstein-Moss shift occurs due to blocking of the lowest conduction band states by partial filling of electrons above the Mott critical density.

The plasma wavelength, λ_{pl}, determines the transition from the transmitting to the reflecting wavelength region (see Figure 5-3). According to classical Drude theory for free electrons in metals [1,6,15,19], λ_{pl} is related to the free carrier concentration, n_e, and the mobility of charge carriers, μ

$$\lambda_{pl} \propto ((n_e e^2/\varepsilon_0 \varepsilon_\infty m_e^*) - \gamma^2)^{-1/2}. \quad (5\text{-}4)$$

Here ε_∞ is the dielectric constant of the medium[7], ε_0 the dielectric constant of free space, m_e^* the effective mass of the charge carriers, and γ a quantity (assumed to be energy-independent) that is correlated to mobility as $\gamma = e/(m_e^*\mu)$. The carrier concentration, n_e, essentially determines the plasma wavelength as γ is small.

Table 5-2 below gives some examples of optimum optical material parameters obtained for ITO films deposited by other vacuum deposition methods. Reviews on optical properties of ITO films deposited by deposition techniques other than PLD are given by, e.g., Hartnagel *et al.* [1] and Hamberg *et al.* [6].

Table 5-2 Optical properties of ITO films deposited by other vacuum techniques. T: transmission (visible region). E_g: band-gap. n: refractive index. T_s: substrate temperature.

Deposition technique	***T*** **[%]**	***E_g*** **[eV]**	***n***	***Ts*** [°C]
Sputtering [4]	68-80	3.57-3.8	1.6-2.3	60-90
Evaporation [21]	69-90	3.75-3.91	-	200-330°C
CVD [20]	90	3.9	-	-

5.1.5 Sn-doping

In this work, a standard target with an SnO_2 concentration of 10 wt% (10.9 at%) and, therefore, an In_2O_3 concentration of 90 wt% In_2O_3 was chosen. In atomic percentage this corresponds to 3.7 at% Sn, 35.6 at% In, and 60.7 at% O. This target composition is expected to give ITO films with the lowest resistivities and the highest transmission of visible light under proper experimental conditions [21,22].

A study of reactively evaporated ITO films of various tin doping demonstrated that optimum resistivities and optimum transparency were achieved for films deposited on heated substrates with a tin concentration of 10–15 wt% [21]. For tin concentrations above 15 wt%, a decrease in transparency was observed and, in general, the Hall mobility tended to decrease with increasing tin concentration. Another study on the free electron density versus Sn concentration of ITO films prepared by a pyrolytic method indicated that a maximum in free electron density occurred at an Sn concentration (relative to all metal atoms) around 9-14 at% [22], which corresponds well to the Sn concentration in our targets.

7 Extrapolated towards high energy.

5.2 Electrical film properties

This section presents results that examine how the electric resistivity of laser deposited ITO films on glass varies as a function of the type of background atmosphere, the background gas pressure, and the substrate temperature.

The resistivity, ρ, is determined from the measured sheet resistance, R_s, and the film thickness, d, of the ITO films as

$$\rho = R_s \cdot d \,. \qquad (3\text{-}7')$$

Figure 5-4 demonstrates how the sheet resistance decreases as a function of film thickness for ITO films deposited in 23 mtorr of oxygen. The films were deposited at a laser fluence around 0.5 J/cm^2 both on non-heated (25°C) and heated (200°C) glass substrates.

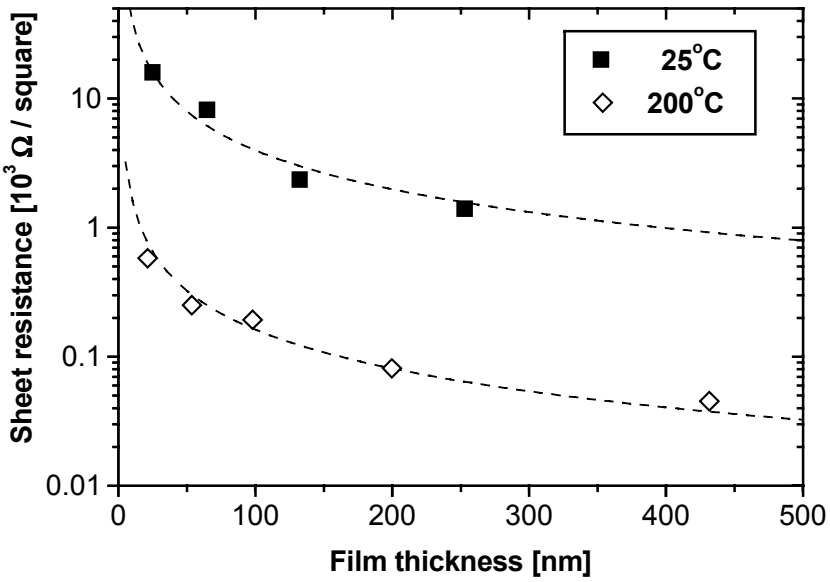

Figure 5-4 Sheet resistance versus film thickness for ITO films deposited in 23 mtorr oxygen at a laser fluence around 0.5 J/cm^2 on heated (200°C) and non-heated (25°C) glass substrates.

Curves corresponding to calculated average resistivities of ρ = 0.040 Ωcm (25°C) and ρ = 0.0016 Ωcm (200°C) are shown as well. There seems to be good agreement between the data and the curves which means that no significant film size effects are present for the deposited ITO films within the applied thickness range (25 - 450 nm). The present work includes only ITO films with thicknesses above 25 nm. Thus, in the following ρ may be taken as a general film parameter that is independent of the film thickness.

As a rule, the electric properties of indium oxide and ITO films have been found to deviate from bulk behaviour when the film thickness decreases below a critical value [1,7,11,23,24]. This value varies depending on the control parameters of the deposition process. Coutal *et al.* [23] and Shigesato *et al.* [11] deposited thin ITO films on glass by PLD (193 nm ArF laser, fluence 5-9 J/cm^2) and sputtering, respectively, and observed an increase in resistivity for thin films with thicknesses below around 100 nm. This resistivity increase was connected

to a decrease in carrier mobility. Zheng *et al.* [24] measured the resistance, *in situ*, of ITO films grown on glass (by PLD) using a 193 nm laser and a fluence of 1 J/cm^2. They also observed a decrease in resistivity with increasing film thickness for ITO films; however, in the range 2 – 35 nm. They ascribed the effect to a change from two-dimensional to three-dimensional (bulk) behaviour. When the film thickness is thinner than, or around, the mean free path of free carriers, surface scattering becomes increasingly important which affects the film conductivity [25].

In our case the size effects are apparently negligible in the applied thickness range. This may indicate that the mean free paths of the free carriers are below 25 nm for thin ITO films deposited in 23 mtorr oxygen at a fluence of 0.5 J/cm^2.

5.2.1 Background atmosphere effects / non-heated substrates

Figures 5-5 to 5-8 summarise results from an experimental study of how the electric resistivity of ITO films deposited on glass (by PLD) varies as a function of key deposition parameters. The parameters examined are the background atmosphere, the background gas pressure, p, and the substrate temperature, T_s. The four atmospheres or gases used in this study were oxygen, neon, argon and xenon. The same gases were used for the deposition rates studies in chapter 4.

Oxygen is the standard reactive gas used in deposition of multicomponent oxides. The gases, neon, argon, and xenon were chosen because they are inert and their masses resemble the masses of atomic oxygen, molecular oxygen, and tin and indium, respectively.

In the work presented in Figures 5-5 to 5-8 the laser fluence was within 0.5 to 0.8 J/cm^2. The fluence was adjusted for each background gas in order to keep the deposition rates within the same order of magnitude. Film thicknesses were within 25 to 250 nm. The film thickness was either calculated from deposition rates, measured by a quartz crystal microbalance (QCM) or measured directly with an atomic force microscope (AFM) – see subsection 3.2.1. The deposition rate, D, strongly depends on the laser pulse energy, E, and the background gas pressure, p. Therefore, a pressure-energy scaling formula was derived for each background gas. The formula was based on extensive experimental data sets on D versus E and p. It was, then, possible to calculate the film thickness from knowledge of the precise energy and pressure at which a given film was deposited. The experimental uncertainties in the determination of film thickness were discussed in section 4.2. The scattering of the data points in Figures 5-5 to 5-8 for the same pressure value indicates the reproducibility of the film resistivity.

It should be noted that the ITO film resistivity has been remeasured for the majority of the films since the work in [26]. In the published data the resistivity was measured with a preliminary resistivity setup, which turned out slightly to overestimate the resistivity. The remeasuring affected mainly films with low resistivity, below or around approximately 0.01 Ωcm. Films that had been analysed with, e.g., AFM or XPS and therefore damaged could not be remeasured. They are indicated with a star in the figures.

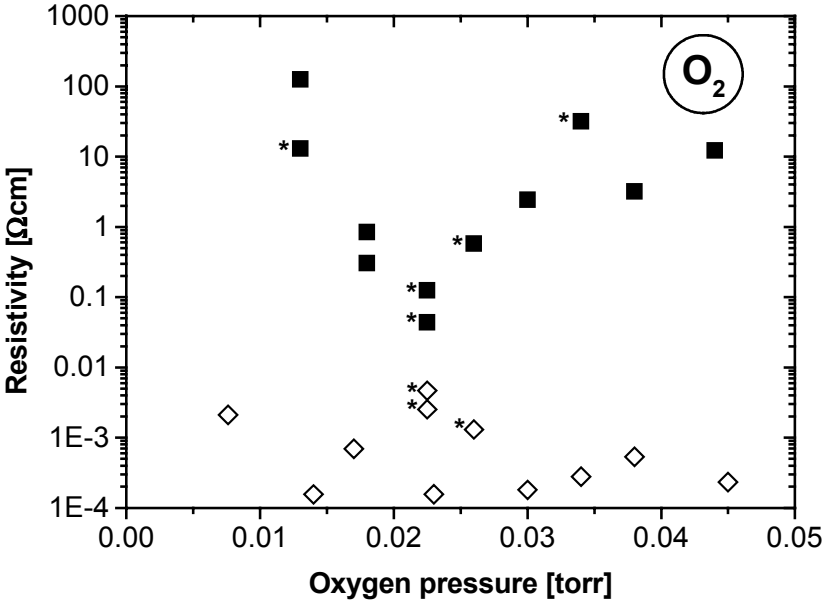

Figure 5-5 Resistivity versus oxygen pressure for ITO films deposited on glass. Solid squares: T_s = 25 °C. Open diamonds: T_s = 200 °C. ∗: Preliminary measurements – see text.

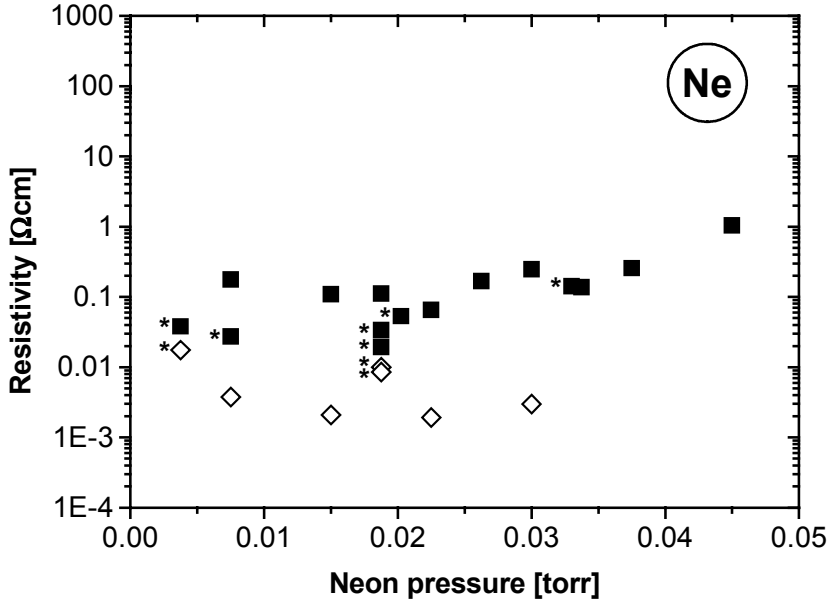

Figure 5-6 Resistivity versus neon pressure for ITO films deposited on glass. Solid squares: T_s = 25 °C. Open diamonds: T_s = 200 °C. ∗: Preliminary measurements.

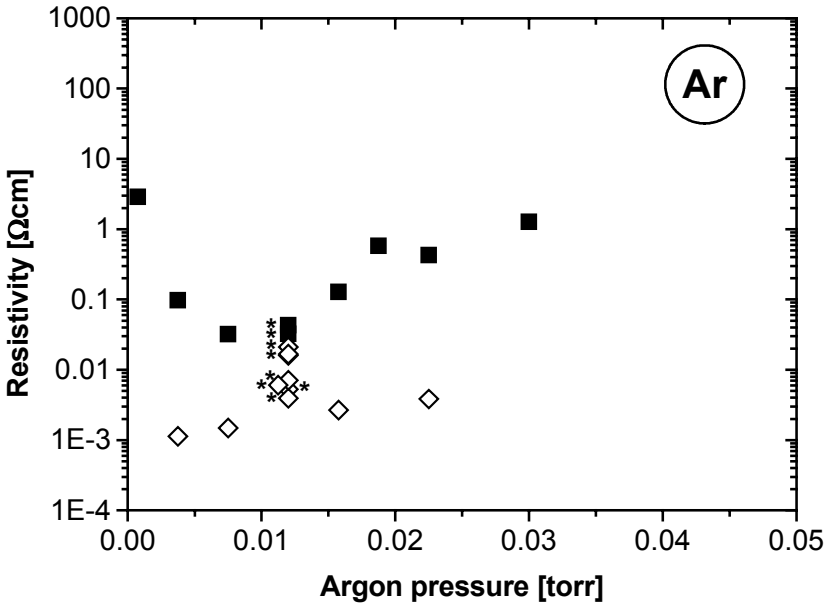

*Figure 5-7 Resistivity versus argon pressure for ITO films deposited on glass. Solid squares: T_s = 25°C. Open diamonds: T_s = 200°C. *: Preliminary measurements.*

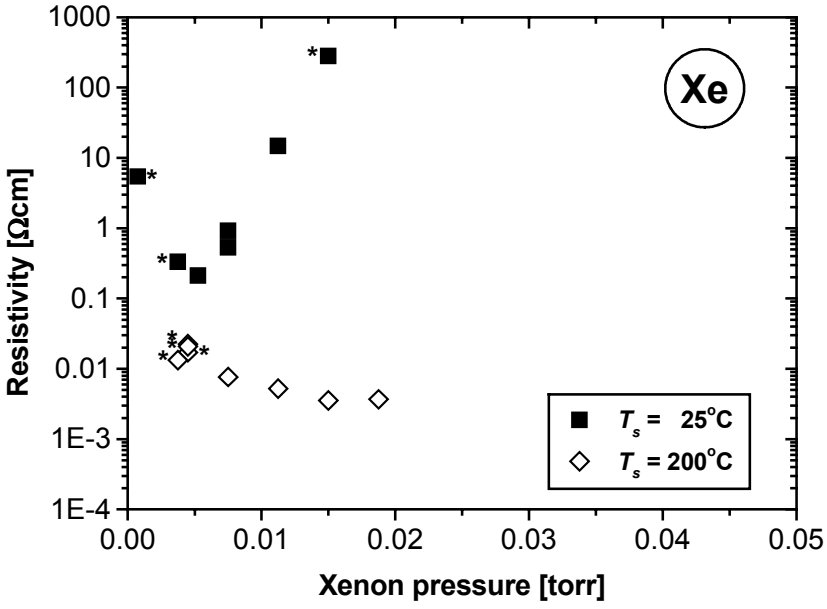

*Figure 5-8 Resistivity versus xenon pressure for ITO films deposited on glass. Solid squares: T_s = 25°C. Open diamonds: T_s = 200°C. *: Preliminary measurements.*

This subsection deals exclusively with the resistivity measurements on ITO films deposited on non-heated glass substrates (T_s = 25°C). Therefore, focus is on the solid squares (+) in Figures 5-5 to 5-8.

The following characteristics are noted in the figures:

- The film resistivity, ρ, varies significantly with background gas pressure for ITO films deposited in oxygen, argon, and xenon.
- The resistivity has a minimum, ρ_{min}, at a specific pressure for ITO films deposited in oxygen, argon, and xenon.
- No significant resistivity minimum is observed for ITO films deposited in neon.
- The lowest resistivity obtained is within the same order of magnitude for ITO films deposited in oxygen, neon, and argon. However, in xenon the lowest measured resistivity is significantly higher.

These characteristics are discussed in detail below.

- Resistivity versus background gas pressure

Focusing, e.g., on the ITO films deposited in the oxygen background gas, Figure 5-5 shows how ρ varies strongly with the oxygen pressure. In fact, ρ decreases with around three orders of magnitude from ρ = 125 (±63) Ωcm at 13 mtorr to ρ = 0.043 (±0.013) Ωcm at 23 mtorr[8]. Then ρ increases again to ρ = 12 (± 4) Ωcm at 44 mtorr. Similar resistivity behaviour is observed for the ITO films deposited in argon and xenon.

Such a strong resistivity dependence on the partial pressure for laser deposited ITO films grown on non-heated substrates has also been observed by Zheng and Kwok [24], and just recently by other groups [2,27,28]. However, their studies included only ITO films deposited in oxygen. The groups observed essentially the same resistivity behaviour as in Figure 5-5, i.e. that ρ went through a minimum at a specific oxygen pressure. In Figure 5-5 the resistivity minimum is obtained at an oxygen pressure of 23 mtorr. This pressure is slightly higher than what has been obtained by the other groups. However, their experimental settings and setup geometries were also slightly different. In the summary section, our resistivity results are compared further with work by other groups.

Zheng and Kwok [24] proposed an explanation of the resistivity behaviour versus oxygen pressure. They claimed that the oxygen gas acted as a velocity moderator during film deposition. Apparently, at the optimum oxygen pressure, energetic ions and atoms with a uniform velocity distribution of various species should combine to produce good-quality films. If the oxygen pressure was too low, the density of the various constituents would not be uniform on the surface of the substrate. If, on the other hand, the oxygen pressure was too high, the particles arriving at the substrate surface would have lost so much energy that their surface mobility on the substrate would be reduced considerably. This would then lead to poorer film quality.

In the present study it is expected that this explanation, to some extent, may explain the resistivity behaviour observed. However, at low pressures the defect production on the growing film by energetic ions is expected to be important for the resistivity as well. The resistivity behaviour is discussed further below.

8 The resistivity uncertainty given in the brackets is based on the uncertainty in film thickness.

■ Resistivity minimum versus background gas

From Figures 5-5, 5-7 and 5-8 it is seen that the resistivity has a minimum, ρ_{min}, at a specific optimum background gas pressure in oxygen, argon and xenon. This optimum pressure is around 23 mtorr in oxygen, around 10 mtorr in argon, and around 5 mtorr in xenon. Thus, the optimum pressure depends on the specific ambient gas used. Such behaviour is not surprising and may be explained by simple considerations.

In our PLD experiments, the collision cross section is expected to be significantly higher for ion/neutral-argon collisions than for ion/neutral-oxygen collisions. The assumption is based on collection cross sections given in section 4.3, where the collection cross section for collisions of silver ions with argon atoms ($\sigma_{Ar} = 6.7 \cdot 10^{-6}$ cm^2) was considerably larger than the collection cross section for collisions of silver ions with oxygen molecules ($\sigma_{O2} = 4.8 \cdot 10^{-6}$ cm^2). Assuming that the ions (and/or atoms) in the plasma plume need a certain number of scattering events to achieve optimum deposition conditions, this is obtained at a lower pressure in argon than in oxygen.

The fact that ρ_{min} was observed at even lower pressure in xenon than in the other two gases can be explained as xenon being a more effective scatterer having a higher mass as well as larger collision diameter than oxygen and argon.

Focusing on ITO films deposited in oxygen, XPS measurements indicate that the minimum in ρ could be connected with an enhanced carrier concentration. The XPS measurements (see section 5-4) on selected ITO films indicated an enhanced Sn to In concentration for ITO films deposited near the optimum pressure, i.e. an enhanced carrier concentration, n_e. This result is in agreement with results from Adurodija *et al.* [27] who observed a maximum in both carrier concentration, n_e, and Hall mobility, μ_H, for ITO films deposited at the optimum oxygen pressure. Kim *et al.* [2] explained the increase in ρ (from ρ_{min}) with increasing pressure as a decrease in the number of oxygen vacancies. However, our XPS measurements indicate that the relative oxygen content in the ITO films is slightly above the stoichiometric value for all three films examined, which does not support their explanation.

■ Resistivity for ITO films deposited in neon

No significant resistivity minimum is observed for ITO films deposited in neon (Figure 5-6). However, neon also represents a special case with regard to plume dynamics during ITO deposition.

In a simplified model, one may assume that an essential condition for obtaining good quality ITO films (at T_s = 25°C) is that the majority of the ablated In, Sn, and O particles arrive at the substrate at equal time. Subsequently, if time-of-flight (TOF) spectra of the different In, Sn, and O ions were measured at the substrate position, these spectra should, to some extent, overlap. The In and Sn particles have significantly higher masses than the O particles. Therefore, one may further assume that the background gas acts most strongly on the ablated O ions (or atoms) in the plasma plume.

With reference to section 4.3 there seems to be a significant difference in the way oxygen and neon may affect the TOF spectra of ablated particles (measured at the substrate position). An oxygen background gas is expected to produce two-component TOF distributions in which the main component is rather narrow. Thus, if the In, Sn, and O TOF spectra must overlap at the substrate to obtain a good ITO film, this is probably achieved only at a specific oxygen pressure (or pressure range). In contrast, a neon background gas is expected to produce more broad TOF distributions that are significantly delayed relative to the distributions in vacuum. This serves two purposes. The pressure range, where

the In, Sn, and O TOF spectra will overlap may be broader and, furthermore, fast ions are suppressed which otherwise might have damaged the growing film.

Figure 4-7 in the previous chapter showed TOF spectra of silver ions ablated in oxygen and neon. Here the first (narrow) ion peak was dominant for silver ions ablated in oxygen, whereas the second (broader) ion peak was dominant for silver ions ablated in neon.

Argon is believed to produce broad TOF distributions for the ablated particles and suppress fast ions as well (see Figure 4-7). However, only if the ion mass is higher than the argon mass [29], which is not the case for oxygen ions. Assuming, argon mainly serves as a scatterer for the fast oxygen ions, the pressure range where the In, Sn, and O TOF spectra overlap may be very narrow in argon as well.

As a comment it should be noted that Wu *et al.* [28] recently produced conducting films by laser ablation from an ITO target in vacuum. However, in contrast to this work, they had a target-substrate distance of only 34.5 mm and they used a KrF eximer laser (248 nm) operating at 2 J/cm^2. The difference in arrival time (at the substrate) for the ablated In, Sn, and O particles is expected to decrease with decreasing target-substrate distance (assuming that the particles have equal initial energies). Moreover, an increased fluence increases the deposition rate, which may improve film conductivity as well. This fact is demonstrated in the following chapter.

With reference to the simplified model given above, it is assumed that not only the presence of a background gas but also how this gas scatters the ablated particles was important for the quality of the ITO films presented in Figures 5-5 to 5-8. Especially fast ions with energies around 100 eV (see, e.g., Figure 4-8) could produce defects in the growing film which seems to be important at low background pressures.

■ Resistivity minimum in xenon

In Figures 5-5 to 5-8 it is observed that ρ_{min} is around 0.02 to 0.04 Ωcm for films deposited in oxygen, neon and argon, whereas ρ_{min} ~ 0.2 Ωcm in xenon, i.e. one order of magnitude higher.

The higher ρ_{min} value in xenon than in the other gases indicates that optimum film deposition conditions are difficult to obtain in xenon.

An interesting point, in this context, is that xenon is a high-mass background gas in which O, Sn, and In ions (and atoms) of lower mass are scattered. Referring to the discussion in subsection 4.3.2 and the neon discussion above, xenon is then expected to produce two-component TOF distributions for the In, Sn, and O particles (measured at the substrate position). Furthermore, the main components of these TOF distributions are expected to be narrow with relative high average velocities (i.e. comparable with the velocities obtained in vacuum). Thus, fast ions may indeed damage the film, possibly even at the "optimum" pressure.

It should be noted that damage of the growing film by fast ions seems to be less important at higher deposition rates (or higher substrate temperatures), at least for deposition in oxygen – see chapter 6.

5.2.2 Substrate temperature effects / heated substrates

This subsection deals with the resistivity measurements on ITO films deposited on heated glass substrates (T_s = 200°C). Therefore, focus is on the open diamonds (◊) in Figures 5-5 to 5-8.

Obviously, increasing the substrate temperature during ITO film deposition affects the resistivity significantly. The following characteristics are noted in the figures:

- ◊ In general, the resistivity, ρ, of the ITO films is lower for films deposited on heated substrates than on non-heated substrates.
- ◊ The resistivities of the ITO films grown at T_s = 200°C are relatively independent of the partial pressure within the applied pressure range.
- ◊ The lowest resistivities are obtained for ITO films deposited in oxygen.

These characteristics are discussed below.

◊ Resistivity versus substrate temperature

In Figures 5-5 to 5-8 the lowest measured resistivity values for films deposited at 200°C are between ρ = 0.00016 ($\pm 4.8 \cdot 10^{-5}$) Ωcm in oxygen and ρ = 0.0035 ($\pm 1.1 \cdot 10^{-3}$) Ωcm in xenon. Thus, a decrease in ρ with around two orders of magnitude was obtained for the ITO films by raising the substrate temperature.

According to section 2.3, an increase in substrate temperature will, e.g., increase the rate of surface diffusion of the adsorbed particles on the surface of the growing ITO film and improve the film quality substantially. In fact, the ITO films deposited at T_s = 200°C are measured to be polycrystalline, whereas the ITO films deposited at T_s = 25°C are amorphous – see chapter 6. Such an improvement in crystallinity of ITO films deposited on heated substrates may reduce carrier scattering and, as a result, increase the carrier mobility as mentioned in subsection 5.1.3.

Recently, Adurodija *et al.* [27] measured the Hall mobility, μ_H, and the carrier density, n_e, of laser deposited ITO films deposited at room temperature and T_s = 200°C, respectively. They also observed a decrease in ρ at T_s = 200°C relative to room temperature that was a direct result of a significant increase in μ_H and a more moderate increase in n_e.

◊ Resistivity versus background gas pressure

The resistivity of ITO films grown at T_s = 200°C is relatively independent of the partial pressure within the applied pressure range (Figures 5-5 to 5-8). This tendency is in accordance with measurements from other groups for deposition in oxygen [2,27,30] even though they observed a slight increase in ρ at the highest pressures. However, their experimental settings as well as setup geometries were slightly different from ours.

The flat resistivity curves, seen in the figures, reflect the high diffusion rate of the ablated particles on the film surface during ITO film growth. At elevated substrate temperatures, the ablated particles can migrate on the surface and improve the local crystallinity even though they may arrive at the film surface at different times.

◊ Resistivity for ITO films deposited in oxygen

Figure 5-9 shows resistivity measurements for ITO films deposited in an oxygen gas at three different substrate temperatures, 25°C, 200°C, and 300°C, respectively. The laser fluence was around 0.5 J/cm^2.

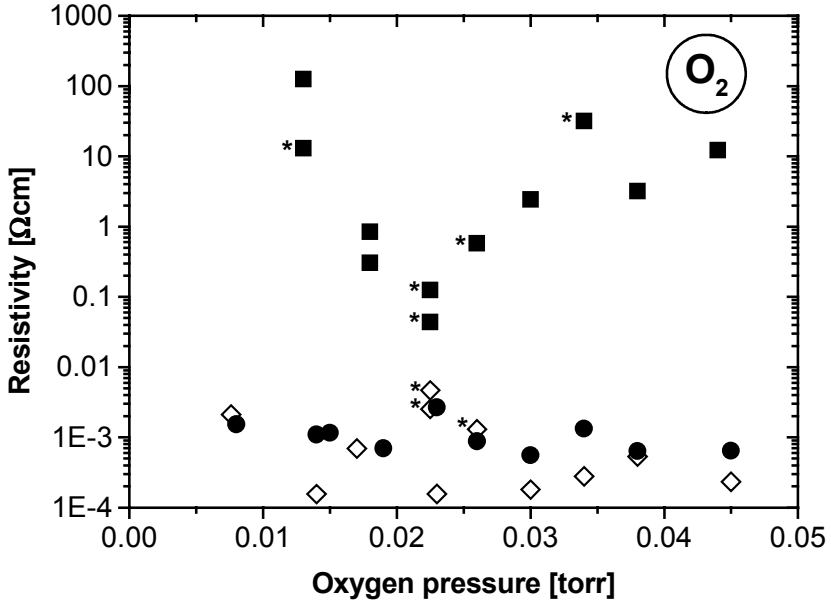

*Figure 5-9 Resistivity versus oxygen pressure for ITO films deposited on glass. Solid squares: T_s = 25°C. Open diamonds: 200°C. Solid circles: T_s = 300°C. *: Preliminary measurements. The scattering of the data points for the same oxygen pressure and substrate temperature indicates the reproducibility.*

No improvement in the resistivity was found when the substrate temperature was increased from T_s = 200°C to T_s = 300°C. This is somewhat surprising. Other authors measured an improvement in ρ at the optimum oxygen pressure when the glass substrate temperature was increased to around 300°C [2,30].

Compared with resistivity data for T_s = 200°C, less scattering in the resistivity data for T_s = 300°C is observed in the figure, possibly indicating a more stable film deposition at this temperature.

When Figures 5-5 to 5-9 are compared, it is clear, that the lowest resistivities are obtained for ITO films deposited in oxygen on heated substrates. The reason for this is that oxygen is a reactive gas and, therefore, chemical effects become important at film deposition in oxygen. Several possible chemical mechanisms may occur which ease the incorporation of oxygen into the growing film. Some of the mechanisms are as follows.

1. Reactions in the gas phase between species emitted from the target and ambient oxygen during a plasma pulse.

As mentioned in section 4.1, gas phase dissociation of molecular oxygen into atomic oxygen is not expected to be of significant importance for deposition due to the high bond dissociation energy of molecular oxygen (5.11 eV). Nevertheless, some dissociation of O_2 is expected to take place initiated by, e.g., collisions between O_2 and high-energy electrons in the plasma. Another possible reaction is that the background gas reacts with the energetic species in the plasma plume and creates metal-oxide complexes. These complexes may then dissociate and provide reactive oxygen atoms. This hypothesis is supported by recent measurements in which InO and SnO complexes were identified by TOF

mass spectrometry following ablation of an In-Sn alloy with an Nd:YAG laser (532 nm, 7ns). The ablation was performed in a background atmosphere consisting of 375 mtorr of oxygen (30%) and helium (70%) [31].

2. Reactions at the film surface between the ambient oxygen and other adsorbed particles during and/or in between plasma pulses.

Roman *et al.* [32] have studied the origin of oxygen in laser deposited (266 nm, 0.4–2.1 J/cm^2) BiSrCaCuO films. Their films were deposited in an oxygen atmosphere (8 to 375 mtorr) on MgO substrates heated to 700°C. They claimed that approximately 45% of the oxygen in their films was incorporated from the ambient gas during the laser pulse, and that no oxygen incorporation happened between laser pulses. They proposed that the main mechanism of oxygen incorporation corresponded to the dissociation of molecular oxygen (by bombardment of energetic species) adsorbed at the surface, leading to the formation of very reactive atomic oxygen that was further injected into the films. In contrast, Zheng and Kwok [24] claimed that, in their laser deposited ITO films deposited at room temperature on glass, the oxygen content was mainly contributed by the oxygen coming from the target itself.

3. Reactions at or near the surface of the target between the ambient and the dense plasma (or the laser light).

Roman *et al.* further claimed that around 10% of the oxygen in their BiSrCaCuO films originated from oxygen incorporated in the target from the ambient gas during the laser irradiation. Another possible mechanism, which may happen close to the target region where the laser fluence is highest, is dissociation of molecular oxygen by multiphoton processes. However, O_2 has a very weak absorption at UV wavelengths [33] above 200 nm.

5.3 Optical film properties

This section presents results that illustrate how the light transmission of laser deposited ITO films varies with respect to the type of the background atmosphere, the background gas pressure and the substrate temperature. Light transmission in the range from 200 to 900 nm was measured with a spectrophotometer (see subsection 3.2.3).

5.3.1 Background atmosphere effects / non-heated substrates

Figure 5-10 shows the average transmission, T_{av}, for visible light (integral value in the range 450 - 750 nm) for the ITO films deposited at T_s = 25°C at various gas pressures in oxygen, neon, argon and xenon. The ITO films examined belong to the same group of films presented in Figures 5-5 to 5-8. The film thickness is between 25 and 250 nm. No significant effect on film thickness was observed in the film transmission in accordance with previous results on sprayed ITO films [34].

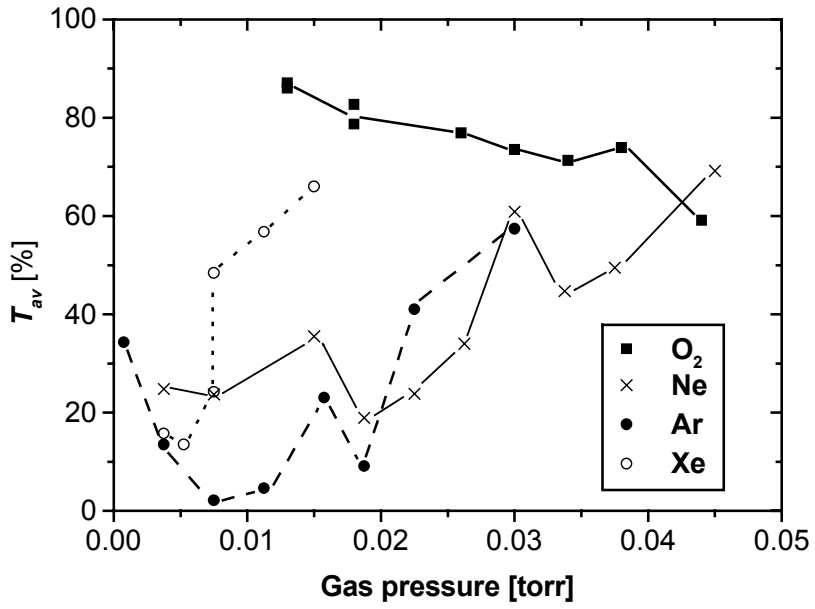

Figure 5-10 Average transmission, T_{av}, versus gas pressure for ITO films deposited at 25°C in various background gases.

Obviously, the optical transmission of the films strongly depends on the type of background gas used during film deposition.

In general, the average transmission was high for ITO films deposited in oxygen. T_{av} was between 60 - 87% and decreased weakly with increasing oxygen pressure during film deposition. Such high transmission of visible light for laser deposited ITO film in oxygen at room temperature is in good agreement with recent observations by other groups [2,27,28]. XPS measurements (see subsection 5.4.1) indicate that the variation in T_{av} with oxygen pressure in our case

may be connected with small variations in film stoichiometry. It seems as if the higher the transmission for ITO films deposited in oxygen at T_s = 25°C, the higher the relative oxygen content. This trend is supported by recent observations by Wu *et al.* [28] who have measured the transmission (at 400, 550 and 700 nm, respectively) as well as the oxygen to indium+tin ratio of a series of ITO films deposited in oxygen at room temperature. In their case high transmission corresponded to high oxygen to indium+tin ratios (i.e. above the expectation value).

The average transmission varied strongly with the gas pressure during deposition for ITO film deposited in the inert gases, neon, argon and xenon. T_{av} was between 2 - 69% and, as a rule, below the values obtained for films deposited in oxygen. Comparing Figure 5-10 with Figures 5-6 to 5-8, it is noted how the transmission data seem to follow the resistivity data. Apparently, low transmission is connected with low resistivity. The majority of the films had a metallic look and according to XPS measurements the metal content was relatively high (i.e. above the expectation value). Thus, the reduced transmission for ITO films deposited in the inert gases may be due to, e.g., increased absorption by defects and oxygen vacancies.

A list of possible defects at high Sn concentration was proposed by, e.g., Frank and Köstlin [35]. Possible defects are: SnO-like inclusions (such as an ionizable ($Sn_2^{\cdot}O_i^{\prime\prime}$) complex involving an interstitial O atom loosely bound to two Sn atoms), a non-ionisable $(Sn_2O_4)^{\times}$ complex (composed of two nearby Sn atoms which strongly bind the three closest O atoms together with an additional O atom), and an $(Sn_2^{\cdot}O_i^{\prime\prime})(Sn_2O_4)^{\times}$ associate.

5.3.2 Substrate temperature effects / heated substrates

This subsection is divided into three parts. Transmission spectra for ITO films deposited in oxygen are presented in the first part. In the second part, ITO band-gaps are estimated from these transmission spectra. The third part deals with transmission spectra for ITO films deposited in various gases. The wavelength range measured in the spectra corresponds to the left part of Figure 5-3. The plasma wavelength is beyond this range. Typical plasma wavelengths for ITO films are between 1 and 3 μm [1,6,16,36].

Transmission spectra for ITO films deposited in oxygen

Figure 5-11 shows the film transmission for three ITO films deposited in 26 mtorr oxygen at various substrate temperatures. The corresponding resistivities are shown in Figure 5-9.

The average transmission, T_{av}, for the films presented in Figure 5-11 was 77% (T_s = 25°C), 88% (T_s = 200°C), and 85% (T_s = 300°C). Thus, heating up the substrate increased the average transmission with around 10% for ITO films deposited in 26 mtorr oxygen at a laser fluence around 0.5 J/cm^2. In this particular case the increase in T_{av} for films deposited on heated substrates is probably due to the improvement in film quality. XPS measurements, of two ITO films presented in the figure, indicated that film composition was closer to stoichiometry at T_s = 200°C than at T_s = 25°C. An increase in average transmission with increasing substrate temperature has also been observed for laser deposited ITO films by other authors [2,37].

Increasing the substrate temperature also seems to shift the absorption edge of the ITO films towards lower wavelengths. This shift is probably connected to a shift in the band-gap of ITO.

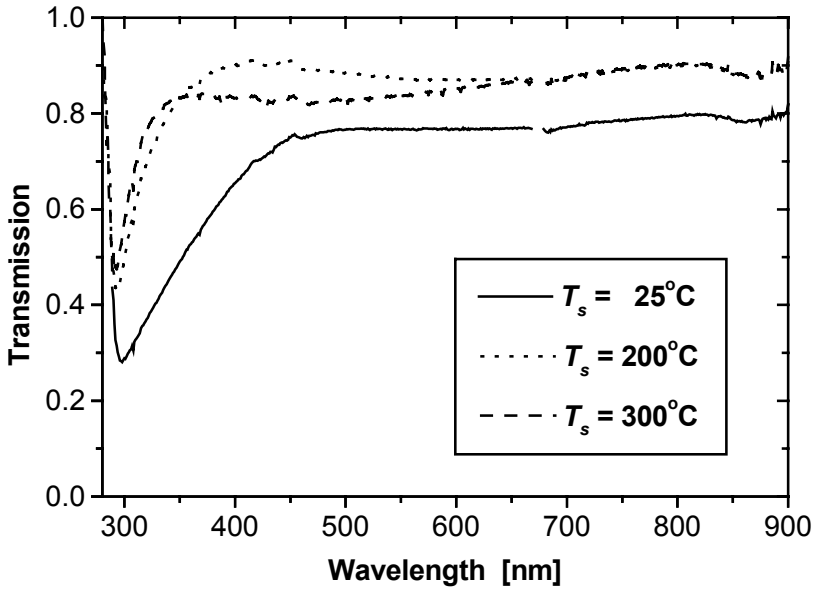

Figure 5-11 Transmission of ITO films deposited in 26 mtorr oxygen at various substrate temperatures, T_s. The film thickness was 88 (± 26) nm at T_s = 300°C, 115 (± 35) nm at T_s = 25° and 115 (± 35) nm at T_s = 200°C.

Estimation of ITO band-gaps

The direct band-gap, E_g, of the ITO films may roughly be estimated by plotting the square of the absorption coefficient, α^2, versus photon energy, $h\nu$, and extrapolating the linear region of the plot toward low energies [1,6,38]. This method is approximate for allowed direct electronic band-to-band transitions in semiconductors assuming that the refractive index, n, is constant in the energy range considered [1]. For heavily doped semiconductors as ITO, this simple method is in fact not valid since the lowest states in the conduction band are blocked, and transitions can take place only to energies above the Fermi energy [6] – see Figure 5-1. Thus, the calculated band-gaps may be taken only as a rough estimate.

Ignoring the reflectivity, which is expected to be low (between 5 and 15% on average [6,37]), α may be determined from the film transmission, T, as

$$\alpha \approx (1/d) \cdot \ln(1/T) \,. \qquad (5\text{-}5)$$

Here, d is the film thickness.

The direct band-gaps for the three ITO films in Figure 5-11 have been estimated to $E_g \approx 3.43$ eV (25°C), $E_g \approx 3.95$ eV (200°C), and $E_g \approx 4.03$ eV (300°C), respectively.

The band-gap value for the ITO film deposited at T_s = 25°C is unreasonable as E_{g0} for undoped In_2O_3 is expected to be around 3.75 eV (subsection 5.1.2). Therefore, it is possible that in this amorphous film, defect levels disturb the band-gap.

Obviously, the band-gap value seems to increase above the undoped value, E_{g0}, when the substrate is heated during ITO deposition. According to equation (5-2) such a band-gap shift may be connected with a Burstein-Moss shift. Recently, Kim *et al.* [2] also estimated band-gaps for ITO films deposited in oxy-

gen by PLD on glass substrates of various substrate temperatures. In accordance with our results, they also observed an increase in E_g with increasing substrate temperature. In their case, the increase in E_g was directly connected with an increase in carrier concentration, n_e.

Transmission spectra for ITO films deposited in various gases

Figures 5-12 compare the transmission of ITO films deposited in oxygen, neon, argon and xenon at T_s = 25°C with films deposited at similar conditions at T_s = 200°C [26]. The film thickness is between 90 and 147 nm. For comparison, films deposited in or near the optimum pressure range were chosen (see subsection 5.2.1), i.e. 26 mtorr in oxygen, 7.5 mtorr in neon and argon, and 3.8 mtorr in xenon.

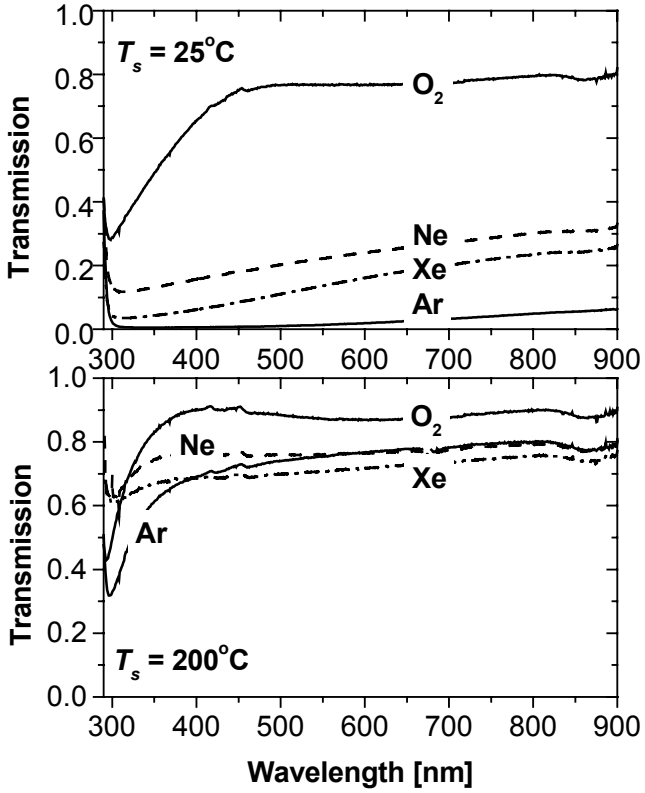

Figure 5-12 Transmission versus wavelength for ITO films deposited at substrate temperatures of T_s = 25°C and T_s = 200°C in various background gases.

The transmission spectra demonstrate that the transmission is poor for ITO films deposited in the inert gases at T_s = 25°C, as expected. The significantly low transmission for the film deposited in argon (T_{av} = 2%) reflects the corresponding relatively low resistivity obtained for this particular film ($\rho \approx 0.031$ Ωcm). As discussed in the previous subsection, low resistivity seems to be connected with low transmission for films deposited in the inert gases on non-heated substrates.

However, significant improvement in the film transmission is observed for the films deposited in the inert gases at T_s = 200°C. T_{av} is 77%, 76%, and 72% for the film deposited in neon, argon, and xenon, respectively. Thus, in the case of argon, the average transmission has been increased with 75% simply by heating

the substrate to 200°C during film deposition. An increase in substrate temperature (in PLD) is expected to improve the local crystallinity of the deposited films and, thereby, reduce the amount of defects which may act as absorption centres.

An interesting point is the contribution from chemical effects on the film transmission, i.e. the difference in transmission between films deposited in the inert gases and films deposited in reactive oxygen.

For ITO films deposited by PLD at 355 nm and a laser fluence of 0.5 – 0.8 J/cm^2, the chemical effect is only around 10 to 16% in the case of film transparency. In comparison, the chemical effect from the oxygen background gas on resistivity was around one order of magnitude (see Figures 5-5 to 5-8). An important difference between ITO films deposited in oxygen and in inert gases (at T_s = 200°C) is that the films deposited in the inert gases seemed to be oxygen deficient. This will be discussed further in the next section. Thus, one may conclude that the optical properties (of ITO films deposited at T_s = 200°C) are less sensitive to film stoichiometry than the electrical properties.

The background gas pressure effect on film transmission for ITO films deposited at T_s = 200°C in oxygen, neon, argon, and xenon was studied as well. However, in general, the average transmission was high (between 72% - 92%, except for a single film deposited in argon with T_{av} = 60%) and no significant pressure effect was observed. All the films deposited in oxygen had a high ave-rage transmission between 79% - 90%.

5.4 Film composition and surface structure

Some of the ITO films treated in the previous sections were examined by X-ray photospectroscopy (XPS) and atomic force microscopy (AFM) in order to study film composition and surface structure (see subsection 3.2.4). For comparison, a few targets were studied with XPS as well. In this section the experimental results are presented and analysed.

5.4.1 Film composition

In the XPS analysis, the relative content of carbon (C 1s), oxygen (O 1s), indium (In $3d^5/_2$) and tin (Sn $3d^5/_2$) in the film and target surfaces was measured. Here the numbers in the brackets correspond to the photo peaks examined. In general, no pretreatment of the films was performed so that a carbon peak was observed for all films. However, the carbon existed only in the upper surface layer of the films. This was confirmed by analysing some of the films after five minutes of sputtering with keV argon-ions[9] (reference [39,40,41] were used to calculate the erosion rate).

Figure 5-13 presents XPS results for selected ITO films deposited in oxygen. The figure shows the concentration of oxygen atoms relative to the total concentration of oxygen, indium and tin (O/OSnIn) as well as the concentration of tin atoms relative to indium atoms (Sn/In).

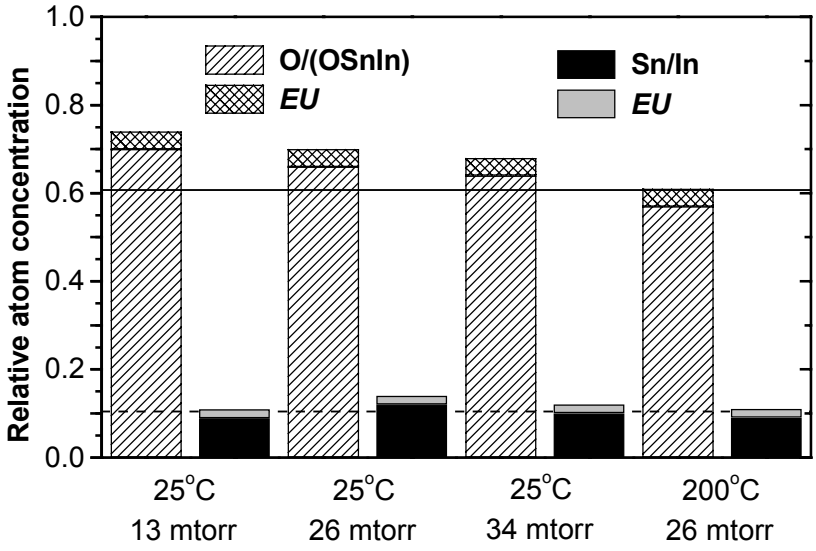

Figure 5-13 Relative atom concentrations of oxygen and tin at the surface of selected ITO films deposited in oxygen at various substrate temperatures. EU: experimental uncertainty. No sputtering cleaning performed.

9 The erosion rate was around 1 nm/min (calculated from specifications in the manufacturer's manual using measured sputtering yields for sputtering of ceramic powders and other metal oxides with keV Ar-ions).

As mentioned in subsection 5.1.5, relative atom concentrations of O/OSnIn ≈ 0.61 and Sn/In ≈ 0.10 correspond to a stoichiometric ITO film. These values are indicated with lines in the figure. The experimental uncertainties (*EU*) indicated in the figure have been determined from two independent XPS-measurements on a single film at different spots on the film surface.

Our XPS results of ITO films deposited in oxygen at 25°C indicate that the relative oxygen content in the films is slightly above the stoichiometric value. This result is in good agreement with observations by Wu *et al.* [28] who also observed a relative excess of oxygen in their ITO films deposited at room temperature using Rutherford backscattering.

Concerning the ITO film deposited in oxygen at T_s = 200°C, it seems as if the film composition is very close to stoichiometry. This corresponds well to the relatively low resistivity value of 0.0013 Ωcm for this film.

In Figure 5-14 XPS results for selected ITO films, deposited in the inert gases at T_s = 25°C and T_s = 200°C, are presented. The figure shows the relative oxygen atom concentration of the surface of the films. The stoichiometric concentration is indicated with a line. The films were deposited at pressures of 3.8 mtorr in neon and xenon, and 11 mtorr in argon, respectively.

As a rule, care must be taken in the interpretation of the results. Analysis of sputtered films indicated possible enrichment of oxygen at the film surfaces of these films. Compared with the "bulk" value the possible oxygen enrichment was 10-13%[10]. However, some of the oxygen enrichment may be due to preferential sputtering.

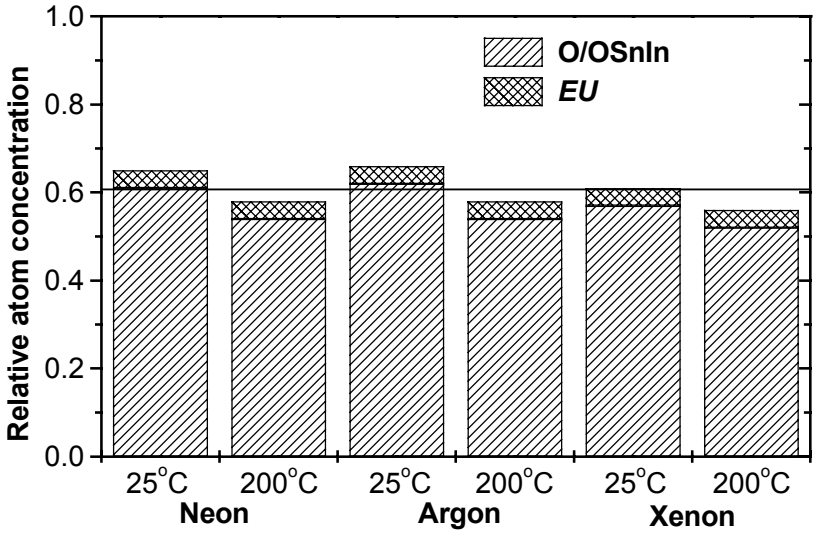

Figure 5-14 Relative atom concentrations of oxygen at the surface of selected ITO films deposited in inert gases at various substrate temperatures. EU: experimental uncertainties. No sputtering cleaning performed.

10 The analysis indicated enrichment of tin at the surface of these films as well.

In general, the oxygen concentration of the ITO films analysed is at or below the stoichiometric value, which indicates a relatively high metal concentration in these films. Furthermore, considering the possible oxygen enrichment (not indicated in the figure) at the surface of these films, the oxygen concentration in the bulk may be even lower.

The oxygen concentration seems lowest for ITO films deposited at T_s = 200°C. Thus, even though these films are expected to have an improved crystallinity, the film composition is nevertheless far from stoichiometry. Especially the ITO film deposited in xenon seems to be significantly oxygen deficient.

Three different ITO targets were examined by XPS as well. As a rule, the ITO targets were enriched with tin on the surface. The Sn/In ratio was two to four times higher than expected from the specifications. However, after sputtering the target surfaces with Ar ions, this ratio approached the stoichiometric value. Apparently, the relative oxygen content varied from target to target. In general, the oxygen content was below the stoichiometric value in the bulk of the targets.

5.4.2 Surface structure

Table 5-3 summarises the dominant surface structure and film firmness for selected ITO films examined by AFM. The films were deposited at a laser fluence of 0.5 – 0.8 J/cm^2 in the four different background gases at T_s = 25°C and T_s = 200°C.

Table 5-3 Dominating surface structure and film firmness.

Background gas	***Surface and firmness*** T_s **= 25°C**	***Surface and firmness*** T_s **= 200°C**
Oxygen	Flat structure	Flat domain structure - hard
Neon	Flat structure – soft	Columnar structure
Argon	Flat structure – soft	Columnar structure
Xenon	Flat structure – soft	Columnar structure

In general, the ITO film surfaces had a flat appearance for films deposited at T_s = 25°C. Height differences, measured over the surface, were within a few nanometers only. Above the surface, individual islands or possible particulates of heights between 10 to 20 nm appeared.

No particular structure could be identified for the ITO films deposited at T_s = 25° in good agreement with the supposed amorphous structure of these films. As a rule, ITO films deposited in the inert gases at room temperature had poor adhesion to the substrate, i.e. the films were soft and could rather easily be scratched with a scalpel. This may be related to the poor quality of these films, i.e. a supposed high defect density.

In contrast, the film deposited in oxygen at T_s = 200°C was hard and could not be scratched without damaging the film-substrate system as a whole. Furthermore, some domain-like structure could be identified on the surface of this film which indicated an improved crystalline structure relative to the film deposited at T_s = 25°C. Individual islands above the surface could be identified on this film as well.

The films deposited in the inert gases at T_s = 200°C had a significant columnar structure on the surface. The difference in heights between columns on a film surface could be up to 50 nm.

The melting temperature of ITO is around $T_m \approx 1910°C$ [42] which means that $T_s/T_m \approx 0.14 - 0.22$ for the ITO films. According to subsection 2.3.3, structures belonging to *zone 1* or *zone T* are then expected to develop during ITO film growth[11]. However, it is difficult precisely to classify the growth regimes for the ITO films in Table 5-3. According to the AFM measurements, the films deposited in inert gases at $T_s = 200°C$ seem to belong to *zone T*, which is a typical structure for energy-enhanced deposition processes such as PLD.

The ITO films deposited at $T_s = 25°C$ probably belong to *zone 1*, where surface diffusion is negligible during deposition. However, there may be large differences in the void fractions of these films.

The void fraction in the ITO films may depend on, e.g., the rate of self-shadowing during film growth – i.e. the fact that atoms already deposited may shadow lower lying areas in the growing film from deposition [43]. Self-shadowing depends among other things on the incident angles (to the substrate) of the ablated particles that again depend on the operating pressure during deposition. Raising the pressure during PLD spreads the range of incident angles and may increase self-shadowing.

According to Smith [43] one can determine the film deposition regime by the Knudsen number, $Kn = \Lambda/h$, where Λ is the mean free path of ablated particles and h a characteristic dimension in the deposition process. Here, h is, e.g., the target-substrate distance. For $Kn > 1$, the deposition is in the molecular flow regime, and for $Kn < 0.01$ the process is in fluid flow. For processes such as PLD the operating pressure can span the deposition range from molecular to fluid flow. In our case, according to subsection 4.1.2, the deposition is in an intermediate regime with $Kn \leq 0.1$. Thus, the ablated particles do not arrive at the substrate with a random angular distribution as is the case for fluid flows. However, some spread in the range of incident angles may occur and, as a result, voids may appear in the films, the rate depending, e.g., on the operating pressure. In contrast, it should be noted that the rather high translational kinetic energies of the ablated particles in laser deposition may reduce the void fraction by momentum transfer to atoms at the growing surface.

Only one example of a measure of a void fraction for laser deposited films has been found. Afonso *et al.* [44] reported on void fractions of less than a few percent for Ge films deposited by PLD at room temperature using an ArF laser (193 nm, 12 ns). However, no details of the deposition parameters were given and, therefore, higher void fractions for the ITO films presented in this chapter may be possible.

For films deposited in oxygen at $T_s = 200°C$ two possibilities exist. Either the films belong to *zone T*, i.e. consist of columns that terminate at equal heights giving the smooth surface, or the films belong to *zone 2*, i.e. consist of crystalline columns with few defects. The latter possibility is supported by recent measurements by Kim *et al.* [2] who measured the grain size of laser deposited ITO films as a function of growth temperature using AFM. The grain size of their films deposited in oxygen increased with increasing T_s (range 100° to 300°C), which is expected for *zone 2* growth [43].

Concerning the growth mechanism, Sun *et al.* [45] studied the initial growth mode of laser deposited ITO on glass (ArF laser, ~ 1 J/cm^2) by looking at the film thickness for onset of conductivity and comparing it with x-ray diffraction measurements. They claimed that the initial growth was always island formation in the temperature range studied (25° - 350°C), and that below T_s = 150° - 200°C these islands grew in three dimensions similar to the Volmer-Weber mechanism (see subsection 2.3.1). Above T_s = 150° - 200°C they claimed that

11 The different structural *zones* are described in subsection 2.3.3

these islands typically became one unit cell thick and then grew laterally in a two-dimensional manner according to the Frank-van der Merwe mechanism.

The islands or particulates observed at the surface of the laser deposited ITO films may be produced by, e.g., cluster condensation from vapour species or mechanically ejected target species (see subsection 2.3.3). We did not study or try to inhibit particulate formation in the work presented in this thesis.

5.5 Summary

In this chapter a comprehensive study of laser deposited ITO films has been presented. The study included an examination of how the electrical and optical properties, as well as, the composition and structure of the ITO films depend on specific experimental parameters such as the type of background atmosphere, the gas pressure and the substrate temperature.

At ITO deposition at room temperature, the dynamics of the ablated particles *prior* to deposition seem essential to film growth: the type of background gas and pressure chosen during deposition control, to some extent, the stoichiometry and defect density of the ITO films, the defects being, e.g., oxygen vacancies. The film composition is important for the electrical properties, whereas the defect density and, thus, the film structure seem important for the optical properties. An oxygen background gas during deposition at room temperature improves the ITO film structure.

Depositing at higher substrate temperatures mainly improves the crystallinity of the ITO films and, subsequently, the charge carrier mobility that in turn improves the film resistivity. In addition, the defect density seems to be reduced, and at deposition in oxygen the ITO film stoichiometry is improved as well.

Table 5-4 shows the ITO resistivity results obtained in this work, i.e. the work presented in chapters 5 and 6. ITO resistivity data obtained by other groups have also been included. It should be noted that uncertainties in the resistivity values have not been included in the table.

Table 5-4 Comparison between resistivity data for ITO films deposited on glass by PLD. T_s; substrate temperature. ρ_{min}; resistivity minimum. λ; laser wavelength. F; laser fluence.

T_s [°C]	ρ_{min} [10^{-4} Ωcm]	*Gas*	λ [nm]	F [J/cm^2]	*Reference/Year*
25	**190**	**O_2**	**355**	**0.5 – 0.8**	**This work/1999**
25	**190**	**Ne**	**355**	**0.5 – 0.8**	**This work/1999**
25	**8**	**O_2**	**355**	**1.9**	**This work/1999**
25	3(÷)	O_2	355	10 - 20	Cali *et al*. [46]/1998
25	5.4*	O_2	248	3	Adurodija *et al.*[27]/1999
25	4	O_2	248	~2	Wu *et al.* [28]/1999
25	3.8	O_2	248	2 (30 ns)	Kim *et al*. [2]/1999
20	5.6	O_2	193	1 (15ns)	Zheng, Kwok[24]/1993
200	**2**	**O_2**	**355**	**0.5 – 0.8**	**This work/1999**
200	**11**	**Ar**	**355**	**0.5 – 0.8**	**This work/1999**
200	**2.6**	**O_2**	**355**	**1.9**	**This work/1999**
200	2.1	O_2	248	2 (30 ns)	Kim *et al.* [2]/1999
200	1.8*	O_2	248	3	Adurodija *et al.* [27]/1999
200	2	O_2	193	1 (15ns)	Zheng, Kwok [30]/1993
250	3	O_2	193	5 – 9	Coutal *et al.* [23]/1996

(÷): No reports on film transmission. *: Substrates of SiO_2 glass or Si.

The resistivity results presented in the table demonstrate, that despite the relatively long wavelength of 355 nm used for ablation throughout this work it is possible to obtain high-quality ITO films at low substrate temperatures. These films are competitive to ITO films deposited at shorter UV wavelengths.

A wavelength of 355 nm corresponds to an energy of around 3.49 eV, which is just below the band-gap of In_2O_3 (around 3.75 eV). In contrast, 248 and 193 nm correspond to energies around 5.00 and 6.42 eV, which are far above the band-gap and, therefore, a significantly higher absorption in the ITO targets occurs as these wavelengths.

An Nd:YAG laser, which has been used in this work, is a solid state laser and, thus, fairly easy and safe to operate. It is expected that Nd:YAG lasers will become smaller, operationally simpler and more powerful in the future. In contrast, excimer lasers, which provide the low UV wavelengths, are gas lasers. Therefore, they are typically more complicated than the YAG laser, they are bigger and they may need constant supply of gas. From an operationally point of view, Nd:YAG lasers are to be preferred and by quadrupling the laser it has the possibility of operating at 266 nm. However, at present it is difficult to obtain sufficient laser power at this wavelength with a beam with an acceptable intensity profile.

5.6 References

1 H.L. Hartnagel, A.L. Dawar, A.K. Jain, C. Jagadish: *Semiconducting Transparent Thin Films* (Institute of Physics Publishing, Bristol 1995)

2 H. Kim, A. Pique, J.S. Horwitz, H. Mattoussi, H. Murata, Z.H. Kafafi, D.B. Chrisey: Appl. Phys. Lett. **74**, 3444 (1999)

3 J.C.C. Fan, F.J. Bachner, G.H. Foley: Appl. Phys. Lett. **31**, 773 (1977)

4 W.-F. Wu, B.-S. Chiou, S.-T. Hsieh: Semicond. Sci. Technol. **9**, 1242 (1994)

5 M.C. de Andrade, S. Moehlecke: Appl. Phys. A **58**, 503 (1994)

6 I. Hamberg, C.G. Granqvist: J. Appl. Phys. **60**, R123 (1986)

7 R.B.H. Tahar, T. Ban, Y. Ohya, Y. Takahashi: J. Appl. Phys. **83**, 2631 (1998)

8 J.C.C. Fan, J.B. Goodenough: J. Appl. Phys. **48**, 3524 (1977)

9 M. Kamei, T. Yagami, S. Takaki, Y. Shigesato: Appl. Phys. Lett. **64**, 2712 (1994)

10 W.-F. Wu, B.-S. Chiou: Appl. Surf. Sci. **68**, 497 (1993)

11 Y. Shigesato, D.C. Paine: Thin Solid Films **238**, 44 (1994)

12 Z. Ovadyahu, B. Ovryn, H.W. Kraner: J. Electrochem. Soc. **130**, 917 (1983)

13 L.A. Ryabova, V.S. Salun, I.A. Serbinov: Thin Solid Films **92**, 327 (1982)

14 N.W. Ashcroft, N.D. Mermin: *Solid State Physics* (W.B. Saunders Company, Philadelphia 1976)

15 A.L. Dawar, J.C. Joshi: J. Mater. Sci. **19**, 1 (1984)

16 L. Meng, A. Macarico, R. Martins: Vacuum **46**, 673 (1995)

17 K. Suzuki, N. Hashimoto, T. Oyama, J. Shimizu, Y. Akao, H. Kojima: Thin Solid Films **226**, 104 (1993)

18 F. Simonis, M.V. Leij, C.J. Hoogendoorn: Solar Energy Mater. **1**, 221 (1979)

19 *Optical Properties of Solids*, F. Wooten (Academic Press, New York 1972)

20 T. Maruyama, K. Fukui: J. Appl. Phys. **70**, 3848 (1991)

21 N. Balasubramanian, S. Subrahmanyam: J. Phys. D: Appl. Phys. **22**, 206 (1989)

22 H. Köstlin, R. Jost, W. Lems: Phys. Stat. Sol. A **29**, 87 (1975)

23 C. Coutal, A. Azéma, J.-C. Roustan: Thin Solid Films **288**, 248 (1996)

24 J.P. Zheng, H.S. Kwok: Thin Solid Films **232**, 99 (1993)

25 C.R. Tellier, A.J. Tosser: *Size Effects in Thin Films* (Elsevier Scientific Publishing, Amsterdam 1982)

26 B. Thestrup, J. Schou, A. Nordskov, N.B. Larsen: Appl. Surf. Sci. **142**, 248 (1999)

27 F.O. Adurodija, H. Izumi, T. Ishihara, H. Yoshioka, K. Yamada, H. Matsui, M. Motoyama: Thin Solid Films **350**, 79 (1999)

28 Y. Wu, C.H.M. Marée, R.F. Haglund, J.D. Hamilton, M.A.M. Paliza, M.B. Huang, L.C. Feldman, R.A. Weller: J. Appl. Phys. **86**, 991 (1999)

29 R.F. Wood, K.R. Chen, J.N. Leboeuf, A.A. Puretzky, D.B. Geohegan: Phys. Rev. Lett. **79**, 1571 (1997)

30 J.P Zheng, H.S. Kwok: Appl. Phys. Lett. **63**, 1 (1993)

31 R. Teghil, V. Marotta, A.G. Guidoni, T.M. Di Palma, C. Flamini: Appl. Surf. Sci. **138-139**, 522 (1999)

32 R. Gomez-San Roman, R.P. Casero, C. Maréchal, J.P. Enard, J. Perrière: J. Appl. Phys. **80**, 1787 (1996)

33 A. Gupta: J. Appl. Phys. **73**, 7877 (1993)

34 R. Pommier, C. Gril, J. Marucchi: Thin Solid Films **77**, 91 (1981)

35 G. Frank, H. Köstlin: Appl. Phys. A **27**, 197 (1982)

36 W.-F. Wu, B.-S. Chiou: Thin Solid Films **247**, 201 (1994)

37 F. Hanus, A. Jadin, L.D. Laude: Appl. Surf. Sci. **96-98**, 807 (1996)

38 I.P. Herman: *Optical Diagnostics for Thin Film Processing* (Academic Press, San Diego 1995) p. 99

39 SPECS manual for the ion source IQE 10/35

40 J. Goschnick, J. Schuricht, A. Schweiker, H.J. Ache: Nucl. Inst. and Meth. in Phys. Res. B **83**, 339 (1993)

41 *Topics in Applied Physics. Sputtering by Particle Bombardment II*, ed. by R. Behrisch (Springer-Verlag, Berlin 1983)

42 Data sheet for ITO sputtering targets from Target Materials, Inc.

43 D.L. Smith: *Thin-Film Deposition: Principles and Practice* (McGraw-Hill, New York 1995)

44 C.N. Afonso, J. Gonzalo: Nucl. Instr. and Meth. in Phys. Res. B **116**, 404 (1996)

45 X.W. Sun, H.C. Huang, H.S. Kwok: Appl. Phys. Lett. **68**, 2663 (1996)

46 C. Cali, M. Mosca, G. Targia: Solid-State Electronics **42**, 877 (1998)

6 Deposition of AZO and ITO films at high laser fluence

Aluminium-doped zinc oxide (AZO) films are a promising alternative to indium tin oxide (ITO) films. AZO films are almost as good conductors as ITO films and have good optical properties. In addition, zinc is a cheap, abundant and non-toxic material, whereas indium is comparatively expensive [1].

In this chapter, results that compare the materials properties of AZO and ITO films deposited by PLD on glass at high laser fluence (around 2.0 J/cm^2) are presented. The first section concerns general material properties of AZO. In the second and third sections, the electrical and the optical properties, respectively, of the AZO and ITO films are presented and analysed. The fourth section deals with the surface structure and the crystallinity of the films. A summary of the chapter is given in section five. A description of the experimental setup and methods used for the film deposition was given in chapter 3.

6.1 Aluminium-doped zinc oxide

Undoped zinc oxide (ZnO) is a wide band-gap (E_g = 3.2 –3.3 eV at room temperature), n-type semiconductor that crystallises in the hexagonal wurtzite (B 4-type) structure [2,3]. The conduction in ZnO is due to deviations from stoichiometry, i.e. mainly controlled by interstitial Zn atoms and O vacancies (giving free carriers). However, un-doped ZnO films have long term unstable electric properties. This instability is related to the change in surface conductance of ZnO films during oxygen chemisorption and desorption [3]. Doping ZnO with, e.g., aluminium, where Al^{3+} ions substitute Zn^{2+} ions, improves the electrical properties of the material as well as the material stability.

In contrast to In_2O_3 the band structure of ZnO has been calculated by many workers, see, e.g., [3] for references. The first two conduction band states are strongly localised on Zn and correspond to unoccupied Zn:3s levels. The highest lying valence bands correspond to O:2p bonding states. Doping with aluminium introduces doping levels in the band structure.

In the present work, AZO targets consisting of 2 wt% Al_2O_3 and 98 wt% ZnO were chosen, which corresponds to 1.6 at% aluminium, 48.0 at% zinc, and 50.4 at% oxygen. Studies of electrical properties of laser deposited AZO films indicated that an Al_2O_3 concentration around 1.5 – 2 wt% in AZO targets gives the lowest resistivities [4,5].

6.2 Electrical properties

This section deals with the relationship between the electrical resistivity of laser deposited AZO and ITO films and three of the experimental parameters of interest during film deposition: oxygen background gas pressure, substrate temperature, and laser fluence.

6.2.1 Background gas effects / non-heated substrates

Figures 6-1 and 6-2 show the resistivity versus oxygen pressure for series of AZO and ITO films deposited on glass at a fluence around 2.0 J/cm^2.

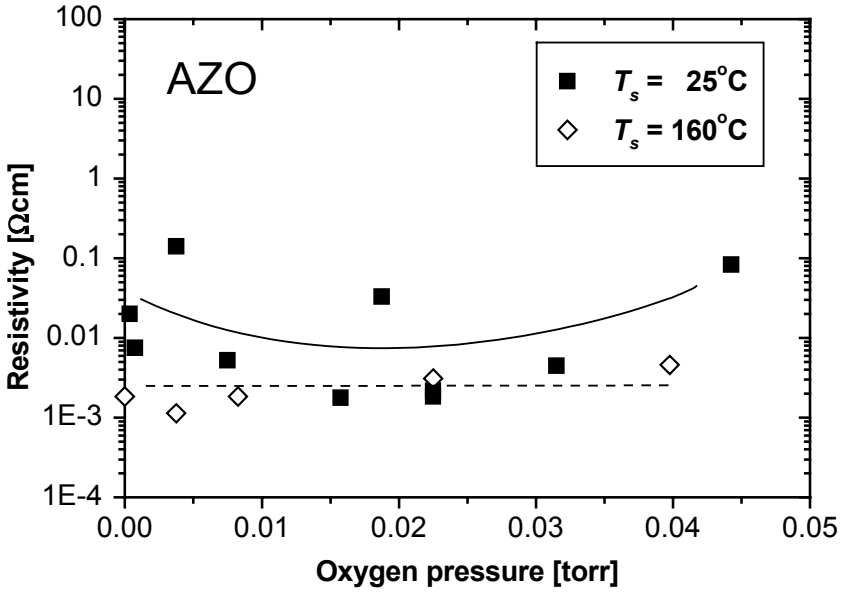

Figure 6-1 Resistivity versus oxygen pressure for AZO films deposited on glass at a fluence of 2.0 J/cm^2 at two different substrate temperatures, T_s. Lines are for guidance only.

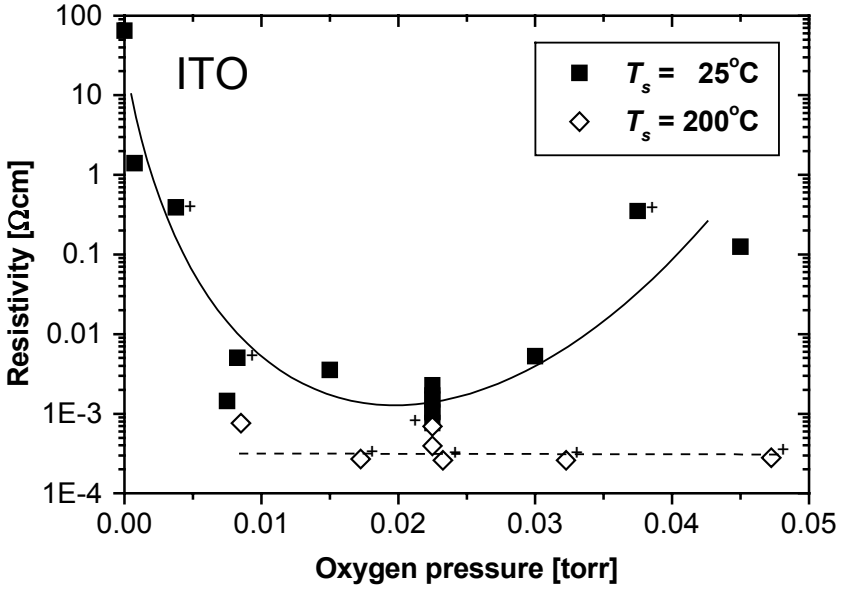

Figure 6-2 Resistivity versus oxygen pressure for ITO films deposited on glass at a fluence of 1.9 J/cm^2 at two different substrate temperatures, T_s. Lines are for guidance only. +: Data from [6], fluence 1.6 J/cm^2.

The AZO and ITO films were deposited on glass substrates at temperatures, T_s, of 25°C, 160°C or 200°C, respectively. The film thickness was between 150 and 380 nm (AZO films) or 180 and 980 nm (ITO films). Whenever possible, the film thickness was estimated from the film transmission spectra using equation (3-4). With regard to the AZO films, the thickness was also calculated from measured deposition rates adopting the film density from the target manufacturer of AZO. As mentioned in subsection 4.2.3, the latter method is very sensitive to laser alignment especially at low background gas pressures. In general, good agreement (within 25% relative uncertainty) was obtained between the two methods. At oxygen pressures between 10^{-6} and 0.01 torr, and a substrate temperature of 160°C, the relative error ranged from 35 to 47%. In Figures 6-1 and 6-2 the scattering of the data points for the same pressure value indicates the reproducibility.

The specific resistivity, ρ, for AZO films deposited at T_s = 25°C varies significantly with oxygen pressure – see Figure 6-1. The scattering of data points for ρ is almost over two orders of magnitude with a minimum of $\rho = 0.0018$ ($\pm 4.5 \cdot 10^{-4}$) Ωcm at an oxygen pressure of 16 mtorr. At lower and at higher pressures, the resistivity tends to increase even though some scattering of the data is noted. The variation of resistivity with oxygen pressure may be a consequence of the oxygen gas acting as a time-of-flight moderator as discussed in section 5.2.1. In order to achieve films of good quality at T_s = 25°C, the different particles in the laser ablated plasma plume must arrive at the substrate at equal times.

Other research groups have grown AZO films on glass by PLD at room temperature as well. Hiramatsu *et al.* [5] reported on an AZO film with $\rho \approx 0.0035$ Ωcm grown in 30 mtorr of oxygen with an XeCl excimer laser (308 nm, 1.5 J/cm^2), but, no indication of the film transmission was given. Suzuki *et al.* [4] produced a highly transparent AZO film with $\rho \approx 0.001$ Ωcm. The film was grown with an oxygen flow (1 cm^3/min) into the plume using an ArF excimer laser (193 nm, 1 J/cm^2). When operating in vacuum (base pressure $5 \cdot 10^{-8}$ torr), they claimed to have obtained a resistivity as low as $5.6 \cdot 10^{-4}$ Ωcm; however, with some reduction in the film transmission. Just recently, Kim *et al.* [7] reported on a transparent AZO film with $\rho \approx 9 \cdot 10^{-4}$ Ωcm deposited with a KrF excimer laser (248 nm, 2 J/cm^2). Thus, our results for AZO films deposited at T_s = 25°C are comparable with previous work, although it seems possible that a combination of improved vacuum conditions and stronger material absorption at shorter UV wavelengths may enhance the conduction in the deposited films.

The resistivity varies strongly with pressure for ITO films grown at room temperature as well. In contrast to AZO, a significantly high resistivity ($\rho \approx 64$ Ωcm) was observed for the ITO film grown in vacuum. However, ITO films produced in an oxygen environment between 7 and 30 mtorr seemed to have almost a constant low resistivity. The lowest resistivity, $\rho = 7.6 \cdot 10^{-4}$ ($\pm 1.2 \cdot 10^{-4}$) Ωcm at T_s = 25°C was obtained for an ITO film grown at an oxygen pressure of 23 mtorr.

The significantly higher resistivity obtained at vacuum for ITO than for AZO may, among other things, be connected to the difference in mass for the metals involved relative to the mass of the oxygen particles. Assuming that the particles have equal initial energies, a difference in mass results in a difference in arrival times at the substrate during ablation.

One may consider a very simplified example that ignores charge effects, mutual collisions, etc. Assume the initial transversal kinetic energy, E_0, of an In, Sn, O, Al, and Zn atom is 10 eV, and that these atoms travel at constant velocities, v_t, towards the substrate in a straight line. The arrival times, t_A, for the different atoms at the substrate placed 6 cm away would then be $t_A(In) \approx t_A(Sn) \approx$ 15 μs, $t_A(O) \approx 5$ μs, $t_A(Zn) \approx 11$ μs, $t_A(Al) \approx 7$ μs (assuming $E_0 = \frac{1}{2} M v_t^2$, where

M is the atomic mass). Thus, relative to oxygen, in this example the In and Sn atoms take three times as long time to reach the substrate, whereas the Zn atom only takes twice as long time. Therefore, if the time-of-flight (TOF) distributions (at the substrate) of the different particles in the plume must overlap in order to achieve films of good quality, the probability is higher in vacuum for AZO than for ITO.

6.2.2 Substrate temperature effects / heated substrates

The resistivity remains almost constant over the applied pressure range for the AZO films deposited at 160°C – see Figure 6-1. This is probably a result of a high diffusion rate of ablated particles on the film surface during film growth at T_s = 160°C (see subsection 5.2.2). The arrival times of the different particles at the film surface are less critical at an increased diffusion rate. Thus, the local crystallinity of films deposited at T_s = 160°C is improved relative to films deposited at T_s = 25°C. This is confirmed by X-ray measurements as described in subsection 6.4.2.

The lowest resistivity reported is $\rho = 0.0011$ ($\pm 4.7 \cdot 10^{-4}$) Ωcm at 3.8 mtorr, and is only slightly better than for the best film deposited at 25°C. This result is somewhat surprising. Generally, it is expected that an increase in substrate temperature (above a certain critical temperature) will improve the film structure and thus increase the charge carrier mobility considerably [8], but apparently it does not seem to be the case here. Results from Suzuki *et al.* [4] and Hiramatsu *et al.* [5] indicated that an enhancement in substrate temperature to 300°C should lower the resistivity further. Both groups obtained resistivities for laser deposited AZO films that were as low as approximately $1.4 \cdot 10^{-4}$ Ωcm at T_s = 300°C. Recently, Kim *et al.* [7] have examined the resistivity of laser deposited AZO films as a function of substrate temperature in the range 25° - 400°C. They obtained a minimum in ρ of $3.8 \cdot 10^{-4}$ Ωcm at T_s = 200°C.

ITO films deposited at 200°C show no specific change in resistivity within the pressure range applied and have substantially lower resistivities than those deposited at room temperature. The lowest resistivity measured is $2.6 \cdot 10^{-4}$ ($\pm 4.5 \cdot 10^{-5}$) Ωcm at 23 and 32 mtorr, which is considerably lower than for the AZO films deposited at 160°C.

6.2.3 Fluence effects

A decrease in laser fluence may lead to a decrease in deposition rate during film growth (see Figure 4.1), which again may have an influence on the nucleation rate at the film surface during deposition – see subsection 2.3.1. This may subsequently affect, e.g., the electrical properties of the deposited film.

Figure 6-3 shows the resistivity versus oxygen pressure of a series of AZO films deposited at two different substrate temperatures at a fluence of 1.4 J/cm^2 (film thickness between 80 and 570 nm). This fluence is slightly lower than the one used for the AZO films presented in Figure 6-1. A comparison between Figures 6-1 and 6-3 demonstrates that decreasing the laser fluence from 2.0 J/cm^2 to 1.4 J/cm^2 deteriorates the conductivity of the AZO films. Especially, AZO films deposited at high oxygen pressure, i.e. above 23 mtorr, have a relatively high resistivity.

Furthermore, Figure 6-3 shows that the resistivity, ρ, of the AZO films deposited at T_s = 25°C and at 1.4 J/cm^2 varies with more than three orders of magnitude with pressure. A minimum of $\rho \approx 0.0091$ Ωcm is observed only at a specific oxygen pressure of around 20 mtorr.

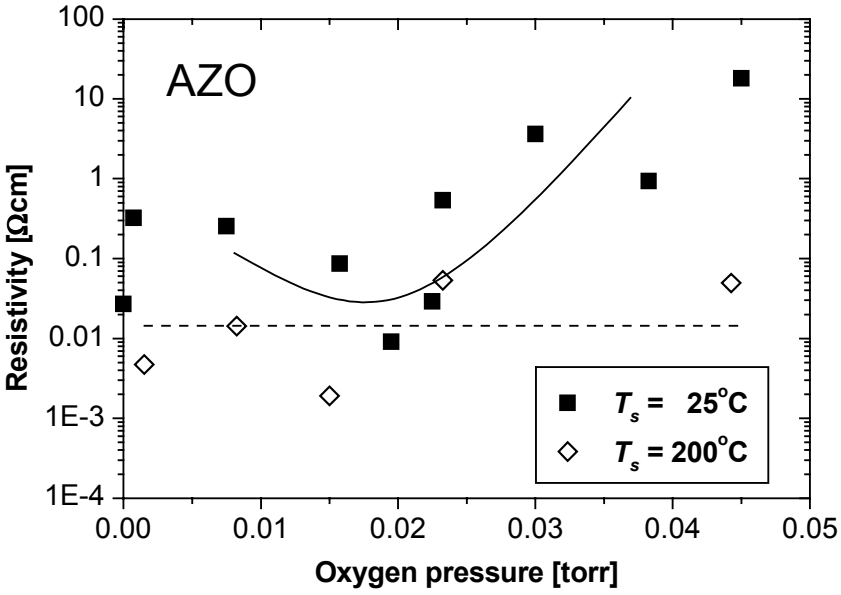

Figure 6-3 Resistivity versus oxygen pressure for AZO films deposited on glass at a fluence of 1.4 J/cm^2 at two different substrate temperatures, T_s. Lines are for guidance only.

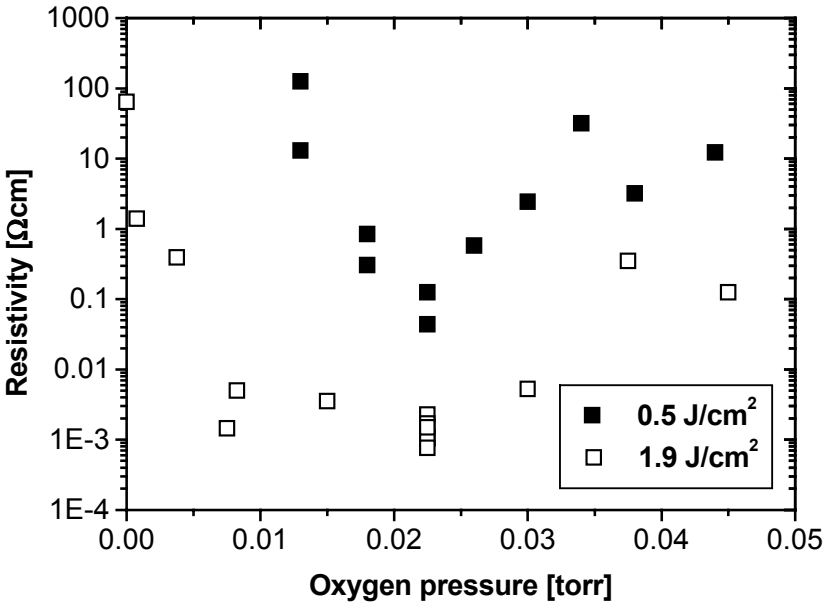

Figure 6-4 Resistivity versus oxygen pressure for ITO films deposited on glass at room temperature at two different laser fluences. Data from Figures 5-5 and 6-2. The scattering of the data point for the same pressure value indicate the reproducibility.

Figure 6-4 compares the resistivity behaviour (with oxygen pressure) of ITO films deposited at laser fluences of around 1.9 J/cm^2 and around 0.5 J/cm^2 (at T_s = 25°C).

Here a significant laser fluence effect is observed as well. An increase in fluence for laser deposited ITO films (at room temperature at 355 nm) has at least two effects which may be identified for the AZO films also; a decrease in the resistivity throughout the pressure range measured and a widening of the optimum pressure range where low resistivity films are obtained. These effects are probably caused by at least three mechanisms:

1. Enhancement of the nucleation rate at the film surface during film growth as mentioned above.

An increase in the nucleation rate during film growth may, at least for Volmer-Weber growth, improve the film quality which, in turn, is expected to give a decrease in the film resistivity.

2. Broader time-of-flight (TOF) distributions at the film surface for the ablated particles.

It has been demonstrated that an increase of laser fluence from 0.8 J/cm^2 to 2.5 J/cm^2 during ablation of silver at normal incidence[12] significantly broadens the corresponding TOF distribution (measured at the target normal) of ablated silver ions [9]. For multicomponent targets, as the ones used in the present work, a similar broadening of the TOF distributions of the different ions in the plasma plume is expected when the laser fluence is increased. Thereby the probability for the different particles to arrive at equal times at the film surface during film growth is enhanced as well. Furthermore, the optimum pressure range where the arrival times are equalised may become wider as is seen in, e.g., Figure 6-4.

3. Ineffective irradiation of the target at low fluence.

In appendix A it is demonstrated how the beam spot area on an ITO target increases with laser fluence until a fluence of around 1.7 J/cm^2. For higher fluences the beam spot area is almost constant which indicates that effective irradiation of the whole beam spot area is achieved. However, for fluence below around 1.7 J/cm^2 the target spot is ineffectively irradiated at the edge of the target spot due to the quasi-Gaussian intensity profile of the Nd:YAG laser beam. This may lead to non-stoichiometric ablation in the periphery of the target spot, where the laser energy density may be below the plasma creation threshold – see section 2.2 or [2].

6.3 Optical properties

In this section the AZO and ITO film transmission is examined as a function of oxygen gas pressure, substrate temperature, and laser fluence.

6.3.1 Background gas and substrate temperature effects

Figure 6-5 shows the average transmission, T_{Av}, between 450 and 750 nm versus oxygen pressure for representative AZO and ITO films deposited on heated and non-heated glass substrates at fluences around 2.0 J/cm^2. For the ITO films only those with thicknesses below 800 nm are included as the transmission seemed to decrease for thicker films.

12 Measured with the setup shown in Figure 3-5.

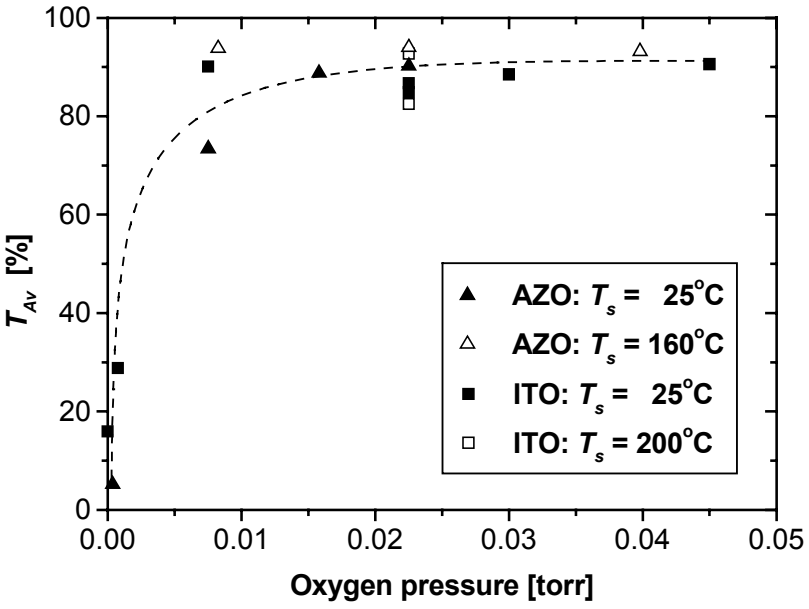

Figure 6-5 Average transmission, T_{Av}, between 450 and 750 nm versus oxygen pressure for selected AZO and ITO films deposited at fluences around 2.0 J/cm^2 at three different substrate temperatures, T_s. The line is for guidance only.

In general, the average film transmission was high for the AZO and the ITO films grown in oxygen on both heated and non-heated substrates. For films deposited at T_s = 25°C and at pressures above 15 mtorr, T_{Av} was above 85%. In contrast, T_{Av} was low (below 25%) for films grown in vacuum or at low oxygen pressures (< 10^{-3} torr) at 25°C. The AZO and ITO films grown at low pressure or vacuum at 25°C were dark brown.

It is possible to estimate the average absorption coefficient, α_{Av}, from the figure. In appendix C, the variation with oxygen pressure of the quantity $-\ln(T_{Av})/d$ is given, where d is the film thickness (T_s = 25°C). For low values of T_{Av} this quantity is roughly proportional to α_{Av} over the wavelength range measured (see equation (5-5)). The values of $-\ln(T_{Av})/d$ at the lowest oxygen pressures correspond to values of α_{Av} as high as $8 \cdot 10^4$ cm^{-1}. For comparison the absorption coefficient for pure silver in the same wavelength range is between $2 \cdot 10^5$ and $8 \cdot 10^5$ cm^{-1} [10]. The quantity $-\ln(T_{Av})/d$ decreases with increasing oxygen pressure (within the applied pressure range) with almost two orders of magnitude for both materials corresponding to a similar decrease in α_{Av}.

With regard to films grown on heated substrates, T_{Av} was above 90% for AZO films and above 82% for ITO films independent of oxygen pressure.

As a rule, T_{Av} is higher for the AZO films than for the ITO films at the optimum pressure (in the range 16 – 23 mtorr). The same tendency has also recently been observed by Kim *et al.* [7].

Transmission spectra of selected AZO and ITO films are shown in Figure 6-6. The ripples in the spectra are attributed to etalon interference effects produced at the air/film and film/substrate interfaces as mentioned in subsection 3.2.1.

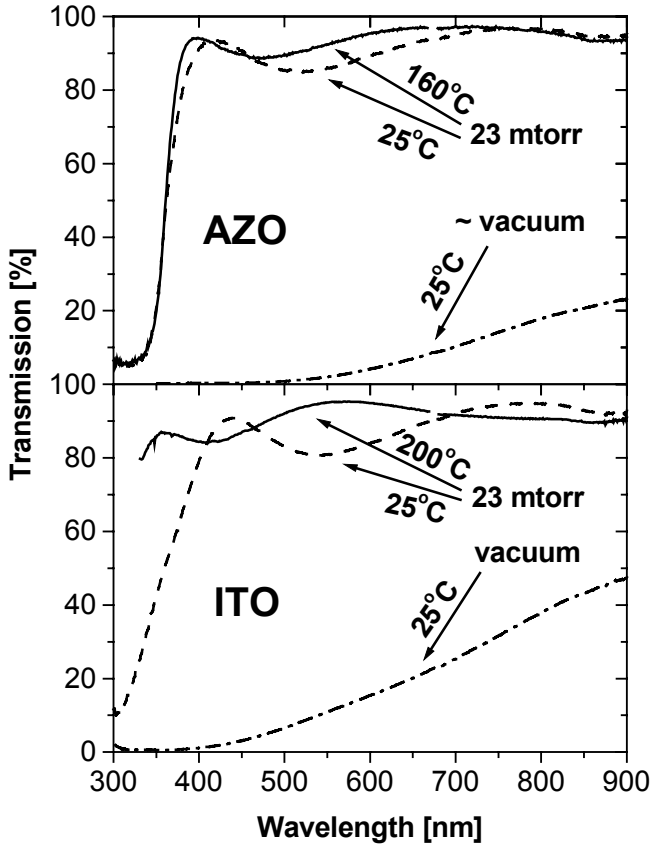

Figure 6-6 Transmission spectra of selected AZO and ITO films. Oxygen pressures and substrate temperatures are indicated. Film thicknesses from 180 to 260 nm.

Despite the striking similarity of the optical properties of the two materials some minor differences are noted as well. Firstly, at T_s = 25°C and an oxygen pressure of 23 mtorr, the AZO transmission curve has a sharper UV cut-off than the ITO curve. Thus, at 25°C AZO is transparent (i.e. transmission above 80%) from a shorter wavelength than ITO at the same oxygen pressure. Secondly, the optical window is significantly wider at T_s = 200°C than at T_s = 25°C for ITO films deposited at 23 mtorr. This effect may be ascribed to a Burstein-Moss shift of the energy gap at T_s = 200°C as the thickness of the two films is almost the same, around 200 nm (see also equation (5-3) and the discussion in section 5.3.2). Apparently, no such band-gap shift is observed for the AZO films.

In Table 6-1[13], rough estimates of the direct band-gap, E_g, for the AZO and ITO films presented in Figure 6-6 are given. Average transmission values are

13 Another ITO film, thicker than the one presented in the figure, was used to calculate the band-gap at T_s = 200°C.

included as well. The band-gaps were determined by plotting the square of the estimated absorption coefficient, α^2, versus photon energy, $h\nu$, and extrapolating the linear region of the plot towards zero absorption, as described in section 5.3.2.

Table 6-1 Estimated energy gap, E_g, and average transmission, T_{Av}, for films deposited in 23 mtorr oxygen. T_s: substrate temperature.

Material	T_s [°C]	E_g [eV]	T_{Av} [%]
AZO	25	3.45	90
AZO	160	3.43	94
ITO	25	3.64	87
ITO*	200	3.78	83

* Film thickness ~ 725 nm.

The estimated energy gap for the AZO film deposited at room temperature is in good agreement with recent results from Kim *et al.* [7]. They obtained, however, a higher band-gap value of E_g = 3.72 eV for an AZO film deposited at T_s = 200°C with a KrF excimer laser (248 nm). Concerning the average transmission values obtained for AZO, they are at least as good as those obtained by other groups [4,5,11] who have used shorter UV wavelengths (193, 308, 248 nm) for ablation.

The band-gap values obtained for the ITO films are in reasonable agreement with results from others. Coutal *et a*l. [12] reported on E_g = 3.72 eV for an ITO film deposited at 200° - 300°C using an ArF laser (193 nm). Kim *et al.* [13] have recently reported on band-gaps between 3.90 and 4.21 for ITO films deposited at temperatures between 25°C and 300°C using an KrF excimer laser (248 nm).

6.3.2 Fluence effects

The average ITO transmission, T_{Av}, for films deposited in oxygen (above 20 mtorr) at T_s = 25°C is significantly improved when the laser fluence is increased from 0.5 J/cm^2 to 1.9 J/cm^2. A comparison between Figures 6-5 and 5-10 (in chapter 5) demonstrates that the improvement is highest (around 30%) at the highest oxygen pressures. A tendency that confirms the importance of the plume particle dynamics during ITO film growth. Changes in laser fluence mainly affect the deposition rate [14], but can also modify the average kinetic energy of the ablated species [9]. An increase in kinetic energy of the oxygen particles during film growth may increase the incorporation of oxygen in the films at high oxygen gas pressure, which again is expected to increase the average transmission of the films as discussed in subsection 5.3.1.

Regarding the energy gap of ITO films deposited at T_s = 25°C, E_g seems higher for the films grown at high fluence as well. In contrast, the highest energy gaps are obtained at low fluence for ITO films deposited at T_s = 200°C (see subsection 5.3.2). No immediate explanation of this phenomenon can be given.

6.4 Film structure and crystallinity

Selected AZO and ITO films were examined by atomic force microscopy (AFM) and X-ray diffraction (XRD) in order to study the surface structure and

crystallinity of the films (see subsection 3.2.4). The experimental results are presented in this section.

6.4.1 Surface structure

Photos 6 to 9, in the "photo gallery" placed at the end of this thesis show surface images of AZO and ITO films deposited in 23 mtorr oxygen on non-heated (T_s = 25°C) and heated (T_s = 160°C, 200°C) glass substrates. The film thicknesses are around 186 – 232 nm.

The AFM images reveal that the ITO films were much smoother than the AZO films under equal deposition conditions. In general, the ITO surfaces were very smooth with variations in heights in the order of a nanometer. However, some particulates with heights of 10 to 30 nm were seen on the surfaces. The particulate density was lowest for the ITO film deposited at T_s = 25°C. The particulate heights were only around 10 nm for this film. Clear crystalline areas were observed on the surface of the ITO film deposited at T_s = 200°C.

For AZO the surface seemed to consist of large material pieces with steps between 10 to 100 nm. The film deposited at T_s = 25°C was slightly smoother than the film grown at T_s = 160°C. However, both AZO films were almost 50 times as rough as the corresponding ITO films.

Furthermore, AZO films deposited at low oxygen pressures (between 0.7 - 7.5 mtorr) were cracked in contrast to the smooth appearance of ITO films and AZO films deposited at other oxygen pressures. No explanation of this phenomenon can be given at present, except that the surface probably cracks due to surface stress combined with poor adhesion to the substrate [15]. Photo 10 in the photo gallery shows microscope pictures of a cracked surface for an AZO film of a thickness around 370 nm deposited in $7.4 \cdot 10^{-4}$ torr of oxygen at T_s = 25°C.

Structures belonging to *zones 1* or *T* are expected to develop in the AZO and the ITO films (see subsection 2.3.3) as the melting temperature, T_m, of the AZO target is around 1975°C (from the target manufacturer), close to the melting temperature of the ITO target. The AZO films could have the *zone 1* structure as broad dome-like structures are observed at the surface of these films. This means that the AZO films could grow according to the Volmer-Weber mode which is expected when the cohesive energy of the film atoms is greater than the cohesive binding between the film and the substrate atoms [16].

6.4.2 Film crystallinity

Figures 6-7 and 6-8 show XRD spectra of AZO and ITO films deposited in oxygen on non-heated and heated glass substrates. The spectra show the intensity of scattered radiation ($Cu_{K\alpha}$ radiation) as a function of scattering angle, 2θ (see the inset in Figure 6-7). The three spectra in Figure 6-7 may be compared quantitatively as they have been recorded with the same setup geometry.

The XRD pattern for the ITO film deposited at T_s = 25°C contains no crystallographic peaks, i.e. the film is amorphous as expected [17]. A diffuse scattering background is observed, for this film, where a substantial part is probably caused by the glass substrate.

The XRD patterns for the two AZO films deposited at T_s = 25°C and 160°C have a crystallographic peak at $2\theta \approx 34.3°$ which may be identified as the scattering peak from (002) planes [4,5]. This indicates the existence of crystallites in the films with the c-axis grown perpendicular to the plane of the glass substrate [18]. According to Lowndes [2] this is the preferred growth orientation for ZnO films.

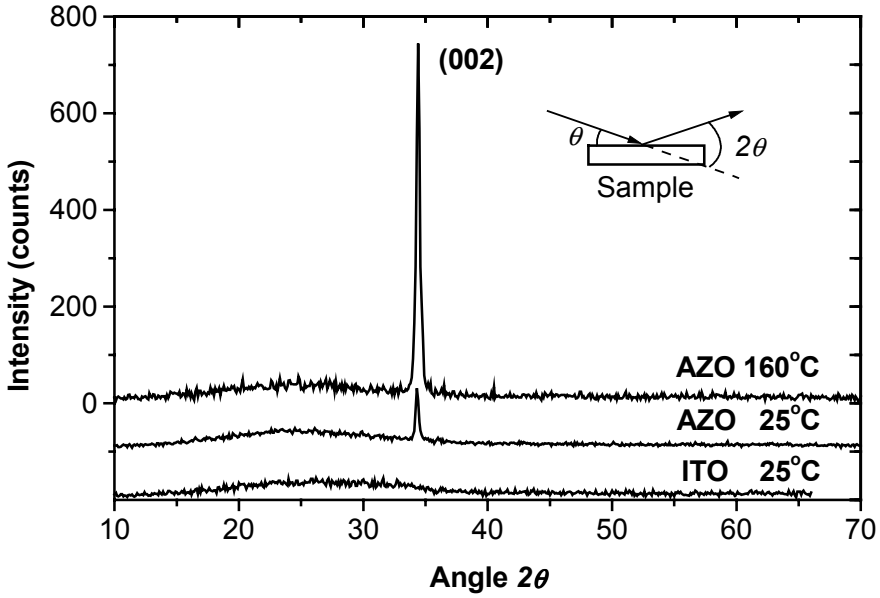

Figure 6-7 X-ray diffraction patterns (symmetric geometry) of films deposited in oxygen at 25 ℃ or 160 ℃. Oxygen pressure during deposition and film thickness are around: 187 nm, 0.38 mtorr (AZO 160 ℃), 163 nm, 15 mtorr (AZO 25 ℃),

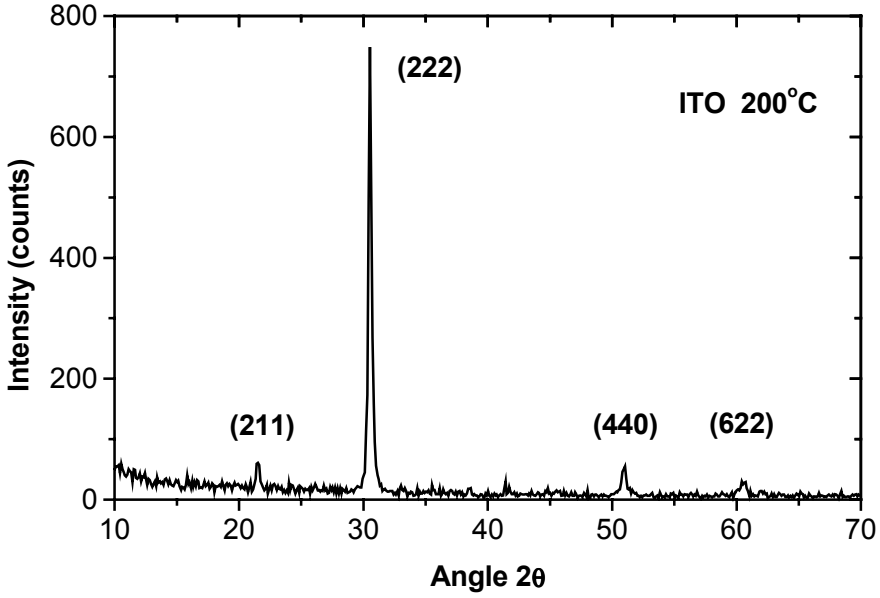

and 322 nm, 23 mtorr (ITO 25 ℃).

Figure 6-8 X-ray diffraction pattern (asymmetric geometry) of ITO film deposited in 23 mtorr oxygen at 200°C.

A less amount of crystalline material is expected in the AZO film grown at T_s = 25°C compared with the film grown at T_s = 160°C. This may be seen by comparing the intensity of the two (002) peaks as the two AZO films have almost equal thicknesses. Thus, the AZO film grown at T_s = 25°C should contain a significant amount of amorphous or randomly oriented material as well.

Ianno *et al.* [19] claimed to have observed a (002) peak in the XRD pattern of a laser deposited ZnO film grown on Si (100) at room temperature using a KrF excimer laser (248 nm). However, other groups [4,7] who have grown AZO films on glass by PLD at room temperature obtained films with randomly orientated material (AZO grown in vacuum at 193 nm and 1 J/cm^2) or amorphous films (AZO grown in 5 mtorr oxygen at 248 nm and 2 J/cm^2). Nevertheless, in accordance with our results, the two latter groups observed the (002) peak in XRD patterns for AZO films deposited at higher substrate temperatures.

Concerning the ITO film deposited at T_s = 200°C, the film is clearly polycrystalline as seen in Figure 6-8. The XRD spectrum contains four clear peaks corresponding to scattering from the crystallographic planes (211), (222), (440) and (622) [20] with (222) being the most intensive. Recently, other groups have presented XRD spectra of ITO films deposited by laser ablation at T_s = 200°C in oxygen containing these peaks as well [7,21].

6.5 Summary

AZO films seem to be a reasonable alternative to ITO films. Clearly, the electrical properties of ITO are superior to those of AZO under similar deposition conditions. Nevertheless, the optical properties of the AZO films are at least as promising as those for the ITO films and improvements in the deposition conditions may further increase the AZO film conductivity as well. The improvements can be operating at a different laser wavelength and with a different deposition rate – see below. As a rule, the deposition rate of AZO was considerably lower (~ 50%) than that of ITO under equal deposition conditions.

For commercial applications the surface of the ITO films was sufficiently smooth and indeed competitive to sputter deposited films [22]. However, the particulate density needs to be reduced. The reduction of particulates was not a subject of the present work, but there are several methods to reduce the particulate density and size [23]. In particular, the ITO films deposited at low fluence had a lower particulate density than the films deposited at high fluence.

The AZO films are at present too rough for commercial use. However, it has recently been demonstrated that it is possible to obtain smoother AZO films on silica substrates using different experimental settings [7].

Possibly, operating at shorter UV wavelengths is more crucial for AZO than for ITO. The absorption coefficients (and thus the characteristic penetration depths) of the two target materials are of the same order of magnitude[14] [24,25]. However, it is evident that operating at a wavelength corresponding to an energy far above the band-gap of ZnO (i.e. far below ~ 380 nm) would give more effective absorption of the laser light.

Craciun *et al.* [24,26] made some studies of the effect of laser wavelength on the ablation of a sintered ZnO target and on laser deposited ZnO films. They claimed that above a certain (wavelength dependent) laser fluence a possible

14 $\alpha \approx 10^4$ cm^{-1} at 532 nm and $\alpha \approx 5 \cdot 10^5$ cm^{-1} at 248 nm for the solid phase of a ZnO target. $\alpha \approx 2.2 \cdot 10^5$ cm^{-1} at 248 nm for an In_2O_3 solid. $\alpha \approx 2\text{-}6 \cdot 10^4$ at 355 nm for the ITO films in this work.

superheating effect during ablation of the ZnO target could lead to microexplosions within the melted material with subsequent adverse effects on film quality. For ablation with a KrF laser (248 nm) they found this fluence threshold to be around 3 J/cm^2, but they claimed that it appeared just above the ablation threshold for ablation with a frequency-doubled Nd:YAG laser (532 nm).

Ianno *et al.* [19] studied laser deposition of ZnO films as a function of laser wavelength and fluence as well. At ablation at 248 nm at room temperature they observed an improvement in film texturing when the fluence was decreased from 1 to 0.5 J/cm^2. Their ZnO films were deposited on silicon.

Therefore it may be possible that for ablation at 355 nm, as in this work, working closer to the ablation threshold would improve the deposited AZO films.

6.6 References

1 www.Goodfellow.com

2 D.H. Lowndes in *Laser Ablation and Desorption*, ed. by J.C. Miller, R.F. Haglund (Academic Press, San Diego 1998) pp. 475-571

3 H.L. Hartnagel, A.L. Dawar, A.K. Jain, C. Jagadish: *Semiconducting Transparent Thin Films* (Institute of Physics Publishing, Bristol 1995)

4 A. Suzuki, T. Matsushita, N. Wada, Y. Sakamoto, M. Okuda: Jpn. J. Appl. Phys. **35**, L56 (1996)

5 M. Hiramatsu, K. Imaeda, N. Horio, M. Nawata: J. Vac. Sci. Technol. A **16**, 669 (1998)

6 E. Holmelund, B. Thestrup, J. Schou (1999), unpublished

7 H. Kim, A. Piqué, J.S. Horwitz, C.D. Merritt, R. Schlaf, Z.H. Kafafi, C.M. Gilmore, D.B. Chrisey: Submitted to Proceedings of SPIE (July 1999)

8 S. Metev in *Pulsed Laser Deposition of Thin Films*, ed. by D.B. Chrisey, G.K. Hubler (Wiley, New York 1994) pp. 255-264

9 T.N. Hansen, J. Schou, J.G. Lunney: Appl. Phys. Lett. **72**, 1829 (1998)

10 *Charged particle and laser irradiation of selected materials*, W.E. Svendsen (Ph.D. Thesis, University of Copenhagen 1996) p. 89

11 Z.Y. Ning, S.H. Cheng, S.B. Ge, Y. Chao, Z.Q. Gang, Y.X. Zhang, Z.G. Liu: Thin Solid Films **307**, 50 (1997)

12 C. Coutal, A. Azéma, J.-C. Roustan: Thin Solid Films **288**, 248 (1996)

13 H. Kim, A. Piqué, J.S. Horwitz, H. Mattoussi, H. Murata, Z.H. Kafafi, D.B. Chrisey: Appl. Phys. Lett. **74**, 3444 (1999)

14 W. Svensen, J. Schou, B. Thestrup, O. Ellegaard: Appl. Surf. Sci. **96-98**, 518 (1996)

15 D.L. Smith: *Thin-Film Deposition: Principles and Practice* (McGraw-Hill, New York 1995) pp. 119-220

16 G.K. Hubler in *Pulsed Laser Deposition of Thin Films*, ed. by D.B. Chrisey, G.K. Hubler (Wiley, New York 1994) pp.327-355

17 X.W. Sun, H.C. Huang, H.S. Kwok: Appl. Phys. Lett. **68**, 2663 (1996)

18 S. Hayamizu, H. Tabata, H. Tanaka, T. Kawai: J. Appl. Phys. **80**, 787 (1996)

19 N.J. Ianno, L. McConville, N. Shaikh, S. Pittal, P.G. Snyder: Thin Solid Films **220**, 92 (1992)

20 L. Meng, M.P. dos Santos: Thin Solid Films **303**, 151 (1997)

21 F.O. Adurodija, H. Izumi, T. Ishihara, H. Yoshioka, H. Matsui, M. Motoyama: Jpn. J. Appl. Phys. **38**, 2710 (1999)

22 L. Meng, A. Maçarico, R. Martins: Vacuum **46**, 673 (1995)

23 L.-C. Chen in *Pulsed Laser Deposition of Thin Films*, ed. by D.B. Chrisey, G.K. Hubler (Wiley, New York 1994) pp. 167-198

24 V. Craciun, D. Craciun, M.C. Bunescu, R. Dabu, I.W. Boyd: J. Phys. D: Appl. Phys. **32**, 1306 (1999)

25 R.L. Wheeler, R.P. Ley: J. Appl. Phys. **37**, 299 (1966)

26 V. Craciun, S. Amirhaghi, D. Craciun, J. Elders, J.G.E. Gardeniers, I.W. Boyd: Appl. Surf. Sci. **86**, 99 (1995)

7 Holographic recording in AZO and ITO films

An interesting property of transparent, semiconducting materials is the possibility of modulating their optical parameters upon illumination.

A few years ago, holographic recording by UV illumination in sputter-deposited ITO and In_2O_3 films was demonstrated by Mailis *et al.* [1]. Recently, they have reported on holographic recording in laser deposited In_2O_3 films as well [2]. However, to our knowledge, holographic properties of other transparent, conducting oxides upon UV illumination have not been studied until now.

In this chapter it is demonstrated how optically induced gratings can be written in laser deposited AZO films as well as in ITO films, and the characteristics of grating formation in the two different materials are compared [3]. The first section gives an introduction to holographic gratings. The second section describes the experimental setup. In the third section the experimental results are presented and discussed and, finally, a summary of the chapter is given in section four.

7.1 Introduction to holographic gratings

In this section a brief introduction to holographic gratings is given. The main reference is [4].

The optical properties of a material such as the refractive index, n, and the absorption coefficient, α, may become spatially modulated in the interference region of two intense coherent light waves. The spatially modulated light field in the material is then called an interference grating. If the material modulation disappears when the inducing light source has been switched off, one is dealing with dynamic or transient gratings. One way of detecting these gratings is by diffraction, i.e. forced light scattering, of a probing light beam.

Typically, two laser beams from the same laser source are arranged to interfere in the material to create a grating. For most purposes it is convenient to use collimated TEM_{00} beams (i.e. the fundamental transverse electric magnetic mode of a laser beam) which are close to an ideal plane wave and provide plane gratings when brought to intersection. The probe beam may be taken from another laser source.

7.1.1 Production of a laser induced grating

The experimental arrangement for the production of laser-induced gratings is sketched in Figure 7-1. Only plane light waves are considered.

Light from a pump laser is split into two beams A and B with wave vectors $\boldsymbol{k_A}$ and $\boldsymbol{k_B}$, and intensities I_A, I_B. The two beams intersect at an angle θ at the sample and create an interference pattern, i.e. an intensity variation that can be written in the form

$$I(x) = I_0 (1 + M \cos (q \cdot x)) . \qquad (7\text{-}1)$$

Here the direction, x, is defined in Figure 7-1 and q is the length of the grating vector given by

$$\boldsymbol{q} = \boldsymbol{k_A} - \boldsymbol{k_B} \ . \qquad (7\text{-}2)$$

M is the intensity modulation coefficient that is given as

$$M = 2\,(I_A I_B)^{1/2} / I_0 \ . \qquad (7\text{-}3)$$

$I_0 = I_A + I_B$ is the total intensity. The spatial grating period is given as

$$\Lambda_G = 2\pi / q \ . \qquad (7\text{-}4)$$

Λ_G can be expressed in terms of the pump wavelength, λ_P, and the angle θ as

$$\Lambda_G = \lambda_P \cdot (2 \sin(\theta/2))^{-1} \ . \qquad (7\text{-}5)$$

The maximum value of Λ_G is limited by the diameter of the laser beam that induces the grating.

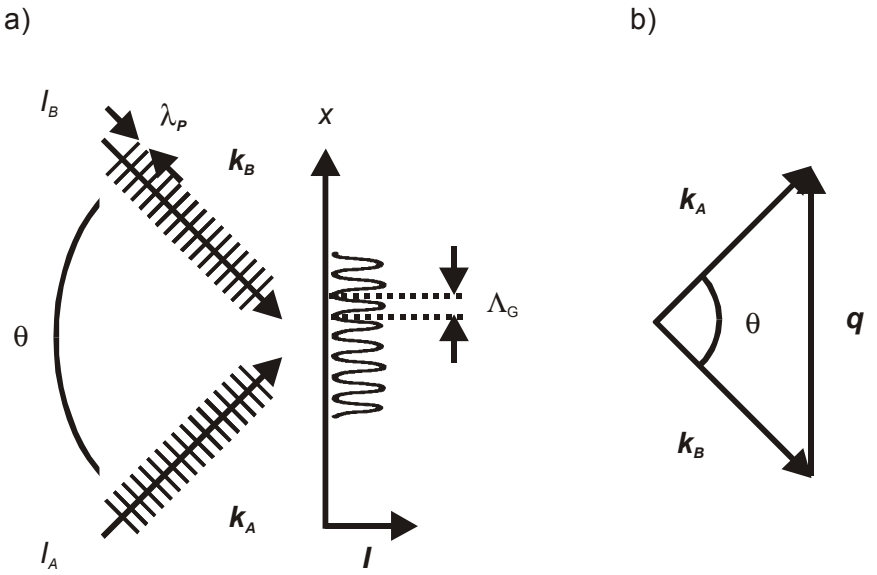

Figure 7-1 a) Intensity pattern created in a sample by interference of two light waves with intensities I_A and I_B and wave vectors $\boldsymbol{k_A}$ and $\boldsymbol{k_B}$, intersecting each other at an angle, θ. Λ_G is the grating period. b) Definition of the grating vector, $\boldsymbol{q}$.

7.1.2 Detection of a thin grating

Light-induced gratings can be probed with a third laser beam. Typically, the wavelength, λ_C, is chosen outside the photosensitive region of the sample material. In addition, the intensity, I_C, may be weakened, so that the probe beam does not influence the grating recording process.

In the sample some of the probe light will be diffracted into various directions by the grating. The characteristics of the diffraction process strongly depend on the thickness, d, of the sample. If d is of the order of the grating period, Λ_G, or smaller, the grating is called thin. Diffraction from a thin grating is shown schematically in Figure 7-2.

When the probe beam traverses the grating area, the radiation emitted from different parts of the grating interferes constructively only in certain directions with regard to the grating orientation and the probe beam direction. In other words, the direction of $\boldsymbol{q}$ and the probe beam wave vector, $\boldsymbol{k_C}$, determines the

possible directions for the diffracted beams. In the following, the probe beam is assumed to be incident normal to the sample, i.e. $\boldsymbol{k_C}$ is normal to $\boldsymbol{q}$.

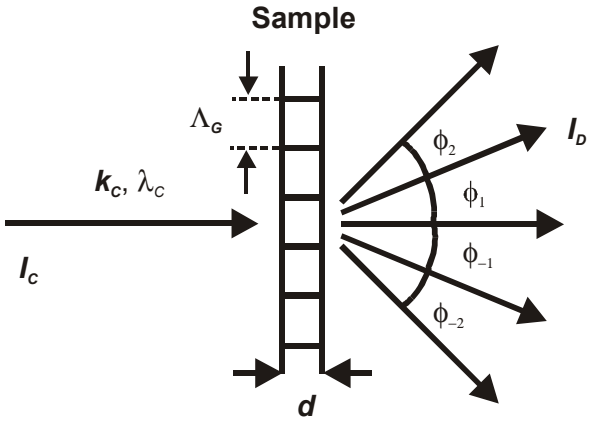

Figure 7-2 Characteristics of diffraction from a thin grating. The symbols are explained in the text.

The directions, φ_m, of the different diffracted beams are given as

$$\sin\varphi_m = m\,\lambda_C / \Lambda_G, \qquad m = \pm 1, \pm 2, \ldots . \qquad (7\text{-}6)$$

The intensities, I_m, of the different diffraction orders $m = \pm 1, \pm 2, \ldots$ are a measure for the modulation of the optical properties of the material. The diffraction efficiency, ξ, of the first order diffracted beam ($m = \pm 1$) is defined as the normalised intensity

$$\xi = I_D/I_C . \qquad (7\text{-}7)$$

Here I_D is the intensity of the first order diffracted beam.

The simplest types of gratings are phase and amplitude gratings, in which the absorption and the refractive index of the material are modulated due to the induced light. For gratings of this type, the diffraction efficiency is

$$\xi = |\,\pi\,\Delta\eta\,d / \lambda_C\,|^2 . \qquad (7\text{-}8)$$

Here $\Delta\eta$ is the modulation amplitude of the complex refractive index, $\eta = n - ik$, of the material and d is the sample thickness.

7.2 Experimental setup

The AZO and the ITO films used for holographic recording were produced by laser ablation on glass in an oxygen atmosphere at a fluence around 2 J/cm^2 – see chapter 6. Only films deposited at oxygen pressures between 16 and 40 mtorr were used in order to ensure that the films were electrically conducting and highly transparent. Typical deposition rates within this pressure range were 7 Å/s for AZO and 12 Å/s for ITO. The film thicknesses were between 180 and 730 nm.

In order to examine the holographic recording dynamics of the laser deposited AZO and ITO films, they were studied in the arrangement sketched in Figure 7-3. Two mutually coherent beams from a Kr-ion laser at a wavelength of 356.4 nm were symmetrically incident to the normal of the film plane. A UV beam splitter (not shown in the figure) was placed in the setup to create the two pump

beams that intersected each other at an angle of $\theta = 21.6°$. The beams were unexpanded (beams width 1.3 mm at $1/e^2$) and TE-polarised[15]. In the film the beams created an interference pattern and, thus, a diffraction grating. The intensity modulation coefficient, M, was kept constant at a value close to unity (M = 0.998). Typical total pump beam intensities were I_0 = 750 mW/cm^2 and I_0 = 1130 mW/cm^2.

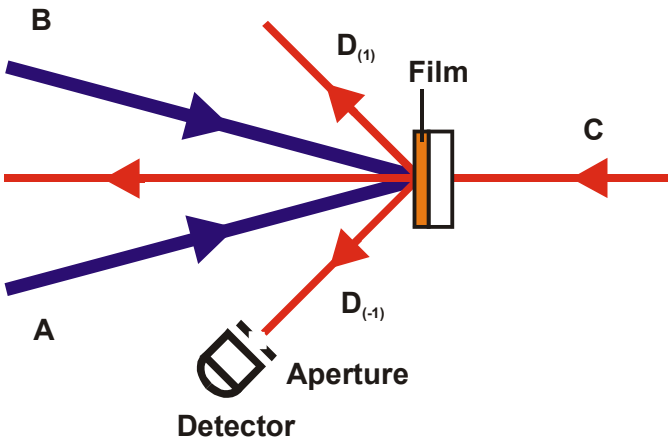

Figure 7-3 Arrangement for production and detection of laser induced gratings. A, B: pump beams. C: probe beam. $D_{(1)}$,$D_{(-1)}$: first-order diffracted beams.

A weak HeNe laser beam at a wavelength of 633 nm probed the grating at normal incidence to the film plane. The beam was TE-polarised as the pump beams (out of plane in Figure 7-3). The probe beam was amplitude modulated with an electro-optic modulator driven with a sine signal at 343.3 Hz from a frequency generator. Then, the first order diffracted beam was detected with a Si-detector using a lock-in amplifier to obtain a good signal-to-noise ratio. In addition, a red filter and a circular aperture were placed in front of the detector head. The temporal behaviour of the detected signal was digitised and stored using a PC.

As a rule, two or three different recordings were made in the same film at different well-separated locations.

7.3 Results and discussion

7.3.1 Experimental results

Figure 7-4 shows the transmission spectra of four selected films measured before holographic recording. Two AZO films deposited at substrate temperatures, T_s = 25° and T_s = 160°C, and two ITO films deposited at T_s = 25° and T_s = 200°. The oscillations in the transmission spectra, seen especially for the ITO films, are due to etalon interference effects between the air/film and film/substrate boundaries. The ITO films are 3-4 times thicker than the AZO films.

15 TE: transverse electric. The electric field vector of the incident waves is parallel to the film surface, i.e. out of plane in the figure.

As can be seen in the figure, the transmission of visible light is high for the four films. However, at a wavelength of 356 nm some absorption takes place, especially for the AZO films and the ITO film deposited at T_s = 25°.

Figures 7-5 and 7-6 show examples of the rise and decay dynamics of the first order diffracted signal from the AZO and the ITO films. The films are the same as presented in Figure 7-4. The diffraction efficiency is in arbitrary units, but the magnitude is known to be within a factor of two (see below). However, the relative magnitude between all curves is correct within the signal-to-noise uncertainty.

In the curves in Figure 7-5 the total pump beam intensity was I_0 = 750 mW/cm^2. This intensity was sufficient to induce gratings in the AZO films. At time zero the two pump beams were turned on and a grating was formed within a few seconds. Some hundred of seconds later the pump beams were switched off, indicated by a broken arrow in the figure, and a slow decay of the grating was observed.

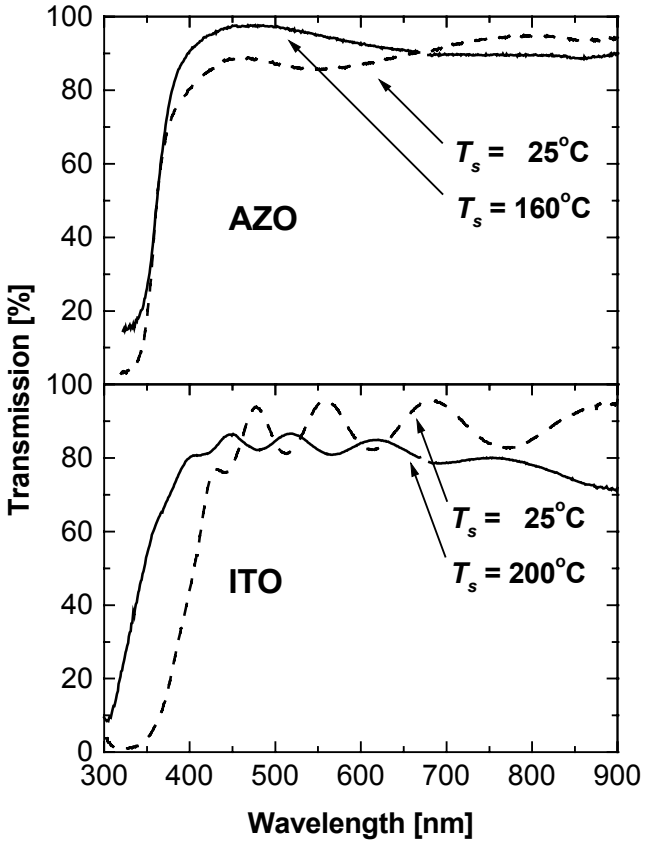

Figure 7-4 Transmission spectra of selected AZO and ITO films deposited at different substrate temperatures, T_s. The film thicknesses are: 210 nm (AZO 25 °C), 180 nm (AZO 160 °C), 670 nm (ITO 25 °C), and 730 nm (ITO 25 °C).

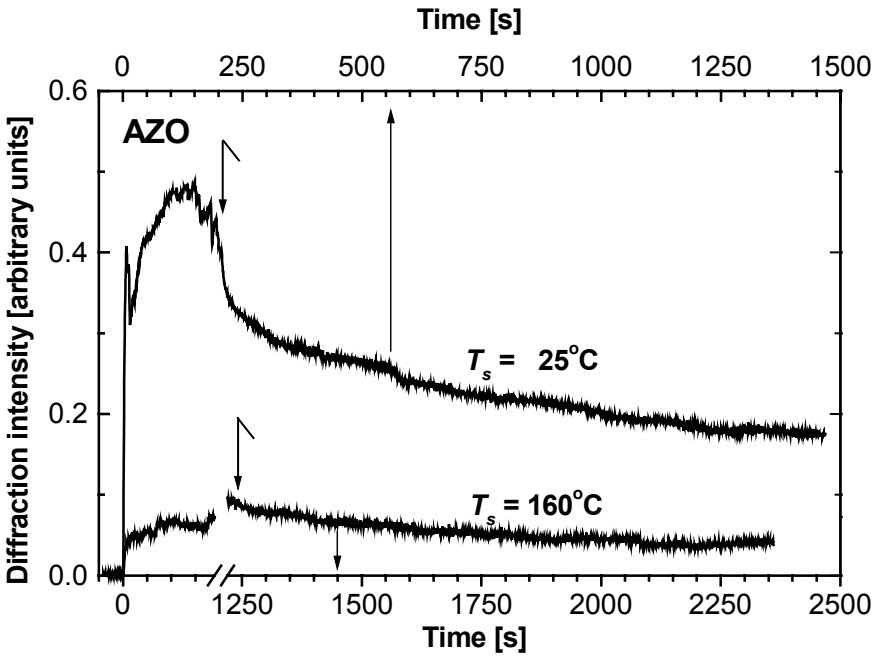

Figure 7-5 Time dynamics of the intensity of the first order diffracted beam in AZO films deposited at different substrate temperatures, T_s. The total pump beam intensity; 750 mW/cm^2. Note the axis break.

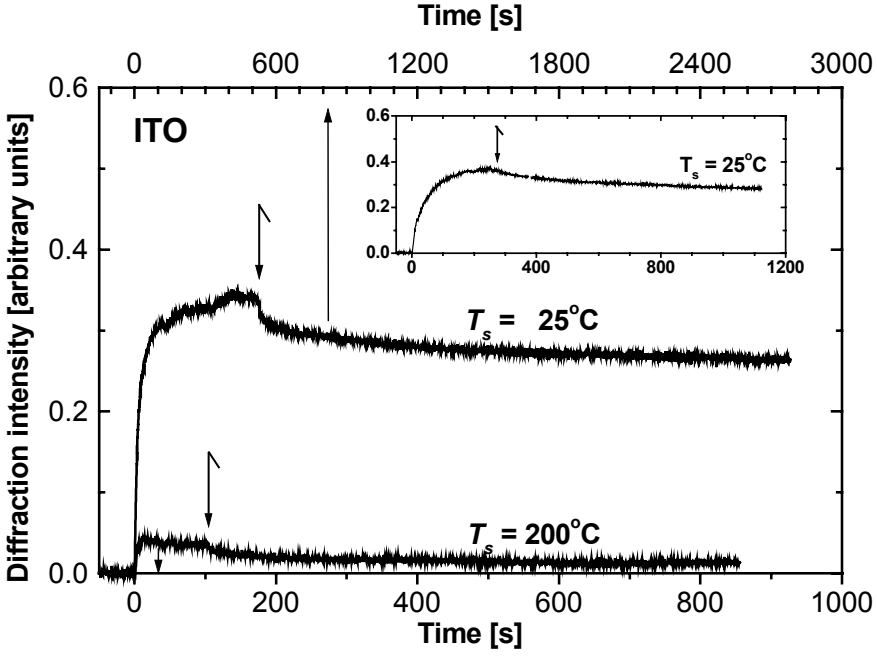

Figure 7-6 Time dynamics of the intensity of the first order diffracted beam in ITO films deposited at different substrate temperatures, T_s. The main curves: total pump beam intensity: 1130 mW/cm^2. The inset: 750 mW/cm^2.

A maximum diffraction efficiency of $\xi = 3.1 \cdot 10^{-6}$ ($\pm 1.6 \cdot 10^{-6}$) was obtained for the AZO film deposited at 25°C (film thickness d = 210 nm). The maximum diffraction efficiency of the AZO film deposited at 160°C (d = 180 nm) was remarkably lower, namely $\xi = 0.77 \cdot 10^{-6}$ ($\pm 0.39 \cdot 10^{-6}$). This rather large difference in diffraction efficiency between films deposited at 25°C and 160°C or 200°C was a general trend, and was also observed for ITO films as demonstrated in Figure 7-6. Grivas *et al.* [2] also obtained a low diffraction efficiency for indium oxide produced at 150°C compared with that obtained at room temperature. Their efficiency was somewhat higher than ours, probably due to the different pump wavelength of 325 nm and the different material.

Diffraction efficiencies together with other optical material parameters for the films presented in the figures are given in Table 7-1.

Table 7-1 Diffraction efficiencies, ξ, and other optical material parameters for selected AZO and ITO films. T_s: substrate temperature. α: absorption coefficient. E_g: energy gap. $|\Delta\eta|$: the modulation amplitude of the complex refractive index.

Material	T_s **[°C]**	ξ **[10^{-6}]**	α ***at 356 nm*** **[10^4 cm^{-1}]**	E_g **[eV]**	$\lvert\Delta\eta\rvert$ **[10^{-4}]**
AZO	25	3.1	5.4	3.47	17
AZO	160	0.77	5.7	3.40	9.8
ITO*	25	2.4	4.3	3.35	4.4
ITO	25	2.2	4.3	3.35	4.6
ITO	200	0.27	0.72	3.77	1.4

* From the inset in Figure 7-6.

The absorption coefficients, α, of the films at 356 nm and the energy gaps were estimated from the transmission spectra presented in Figure 7-4. The estimation procedure has previously been described in subsection 5.3.2. The absolute value of the modulation amplitude of the complex refractive index, $|\Delta\eta|$, was determined from equation (7-6) assuming that the gratings were simple amplitude or phase gratings. The values of $|\Delta\eta|$ are discussed further below.

Typically, increasing the pump beam intensity by 50% did not affect the maximally obtainable diffraction efficiency of the holographic gratings. This is demonstrated in the inset in Figure 7-6. Here an example of two recordings in the same film at different pump beam intensities is presented. Similar recordings have been made in several films of AZO and ITO that were deposited on heated and non-heated substrates. This indicates saturation of the material modulation at the intensities used in this work.

In the experiments the grating period was Λ_G = 0.95 μm, which was large compared with the film thickness. Using a probe wavelength of λ_C = 633 nm, this should give first-order diffracted beams at $\varphi_{I,-1} = \pm 41.7°$ to the film normal (according to equation (7-6)). This agrees well with the measured angle of φ_I = 41° (±1°). With the present geometry it was not possible to observe higher order diffracted beams because they were evanescent. However, both the (-1) and (+1) diffracted beams were observed from all gratings.

In general, the grating formation could be fitted well to a single exponential function of the form $\xi = A\,(1 - \exp(-t/\tau))$, where A is the steady state diffraction efficiency and τ is the characteristic time constant. The only exception was for ITO films deposited at room temperature, where single exponential growth occurred only during the first 20 to 30 seconds. The exponential fits to the AZO

and the ITO curves in Figures 7-5 and 7-6 resulted in the time constants, τ, presented in Table 7-2.

Table 7-2 Time constants for grating formation, τ, and grating decay, τ_1, τ_2, for selected AZO and ITO films.

Material	T_s [°C]	τ [s]	τ_1 [s]	τ_2 [s]
AZO	25	2.8	14	545
AZO	160	3.0	4.1	481
ITO*	25	13	13	361
ITO	25	11	20	634
ITO	200	2.2	2.3	162

* From the inset in Figure 7-6.

As can be seen from the table, the time constants for the grating formation were only a few seconds for the AZO films and the ITO film deposited at T_s = 200°C. For each film, τ in general decreased when the pump beam intensities were increased.

The grating decay appeared to be more complicated. A double exponential function of the form $\xi \propto A_1 \exp(-t/\tau_1) + A_2 \exp(-t/\tau_2)$, with constants A_1, A_2, and with a fast time constant τ_1 and a slow time constant τ_2 was a good approximation to the curves. The time constants associated with the decay in the AZO and the ITO films, presented in Figures 7-5 and 7-6, are given in Table 7-2 as well. The decay time constants were shortest for films deposited at high substrate temperature for each material, as can be seen from the table.

From several different recording experiments it was observed that the diffraction efficiency of the films was not correlated with the electrical conductivity. Furthermore, from the absorption coefficient values presented in Table 7-1 it is obvious that the absorption at the wavelength of 356.4 nm used experimentally does not play a significant role. The absorption of the ITO films at 356 nm differed significantly from 25°C to 200°C in contrast to the AZO films that had almost the same absorption at this wavelength. However, the diffraction efficiency did not deviate noticeably from one material to another, as can be seen from the ξ values in Table 7-1.

7.3.2 Discussion

Apparently, AZO and ITO films deposited by laser ablation demonstrate similar recording properties upon illumination with UV light. In order to estimate the material modulation for the two different materials, it is assumed that the recorded gratings are of the simple amplitude or phase type. Then, the material modulation may be expressed by the absolute value of $\Delta\eta$ (the modulation amplitude of the complex refractive index). From equation (7-6), $\Delta\eta$ is related to the diffraction efficiency, ξ, and film thickness, d, as

$$|\Delta\eta| = \xi^{1/2} \cdot (\lambda_C / \pi d) , \qquad (7\text{-}9)$$

where λ_C is the wavelength of the probe beam. Values of $|\Delta\eta|$ for the different films were given in Table 7-1. Indeed, taking $|\Delta\eta|$ as a measure of the material response to the intensity pattern created by the pump beams, it is clear that AZO has a higher material response than ITO. Especially, the AZO films deposited on non-heated substrates are superior to the other films regarding the holographic recording properties.

Heating the substrate during ITO and AZO film deposition mainly improves the film crystallinity and the film stoichiometry. In other words, the defect density is reduced upon substrate heating. In subsection 5.3.1 it was indicated that upon irradiation with light with an energy below the band-gap energy, the light is mainly absorbed by defects in the films. However, in the case of intense light sources as in the present recording experiments significant two-photon absorption may take place as well. Nevertheless, it is indeed possible that the holographic recording properties are related to the defect density of the films.

Grivas *et al.* [2] proposed that the recording mechanism of their sputter-deposited In_2O_3 and ITO films was influenced by the presence of oxygen vacancies in the films. Oxygen vacancies, which are considered as defects, are responsible for conduction in undoped In_2O_3. Their hypothesis is interesting as the oxygen vacancies only contribute with a minor fraction to the electrical conductivity in AZO and ITO films. This could explain why the diffraction efficiency apparently is not connected to the film conductivity for these films. However, some film transparency and, thus, a significant amount of oxygen in the films are necessary for holographic recording as it was not possible to produce gratings in dark AZO and ITO films.

Another interesting point is the difference in $|\Delta\eta|$ for films deposited on non-heated and heated glass substrates. The difference in $|\Delta\eta|$ is almost a factor of two for the AZO films, but a factor of three for the ITO films. This difference between AZO and ITO confirms the assumption that the optical material response of these films is connected to the amorphous parts. As demonstrated in the previous chapter, ITO films deposited at T_s = 25°C are amorphous, while ITO films deposited at T_s = 200°C are polycrystalline. In contrast, AZO films deposited both at T_s = 25°C and T_s = 160°C contain some crystalline material, even though, the amount of crystalline material is highest for films deposited at T_s = 160°C. In other words, the difference in crystalline material between films deposited on heated and non-heated substrates is highest for ITO in agreement with the high difference in $|\Delta\eta|$.

7.4 Summary

Holographic grating formation induced by UV laser light at 356.4 nm has been demonstrated in laser deposited AZO and ITO films. The existence of holographic recording upon UV illumination in materials other than indium oxide and indium tin oxide indicates that the recording properties are not associated with specific properties of the indium components. Holographic recording can be extended to other transparent conducting materials as, e.g., AZO.

The holographic recording properties of AZO are superior to those of ITO for films deposited by laser ablation at 355 nm. The grating formation may be connected to defects in the films.

7.5 References

1 S. Mailis, L. Boutsikaris, N.A. Vainos: Appl. Phys. Lett. **69**, 2459 (1996)

2 C. Grivas, D.S. Gill, S. Mailis, L. Boutsikaris, N.A. Vainos: Appl. Phys. A **66**, 201 (1998)

3 B. Thestrup, C. Dam-Hansen, J. Schou, P.M. Johansen, *Holographic grating formation in laser deposited aluminium-doped zinc oxide and indium tin oxide films*, submitted to Journal of Optics A, December 1999

4 H.J. Eichler, P. Günter, D.W. Pohl: *Laser-Induced Dynamic Gratings* (Springer-Verlag, Berlin 1986)

8 Conclusions

The main contributions from the work presented in this thesis are:

- The design and initial testing of a pulsed laser deposition setup with the opportunity of varying the key deposition parameters.
- The presentation of a comprehensive experimental study on how the material properties of laser deposited ITO films at 355 nm are affected by specific experimental parameters in the PLD process. The study has especially clarified the connection between the electrical and the optical properties of the ITO films and the background atmosphere.
- A comparison between the material properties of AZO and ITO films grown under similar deposition conditions.
- The demonstration of holographic recording formation in laser deposited AZO and ITO thin films. In particular, the verification of holographic recording possibilities upon UV illumination in transparent, semiconducting materials other than indium oxide compounds.

8.1 Main conclusions

Four topics have been presented in this thesis. The main conclusions from these topics are given below.

8.1.1 ITO deposition rates

The experiments presented in chapter 4 clearly demonstrated that ITO deposition rates strongly depend on experimental deposition parameters such as the type of background atmosphere, the gas pressure, and the laser fluence. The ITO deposition rates in oxygen and three inert gases - neon, argon and xenon - were compared. The highest deposition rates, at similar laser fluence, were obtained in oxygen. This result may be ascribed to gas dynamic effects as well as to chemical effects between the ablated species and the oxygen background gas.

8.1.2 ITO films deposited in various background atmospheres

In chapter 5 it was shown how the ITO film properties, the surface structure and the composition were related to key deposition parameters in the PLD process. ITO films, produced in oxygen, neon, argon and xenon on non-heated and heated glass substrates, were analysed and compared.

In general, the electrical resistivity of ITO films deposited on non-heated substrates varied strongly with gas pressure, especially for films deposited in oxygen, argon, and xenon. This pressure dependence of the film resistivity may be connected to the particle dynamics in the plasma plume *prior* to deposition, which is expected to change with pressure. The film composition seemed important for the electrical properties of the ITO films. The optical properties of the ITO films turned out to be, among other things, sensitive to the film structure. An oxygen background atmosphere during deposition at room temperature improved the film structure.

The resistivity of ITO films deposited at 200°C was almost independent of the ambient gas pressure. Depositing ITO films on heated substrates mainly improved the crystallinity of the films and thereby the resistivity. At deposition in oxygen the ITO film stoichiometry seemed to be improved as well. The lowest resistivities were obtained for ITO films deposited in oxygen at 200°C. This improvement in resistivity can be ascribed to chemical effects, during film deposition, involving the oxygen gas.

Despite the wavelength of 355 nm used, which corresponds to an energy below the band-gap of indium oxide, it was possible to obtain high-quality ITO films at low substrate temperatures.

8.1.3 AZO and ITO films deposited at high laser fluence

Chapter 6 presented results that compared the electrical and the optical properties as well as the surface structure and the crystallinity of AZO and ITO films deposited in an oxygen atmosphere.

The electrical properties of the ITO films were superior to the AZO films under similar deposition conditions. However, the average transmission of visible light was in general high for both materials. The surface of the ITO films was smooth with height variations in the order of a nanometer. However, particulates were identified on the surfaces. In contrast, the AZO films were rough with height variations between 10 and 100 nm depending on the substrate temperature during deposition. ITO films deposited on non-heated substrates were amorphous, whereas the AZO films contained some crystalline material. Films deposited at 200°C were polycrystalline.

The material properties of the ITO films deposited at high fluence (around 2.0 J/cm^2) were superior to the ITO films deposited at low fluence (around 0.5 J/cm^2).

8.1.4 Holographic recording in AZO and ITO films

Holographic grating formation induced by UV laser light was demonstrated in laser deposited AZO and ITO films. The holographic recording properties of AZO were superior to those of ITO. The existence of holographic recording upon UV illumination in materials other than indium oxide and indium tin oxide indicates that the recording properties are not associated with specific properties of indium compounds.

8.2 Future perspectives

There is a large potential for the application of transparent, semiconducting films deposited at relatively low substrate temperatures. The pulsed laser deposition technique has proved to be competitive to other vacuum deposition techniques within the field of deposition of multicomponent oxides.

For commercial applications the particulate density of the laser deposited ITO films needs to be reduced, and the surface structure of the AZO films must be improved. Therefore, future work on laser deposited ITO and AZO films is suggested at a laser wavelength of, e.g., 248 or 266 nm. Operating at these wavelengths implies the possibility of reducing particulates as well as improving the AZO surface structure.

In addition, further investigations of the specific role of the ambient background atmosphere are suggested. A combination of *in situ* diagnostic methods as, e.g., time-of-flight measurements and post-deposition diagnostic methods is recommended.

An interesting idea would be to deposit transparent, semiconducting oxides in an atmosphere mixture of oxygen and helium. A low-mass gas such as helium is expected to reduce fast oxygen ions that may create defects in the growing film. Furthermore, helium may broaden the time-of-flight distribution (measured at the substrate position) of the ablated oxygen particles, which is desirable.

New interesting substrates for laser deposition of ITO or AZO may be, e.g., organic materials or heat-sensitive polymers.

Appendices

A. Spot size and quartz crystal microbalance measurements

Spot size measurement

In order to determine the laser beam spot size on an ITO target (see section 3.1), several beam spots at various laser pulse energies were made on a target. The area of each beam spot was then determined by measuring the minor and major semiaxis of the elliptical spot using a caliper. Figure A 1 shows the single beam shot area versus laser pulse energy. Above a laser pulse energy of approximately 125 mJ the single shot area became almost constant. The spot size is defined from the intersection of two line fit and found to be 0.0718 cm^2 (at a pulse energy of 125 mJ corresponding to a laser fluence of 1.8 J/cm^2).

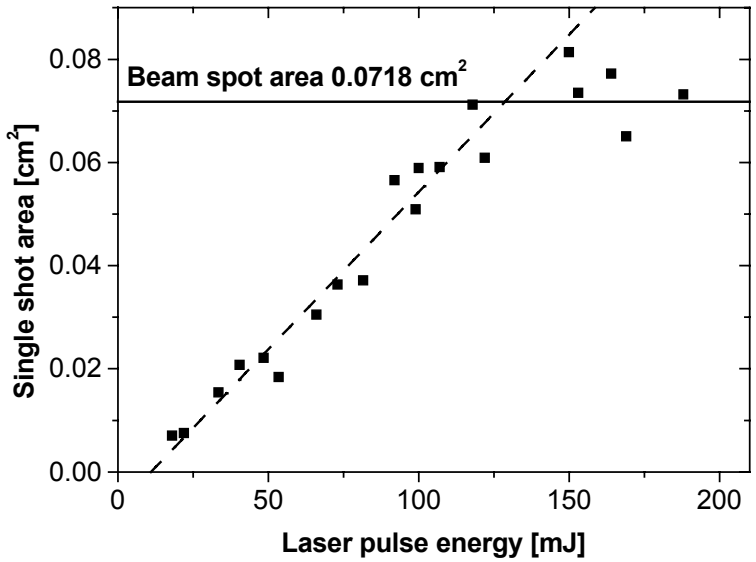

Figure A 1 Beam spot area versus laser pulse energy. The spot size is found from the intersection of the line fits.

Quartz crystal microbalance measurements

The mean mass deposition rate, D_M, was determined from QCM measurements as described in subsection 3.2.1. Figure A 2 shows an example of how the resonance frequency, f_q, of a quartz crystal decreases with time during ablation of an ITO target. The resonance frequency was measured every third second applying a Quick Basic program. A typical frequency measurement was made within a few minutes only in order not to overload the crystal. The frequency decrease as a function of time, $\Delta f/\Delta t$, was then determined from the slope of a line fit to the

data using a commercial data handling program. As the deposition rate decreased significantly during the first minute of ablation, data was only collected after one minute of ablation. In cases of very high deposition rate, the deposition rate was measured within one minute only and D_M instead calibrated by subtracting 10% from the measured deposition rate value.

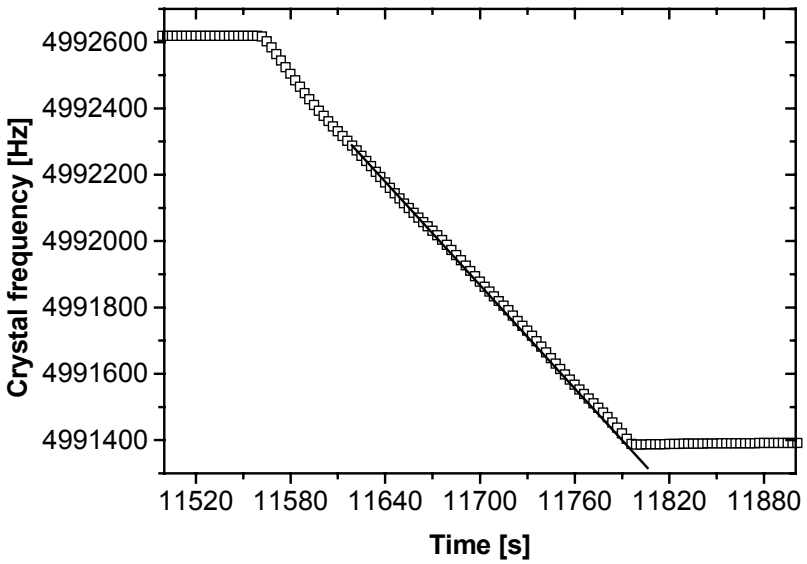

Figure A 2 Crystal frequency versus time during ablation of ITO. Fluence: 0.5 J/cm^2. Oxygen pressure: 23 mtorr.

List of experimental equipment

- ***Laser:*** NY81C-10 from Continuum.
  Wavelengths: 1064 nm, 532 nm, 355 nm, 266 nm.
  Pulse width (FWHM): 5.7 ns at 355 and 266 nm.
  Specifications (at installation): Energy 320 mJ, energy stability ±4.0 %, power drift ±5.0 % (all values for a repetition rate of 10 Hz).
  Beam intensity profile: Quasi-gaussian.
  The laser beam was *s*-polarised at target incidence.
- ***Targets:*** Hot pressed ceramics from Pure Tech. Inc..
- ***Substrates:*** Microscope cover glasses from Knittel Gläser.
- ***Step motors:*** From MIR Electronic Vertriebs.
- ***Laser power meter:*** From Ophir.
- ***Microscope slides:*** From Knittel Gläser.
- ***Cold cathode gauge:*** From Baltzers.
- ***Pirani gauge:*** From Alcatel.
- ***Diffusion pump:*** From Alcatel.
- ***Quartz crystal microbalance:*** AT-cut crystal from Baltzer.
- ***Spectrophotometer:*** Cary UV/Visible from Varian.
- ***Atomic Force Microscope:*** Dimension 3000 from Digital Instruments.
- ***Diffractometer:*** Rotating anode diffractometer at Risø.

B. Estimated collection cross section for collision of silver ions with a neon background gas

In this appendix, the collection cross section for collision of silver ions with a neon background gas is estimated. The experiments were performed with the experimental setup described in section 3.3.

Figure B 1 shows the dependence of the silver ion current, *I*, in the transmitted peak (first ion peak) of the TOF spectrum on $N \times R_{TP}$. Here, N is the particle density of the neon background atmosphere and R_{TP} the target-probe distance.

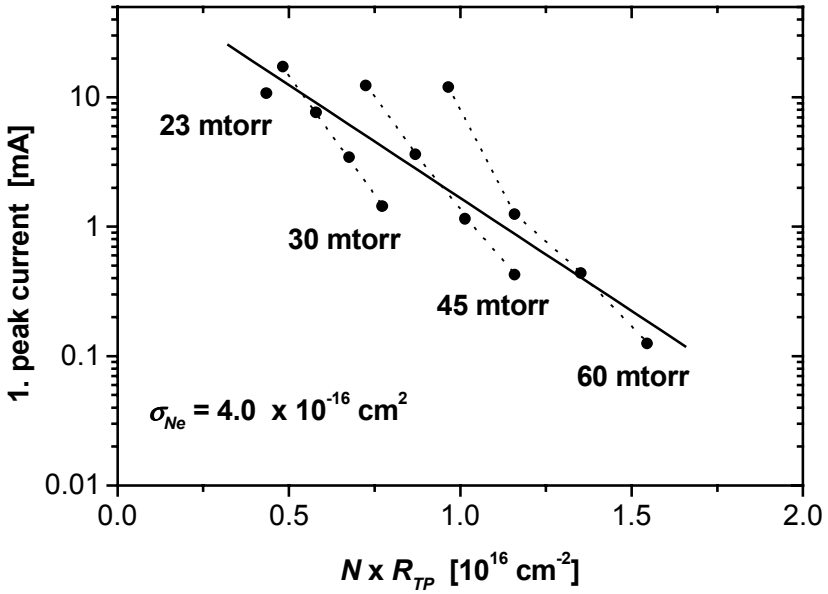

Figure B 1 Ion current of the 1. silver ion peak versus $N \times R_{TP}$. The neon pressure, for each R_{TP} data series, is given as well. N: Neon particle density. R_{TP}: Target-probe distance. σ_{Ne}: Estimated collection cross section for collision of silver ions with a neon gas. Fluence: 2.4 J/cm^2.

The collection cross section, σ_{Ne}, for collision of silver ions with a neon gas is estimated from the Figure using a simple Beer's law scattering model for the ions in the 1. peak (following the same procedure as in [1]). In this model, it is assumed that the 1. peak current, *I*, measured by the probe may be given as

$$I \propto exp(-\sigma_{Ne} N R_{TP}) \qquad (B\ 1)$$

Thus, from the slope of a line fit (least squares methods) to the data in Figure B 1 it is possible to estimate σ_{Ne}, i.e. the collection cross section for collisions of silver ions with the neon background gas. From the Figure, $\sigma_{Ne} = 4.0 \cdot 10^{-16}$ cm^2.

For each R_{TP} data series measured at a constant neon pressure, the data points are scattered around the line fit. This data scattering is due to two facts

1. The ion probe was placed at an angle of 7.5° to the target normal and, therefore, slightly outside the plasma plume centre.

This means, that when the probe is moved toward the target, the probe gets closer to the plume centre-line, where the ion-density is highest [2]. Therefore, at constant neon pressure, due to the geometry alone, higher peak-currents are expected at a target-probe distance of 50 mm relative to a target-probe distance of 80 mm.

2. The relative collecting area decreases with increasing target-probe distance.

The probe area divided by the surface area of a semi-sphere with centre at the target and radius equal to R_{TP} increases with decreasing R_{TP}.

In this thesis, it has been assumed that it is reasonable to compare the dynamics (in a background gas) of ablated silver ions with the dynamics of ablated indium and tin ions. Table B 1 presents some calculated total collision cross sections, σ_T, for silver ions scattered into different atmospheres and for indium, tin, and oxygen ions scattered into neon. The collision cross sections are based on a simple hard sphere scattering model. In this model, the ion-particle collision is treated as a collision between two hard, elastic spheres of diameter d_1 and d_2, respectively. The total collision cross sections is then given as

$$\sigma_T = \pi \ (d_{12})^2, \quad d_{12} = \tfrac{1}{2} (d_1 + d_2) \qquad (B\ 2)$$

In the calculations, the collision diameters and the covalent radii (times two), given in Table 4-2 in chapter 4, have been used as the particle diameters.

Table B 1 Calculated total collision cross sections, σ_T, for ions scattered in a gas.

Ion	***Gas***	σ_T **[10^{-16} cm^2]**
Ag^+	Oxygen	(30.5)
Ag^+	**Neon**	**21.4**
Ag^+	Argon	30.8
Ag^+	Xenon	43.7
In^+	**Neon**	**23.1**
Sn^+	**Neon**	**22.6**
O^-	Neon	12.6

The total collision cross section for indium and tin ions scattered into neon is within 10% of the total collision cross section for silver ions ablated into neon. Therefore, it seems reasonable to compare the dynamics of silver ions with the dynamics of indium and tin ions.

The total collision cross section for silver ions scattered into oxygen is given in brackets, as an oxygen molecule cannot be considered as a hard sphere. The amount of possible scattering processes are much higher for *ion – molecule* collisions than for *ion – atom* collisions, since a molecule can be vibrationally and rotationally excited in excess of being electronically excited.

The estimated collection cross sections and the total collision cross sections cannot be compared directly, as they do not represent the same events. However, it may be interesting to compare ratios of these quantities. From the measurements (this work and [1]) σ_{Ne}/σ_{Ar} = 0.60 and from the calculations $\sigma_{T\{Ag^+ \rightarrow Ne\}}/\sigma_{T\{Ag^+ \rightarrow Ar\}}$ = 0.70. I.e. the cross section ratios (for silver ion scattered in neon versus silver ions scattered in argon) are in reasonable agreement with each other (within 14%).

1 T.N. Hansen, J. Schou, J.G. Lunney: Appl. Surf. Sci. **138-139**, 184 (1999)

2 T.N. Hansen, J. Schou, J.G. Lunney: Europhys. Lett. **40**, 441 (1997)

C. Estimated average absorption coefficients for AZO and ITO films

Figure C 1 shows the quantity $-\ln(T_{Av})/d$ versus oxygen pressure during deposition for representative AZO and ITO films deposited at room temperature. Here, T_{Av} is the average film transmission between 450 and 750 nm, measured with a spectrophotometer. d is the film thickness.

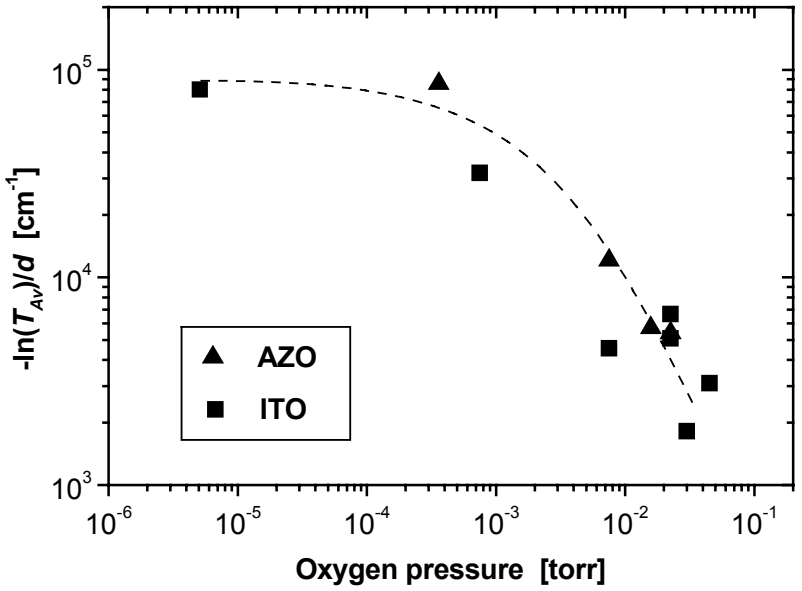

Figure C 1 The quantity $-\ln(T_{Av})/d$ as a function of oxygen pressure for representative AZO and ITO films deposited at 25°C. T_{Av}: Average transmission between 450 and 750 nm. d: Film thickness. The line is for guidance only.

For low values of T_{Av} the quantity $-\ln(T_{Av})/d$ is roughly proportional to the average absorption coefficient, α_{Av}, over the measured wavelength range. The decrease in $-\ln(T_{Av})/d$ with increasing oxygen pressure corresponds to a decrease in α_{Av}. At the highest oxygen pressures, the film absorption is so low that the transmission is approximately reflectivity limited, making it difficult to obtain accurate values of α_{Av} [1].

1 J.C.C. Fan, F.J. Bachner, G.H. Foley: Appl. Phys. Lett. **31**, 773 (1977)

List of figures

List of tables

Nomenclature

Symbol (a,A,α)	*Unit*	*Meaning of quantity*
a	m	Distance between adsorption sites
a_e	m	Effective collision diameter
d	m	Film thickness
d_1,d_2	m	Quartz crystal and electrode thickness
d_1,d_2	m	Particle diameters
e	C	Elementary charge
f_q	Hz	Resonance frequency
Δf	Hz	Frequency shift
h	m	Target-substrate distance
k		Imaginary part of complex refractive index
k_B	J/K	Boltzmann's constant
k, k_F	m^{-1}	Wave number, Fermi wave number
$\boldsymbol{k}$	m^{-1}	Wave vector
l,b,d	m	Length, width and thickness
l_1,l_2	m	Quartz crystal and electrode diameter
l_c,l_s	m	Contact tip diameter and spacing
m	J	Supersaturation
m	amu	Ion mass
m_c^*, m_v^*, m_{vc}^*	amu	Effective masses
n	m^{-3}	Molar concentration
n,n_0,n_1		Refractive indices
n_e	m^{-3}	Carrier concentration
p	Pa, torr	Pressure
$\boldsymbol{q}$, q	m^{-1}	Grating vector, length of grating vector
r_0	m	Radius of laser beam spot on target
t	s	Time
t_P, t_A	s	Peak time, arrival time
Δt	s	Time interval
v_0, v_t	m/s	1st peak velocity, transverse velocity
x	m	A length axis
A		Steady state diffraction efficiency
C_f	amu/(Hz m^2)	QCM calibration constant
C_{Sn}	at%	Tin concentration
D	m/s	Linear deposition rate
D_I	m/s	Instantaneous deposition rate
D_M	amu/m^2s	Mass deposition rate
E, E_F	eV	Energy, Fermi energy
E_g, E_g^0, W	eV	Energy-gaps, energy difference
ΔE_g^{BM}	eV	Burstein-Moss shift
F	J/m^2	Fluence
ΔG	J	Total cluster free energy
ΔG^*	J	Free energy barrier for nucleation
I	A	Electric current
I_A, I_B, I_0, I_C, I_D	W/m^2	Intensities
Kn		Knudsen number
M		Oscillation number

Symbol (a,A,α)	*Unit*	*Meaning of quantity*
M	amu	Atomic mass
M		Intensity modulation coefficient
N	m^{-3}	Particle density
N		Number of ions
N_A	amu/g	Avogadro's number
R	Ω	Electrical resistance
R_s	Ω/square	Electrical sheet resistance
R_a,R_e	$cm^{-2}s^{-1}$	Actual and equilibrium deposition rate
R_{TP}	m	Target-probe distance
S	m^2	Probe area
T	K	Absolute temperature
T_{Av}	%	Average transmission
T_s	K	Substrate temperature
T_m	K	Melting temperature
T_{ap},T_{cycle}	s	Time constants
ΔT	s	Film deposition time
V	V	Voltage
α	m^{-1}	Absorption coefficient
α_{Av}	m^{-1}	Average absorption coefficient
ε_0, ε_∞	F/m	Dielectric constants
γ	s^{-1}	Quantity related to mobility
η		Complex refractive index
$\Delta\eta$		Modulation amplitude
φ_m	degrees	Diffracted beam angle
λ	m	Wavelength
λ_{gap}, λ_{pl}	m	Band-gap and plasma wavelength
λ_p, λ_C	m	Pump and probe wavelength
μ,μ_H	cm^2/Vs	Mobility, Hall mobility
ν	Hz	Frequency
θ	degrees	Angle
ρ	Ωm	Electric resistivity
ρ_{min}	Ωm	Resistivity minimum
ρ_f	kg/m^{-3}	Film density
σ	$(\Omega m)^{-1}$	Electric conductivity
σ_{O2}, σ_{Ne}, σ_{Ar}	m^2	Collection cross sections
σ_T	m^2	Total collision cross section
τ	s	Characteristic time constant
ξ		Diffraction efficiency (first order)
h, $\hbar$	Js	Planck´s constant
$\hbar\Sigma_c$, $\hbar\Sigma_v$	eV	Self-energies
Λ	m	Mean free path
Λ_D	m	Diffusion length
Λ_{Ion}	m	Ion mean free path
Λ_G	m	Grating period

Abbreviations

AFM	Atomic force microscope
AZO	Aluminium doped zinc oxide
CVD	Chemical vapour deposition
HTS	High-temperature superconductor
ITO	Indium tin oxide
PLD	Pulsed laser deposition
QCM	Quartz crystal microbalance
TE	Transverse electric
TEM	Transverse electric magnetic
TOF	Time-of-flight
UHV	Ultra high vacuum
UV	Ultraviolet
XPS	X-ray photoelectron spectroscopy
XRD	X-ray diffraction
YBCO	Yttrium Barium Copper Oxide

Photogallery

Photo 1: Side view of laser plasma seen through vacuum window during film deposition. The plasma is the elongated bright area in the blue light seen in the lower right corner of the photo. The author to this thesis is standing left to the chamber.

Photo 2: Film deposition chamber (opened). The deposition system, mounted on the upper chamber flance, is raised above the chamber. A. Nordskov is standing left to the chamber.

Photo 3: Close up of the deposition system with an irradiated ITO target.

Photo 4: Microscope picture of an ITO target. Upper part; un-irradiated area, mat appearance. Lower part; irradiated area, shiny metallic look. Magnification around 1:40.

Photo 5: Microscope picture of an ITO film on a glass substrate. The black line is the substrate border. Left side; ITO film. Right side; glass substrate. Magnification around 1:40.

Photo 6: Surface image of AZO film deposited at 25℃ in 23 mtorr of oxygen at a fluence of 2.0 J/cm^2. Film thickness ~232 nm. x-axis: 500 nm/div. z-axis: 100 nm/div.(AZO01_06).

Photo 7: Surface image of AZO film deposited at 160℃ in 23 mtorr of oxygen at a fluence of 2.0 J/cm^2. Film thickness ~186 nm. x-axis: 500 nm/div. z-axis: 100 nm/div.(AZO01_11).

Photo 8: Surface image of ITO film deposited at 25℃ in 23 mtorr of oxygen at a fluence of 1.9 J/cm^2. Film thickness ~214 nm. . x,y-axis: 1μm/div.(ITO12_14).

Photo 9: Surface image of ITO film deposited at 200℃ in 23 mtorr of oxygen at a fluence of 1.9 J/cm^2. Film thickness ~186 nm. x,y-axis: 1μm/div.(ITO12_19).

Photo 10: Microscope surface images of AZO film deposited 25℃ in $7.4 \cdot 10^{-4}$ torr of oxygen at a fluence of 2.0 J/cm^2. Film thickness ~372 nm.(AZO01_02).

Photo 1

Photo 2

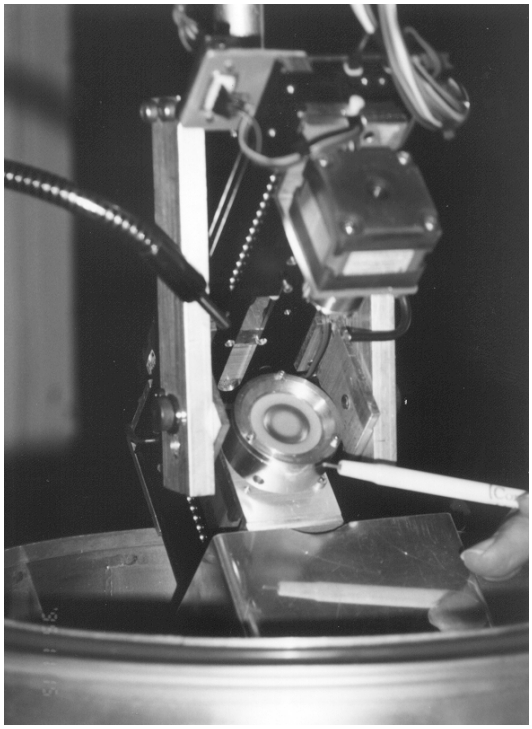

Photo 3

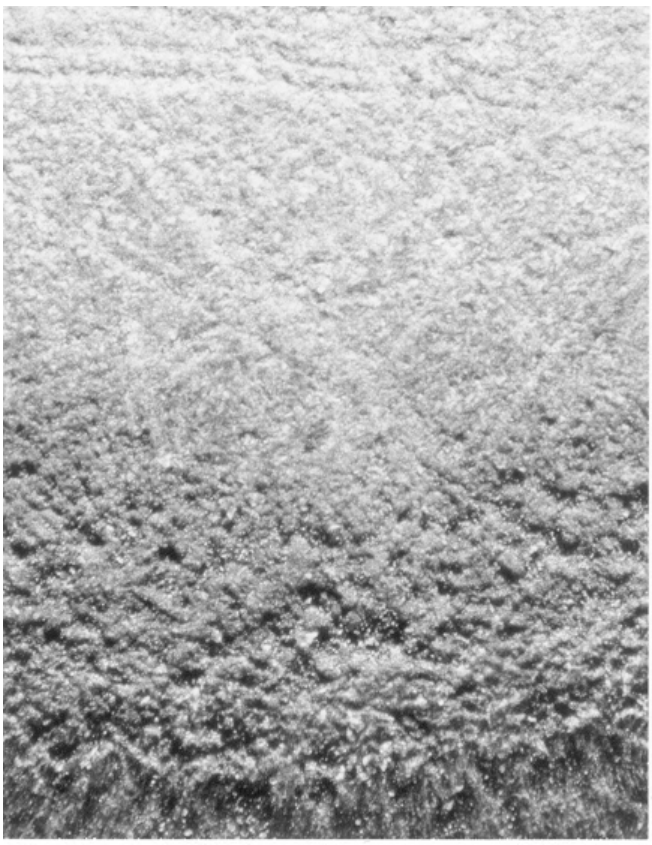

Photo 4

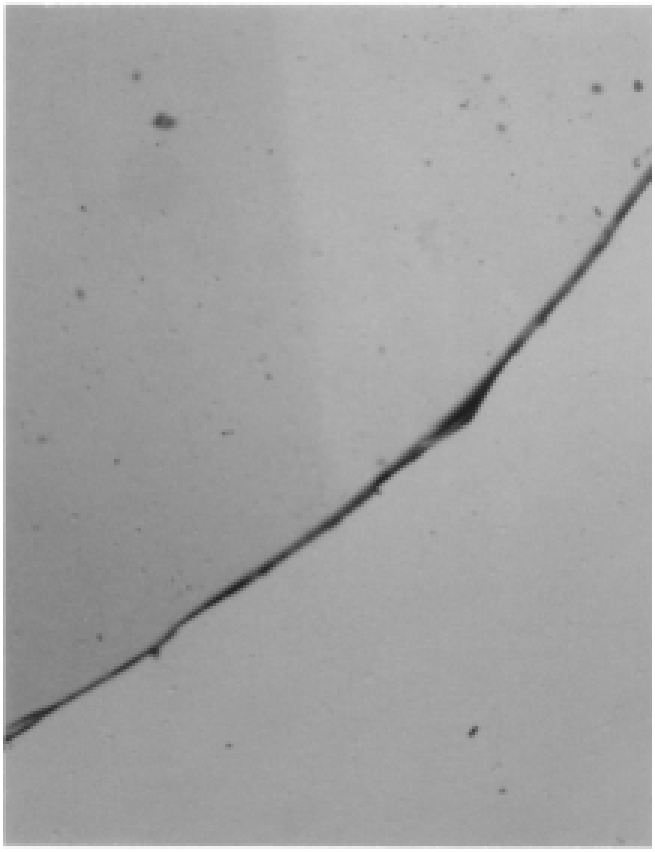

Photo 5

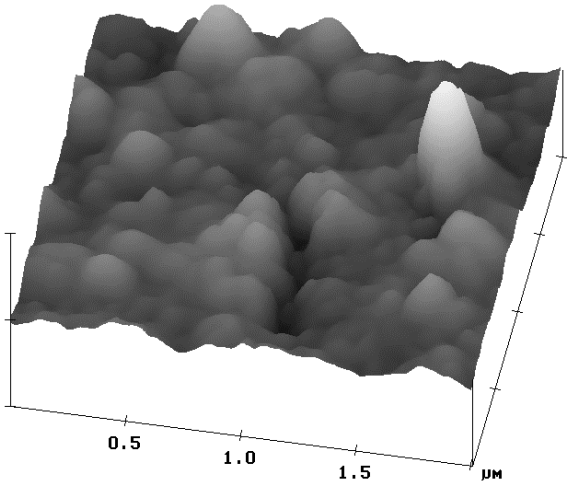

Photo 6

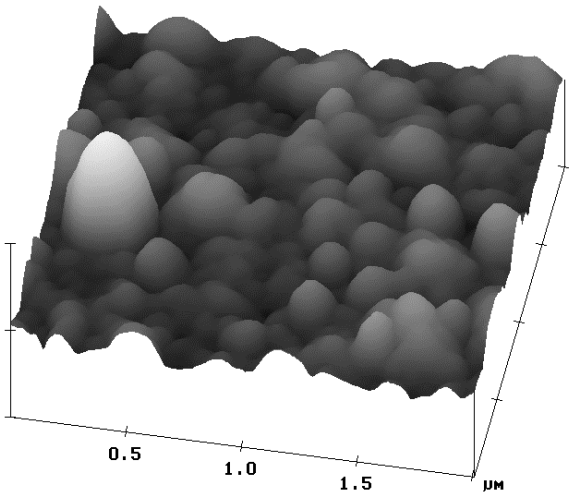

Photo 7

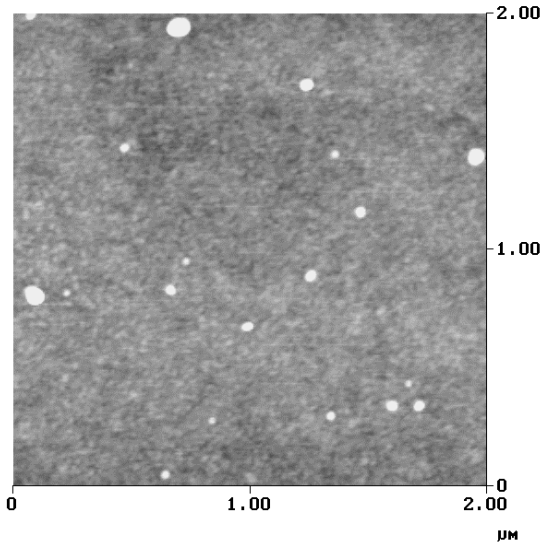

Photo 8

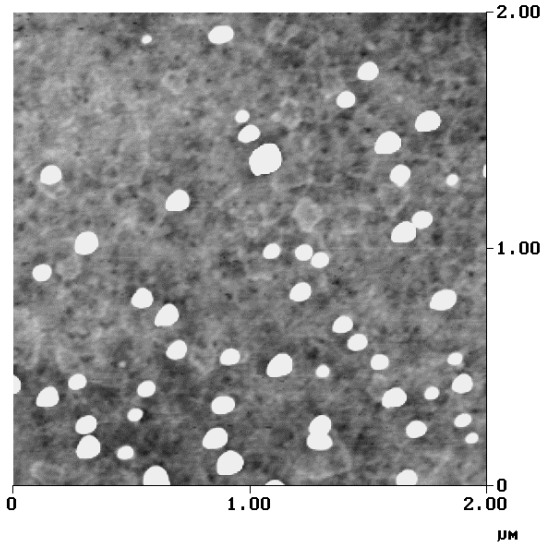

Photo 9

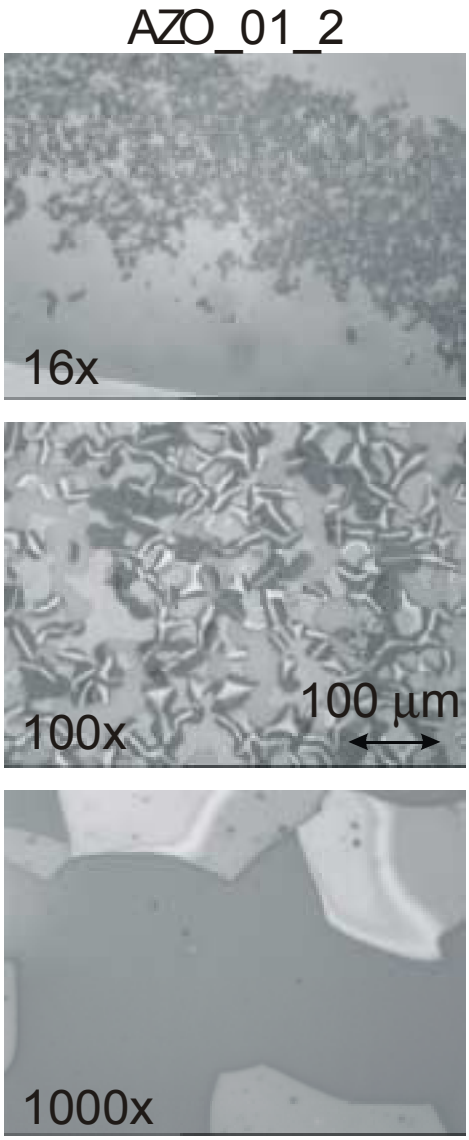

Photo 10

9 Personal bibliography

Refereed articles

1. B. Thestrup, W. Svendsen, J. Schou, O. Ellegaard (1994*), Sputtering of thick D_2 films by keV electrons*, Phys. Rev. Lett. **73**, pp. 1444-1447

2. W. Svendsen, B. Thestrup, J. Schou, O. Ellegaard (1995), *Sputtering of thin and intermediately thick films of solid deuterium by keV electrons*, Nucl. Inst. and Meth. B **101**, pp. 174-178

3. W. Svendsen, J. Schou, B. Thestrup, O. Ellegaard (1996), *Ablation from metals induced by visible and UV laser irradiation*, Appl. Surf. Sci. **96-98**, pp. 518-521

4. W. Svendsen, A. Nordskov, J. Schou, B. Thestrup, O. Ellegaard (1997), *Angular distributions and total yields of laser ablated silver*, Nucl. Inst. and Meth. B **122**, pp. 356-358

5. J. Schou, B. Thestrup, W. Svendsen, B. Stenum, O. Ellegaard, R. Pedrys, B. Warczak (1998), *Sputtering of surfaces of the solid hydrogens*, J. of Low Temp. Phys. **111**, pp. 569-576

6. B. Thestrup, J. Schou, A. Nordskov, N. B. Larsen (1999), *Electrical and optical properties of thin indium tin oxide films produced by pulsed laser ablation in oxygen or rare gas atmospheres*, Appl. Surf. Sci. **142**, pp. 248-252

7. B. Thestrup, J. Schou (1999), *Transparent, conducting AZO and ITO films produced by pulsed laser ablation at 355 nm*, Applied Physics A **69**, s807-s810

8. B. Thestrup, C. Dam-Hansen, J. Schou, P.M. Johansen (2000), *Holographic grating formation in laser deposited aluminium-doped zinc oxide and indium tin oxide films*, J. Opt. A **2**, pp 196-199

10 Reprints of publications

The publications prepared as a result of the work carried out during the present Ph.D. study are listed below. Reprints of the publications are given in the following pages.

- B. Thestrup, J. Schou, A. Nordskov, N.B. Larsen, *Electrical and optical properties of thin indium tin oxide films produced by pulsed laser ablation in oxygen or rare gas atmospheres*, Appl. Surf. Sci. **142**, 248 (1999)

- B. Thestrup, J. Schou, *Transparent, conducting AZO and ITO films produced by pulsed laser ablation at 355 nm*, Applied Physics A **69**, s807 (1999)

- B. Thestrup, C. Dam-Hansen, J. Schou, P.M. Johansen, *Holographic grating formation in laser deposited aluminium-doped zinc oxide and indium tin oxide films*, J. Opt. A **2**, 196 (2000)

Title and author

Deposition of ITO and AZO thin films by laser ablation at 355 nm in a background atmosphere

Birgitte Thestrup

ISBN	ISSN
87-550-2609-5	0106-2840

Department	Date
Optics and Fluid Dynamics Department	February 2000

Pages	Tables	Illustrations	References
147	11	44	163

Abstract (max. 2000 characters)

The main topic in this thesis is deposition of ITO and AZO thin films by pulsed laser ablation at 355 nm in a background atmosphere.

Indium tin oxide (ITO) and aluminium doped zinc oxide (AZO) films belong to the transparent, semiconducting films, which have many applications in opto-electronic devices.

Pulsed laser deposition (PLD) is a relatively new film deposition technique, which is applicable, especially, for deposition of multi-component oxide materials. However, despite of its success, the deposition process is not understood in detail.

Here, a design of a pulsed laser deposition setup with the opportunity of varying key deposition parameters is presented. A comprehensive experimental study, on how the material properties of laser deposited ITO films at 355 nm are influenced by specific experimental parameters in the PLD process, is given. Especially, this study clarifies the connection between the electrical and optical properties of the ITO films and the background atmosphere. Furthermore, a comparison between the material properties of AZO and ITO films grown at similar deposition conditions is presented. Finally, holographic recording in laser deposited AZO and ITO thin films is demonstrated.

Descriptors INIS/EDB

Available on request from Information Service Department, Risø National Laboratory,
(Afdelingen for Informationsservice, Forskningscenter Risø), P.O.Box 49, DK-4000 Roskilde, Denmark.
Telephone +45 4677 4004, Telefax +45 4677 4013